UNIVERSIDADE ESTADUAL PAULISTA
FACULDADE DE ENGENHARIA,
CAMPUS DE ILHA SOLTEIRA - FEIS

Texto Sistemático Crítico para Concurso de Livre Docência

Supercondutividade em tamanhos mesoscópicos

Rafael Zadorosny

Ilha Solteira
2018

UNIVERSIDADE ESTADUAL PAULISTA
FACULDADE DE ENGENHARIA,
CAMPUS DE ILHA SOLTEIRA - FEIS

Supercondutividade em tamanhos reduzidos

Rafael Zadorosny

Texto Sistemático Crítico Apresentado à Faculdade de Engenharia de Ilha Solteira da Universidade Estadual Paulista – UNESP, para o Concurso de Livre Docência junto ao Departamento de Física e Química na disciplina de Eletromagnetismo.

Ilha Solteira
2018

Dedicatória

Dedico esse trabalho a todos que participaram da minha vida e sempre acreditaram no meu trabalho, família, amigos, meu ex-orientador e meus orientandos

Agradecimentos

Agradeço a todos os colaboradores que me ajudaram a efetivar tanto os trabalhos que aqui serão apresentados, quanto aqueles que foram e estão sendo desenvolvidos. Da minha família, agradeço aos meus pais, Sueli D. J. Zadorosny e Aristeu Zadorosny, ao meu irmão, Lincon Zadorosny, à minha mulher, Francine Bettio Costa e ao meu filho, André Luiz Zadorosny. Especial gratidão ao meu ex-orientador e, ainda mentor, Wilson Aires Ortiz; ao Edson Sardella, com o qual tenho trabalhado desde o pós-doutorado e pela amizade que desenvolvemos nesse tempo; ao Maycon Motta, um irmão que ganhei e com o qual tenho o prazer de estar, novamente, desenvolvendo um trabalho conjunto.

Agradeço, ainda, a todos que trabalharam e /ou trabalham comigo, Cláudio Luiz Carvalho, que me recebeu em seu grupo quando fui contratado na UNESP e pela amizade, e aos meus ex-orientandos e atuais orientandos, Vivian D. Rodrigues, Joao B. da Silveira, Regiane G. de Lima, Gisele A. de Souza, Elwis C. S. Duarte, Maycon Rotta, Alexsander L. Pessoa, Alice Presotto, Danilo Okimoto, Vinicius S. Souto, Alex N. B. da Silva, Adriana G. Presotto, Ana M. Caffer.

Aos técnicos e servidores que mais me acompanharam nesses mais de sete anos de UNESP: Solange Marlene Nascimento (que nos deixou saudades), Thiago R. Nicolette, Mario P. C. Júnior, Gilberto A.de Brito, Elton J. de Souza, Márcia R. N. Chaves, Graciele P. V. Nizo, Thaís L. da Rocha e Ailton dos Reis.

Finalizando e não menos importante, gostaria de agradecer às agências de fomento CAPES e CNPq e, principalmente, á FAPESP com a qual tenho uma relação que passou por bolsa de IC, doutorado direto, pós-doutorado e, ultimamente, dois projetos de pesquisa além dos vários fomentos para participação em eventos no exterior.

Sumário

1. Resumo

A supercondutividade em escalas nanoscópicas tem sido objeto de estudos há várias décadas. Contudo, com o advento da nanotecnologia e consequente fabricação de materiais com tamanhos nanoscópicos, esta área se tornou bastante atrativa tanto do ponto de vista de novos comportamentos verificados (e uma possível física nova) quanto das possíveis aplicações. Com isso, nesse trabalho serão apresentadas algumas breves revisões bibliográficas no sentido de deixar o texto mais didático. Na sequência, relatar-se-á sobre algumas produções científicas no intuito de evidenciar a evolução das pesquisas realizadas e o seu contexto cronológico.

2. Uma breve revisão sobre fenômenos críticos e transições de fase, Teoria de Landau para Transições de fase de segunda-ordem e Teoria de Ginzburg-Landau (GL)

A fenomenologia da supercondutividade está relacionada aos comportamentos termodinâmicos desses materiais. Dessa forma, é interessante ter-se uma noção sobre fenômenos críticos e transições de fase. Adicionalmente, antes de descrevermos a teoria fenomenológica de Ginzburg-Landau para os supercondutores (SCs), é interessante discutirmos um pouco sobre a teoria de Landau para transições de fase de segunda ordem, já que a GL se originou dela. Dessa forma, na sequência transcrevo um texto introdutório o qual depositei no "arXiv" (https://arxiv.org/ftp/arxiv/papers/1505/1505.01150.pdf).

Fenomenologia da Supercondutividade e Supercondutores Mesoscópicos

Phenomenology of the superconductivity and mesoscopic superconductors

Rafael Zadorosny1, Alice Presotto1, Elwis C. S. Duarte1, Edson Sardella2

1 Departamento de Física e Química, Univ Estadual Paulista – Unesp, CP 31, CEP 15385-000, Ilha Solteira, SP

2 Departamento de Física, Faculdade de Ciências, Univ Estadual Paulista – Unesp, CP 473, CEP 17033-360, Bauru, SP

Resumo

Em geral, quando a teoria fenomenológica de Ginzburg-Landau para supercondutores é trabalhada, pouco se esclarece aos alunos sobre a origem da mesma. Esta tem como base conceitos termodinâmicos como fenômenos críticos e transições de fase que, se devidamente tratados, enriquecem de sobremaneira a aula sobre tal assunto. Assim, neste trabalho apresentamos uma sequência para o desenvolvimento da principal teoria fenomenológica da supercondutividade. Iniciamos com uma breve introdução aos fenômenos críticos e transições de fase e, então, desenvolvemos a teoria de Landau para transições de fase de segunda ordem. Após isso, expomos a teoria de Ginzburg-Landau, e a teoria de Ginzburg-Landau dependente do tempo. Aplicamos esta última para o caso de dois sistemas supercondutores mesoscópicos, um homogêneo e outro com defeitos superficiais. Observa-se que os defeitos interferem de sobremaneira na dinâmica de vórtices do sistema.

Palavras chave: *Ginzburg-Landau, mesoscópico, vórtice, supercondutor*

Abstract

Usually, during the classes, the origin of the phenomenological theory proposed by Ginzburg-Landau is not treated. The fundamentals of such theory are based on thermodynamics concepts like criticality and phase transitions that, if used, could enrich a lot the classes. Thus, in this work we present a sequence for the development of this major phenomenological theory for superconductors. We will begin with a brief introduction to the criticality and phase transitions phenomena e then we will describe the Landau theory for second order phase transitions. After that, we will introduce the Ginzburg-Landau theory and the time-dependent Ginzburg-Landau theory. As an application of this last one, we will study two mesoscopic systems. One of them a homogeneous sample and the other one a sample with surface defects. We show that the defects strongly influences the vortex dynamics of the system.

Keywords: *Ginzburg-Landau, mesoscopic, vortex, superconductor*

1. Introdução

Há mais de cem anos os fenômenos críticos são observados. Esses fenômenos são assim denominados por ocorrerem próximos a um ponto crítico que, por sua vez, pode ser entendido como o ponto do diagrama de fase de um sistema onde a transição de fase é de segunda ordem. Nas suas proximidades, diferentes sistemas comportam-se de modo semelhante, obedecendo a leis de potências cujos expoentes não são inteiros, os denominados expoentes críticos [1, 2].

Várias teorias foram propostas na tentativa de explicar esses fenômenos físicos. Destacamos nesse trabalho a simples, porém elegante teoria para transições de fase de segunda ordem proposta por Landau em 1937 [3]. Tal teoria é baseada na expansão da energia livre do sistema estudado em função do seu parâmetro de ordem. O parâmetro de ordem, por sua vez, é uma quantidade definida como zero em uma fase do sistema (fase desordenada, acima da temperatura crítica) e com valores diferentes de zero em outra (fase ordenada, abaixo da temperatura crítica).

A teoria de Landau nos dá elementos importantes para o desenvolvimento da teoria de Ginzburg-Landau (GL) [4-7] publicada em 1950 a qual descreve satisfatoriamente vários fenômenos relacionados à supercondutividade. Por seu aspecto fenomenológico e simples, os pesquisadores da área receberam, à época de sua publicação, tal trabalho com ceticismo mas, em 1959, quando Gorkov [4] mostrou que as equações GL eram um caso particular da teoria supercondutora de primeiros princípios BCS [8,9], esta se popularizou no meio. Em 1966, Schimid [10] inseriu uma dependência temporal às equações GL e, dessa forma, a dinâmica de sistemas fora do equilíbrio foi possível de ser estudada.

2. Breve abordagem sobre Fenômenos Críticos e Transições de Fase

Todos os fenômenos que ocorrem nas proximidades de um ponto crítico são denominados Fenômenos Críticos (FC). Este ponto, em geral, é o final de uma curva finita que separa duas fases distintas de um sistema, como por exemplo a curva de vaporização da água, que separa o estado líquido do gasoso. Geralmente denotamos por T_C e $P_{C,}$ por exemplo, a temperatura e pressão do ponto crítico. No contorno deste ponto, é possível passar de um estado a outro da matéria (de vapor para líquido, por exemplo) sem haver uma mudança abrupta entre os estados [1]. Este comportamento pode ser descrito por um parâmetro de ordem característico de cada substância. Outro fato interessante é que, embora diferentes sistemas apresentem diferentes fenômenos de transição de fase, na região próxima ao ponto crítico todos têm o mesmo comportamento.

Assim, é possível identificar a ordem das transições de fase pelo comportamento do parâmetro de ordem do sistema. Se esse mudar de forma contínua entre uma fase e outra, a transição é de segunda ordem, mas se for descontínuo, a transição será de primeira ordem. Essa definição é diferente da inserida por Ehrenfest, onde a ordem da transição está relacionada com a ordem da derivada do potencial termodinâmico adequado. Se a primeira derivada for descontínua, a transição será de primeira ordem, mas se a segunda derivada for aquela que apresentar alguma descontinuidade, mantendo-se a primeira derivada contínua, a transição será de segunda ordem e assim por diante. Nos casos analisados nesse trabalho, ambas as definições serão satisfeitas.

Com esta breve noção sobre fenômenos críticos, na próxima seção será analisada a Teoria de Landau para transições de fase de segunda ordem. Por essa teoria, a energia livre do sistema é descrita em termos do parâmetro de ordem nas proximidades do ponto crítico.

3. A Teoria de Landau para transições de segunda ordem

Essa teoria tem por base a expansão da energia livre do sistema (esta pode ser entendida como a energia que este possui e possível de ser transformada em trabalho) em potências do parâmetro de ordem, η, específico de cada sistema. Dessa forma, a continuidade da mudança de estado na transição de fase de segunda ordem é expressa matematicamente pelo fato de η ter valores pequenos perto do ponto crítico. Assim, considerando a vizinhança desse ponto, expandimos a energia livre de Gibbs, por exemplo, em potências de η

$$G = G_0 + \alpha\eta + a\eta^2 + c\eta^3 + b\eta^4 + \ldots \tag{1}$$

onde a expansão foi feita até quarta ordem devido ao baixo valor de η e os coeficientes, α, a, c e b são funções da pressão (P) e da temperatura (T).

Para obtermos η devemos minimizar a energia livre:

$$\frac{\partial G}{\partial \eta} = \alpha + 2a\eta + 3c\eta^2 + 4b\eta^3 = 0 \tag{2}$$

$$\alpha + \eta(2a + 3c\eta + 4b\eta^2) = 0 \tag{3}$$

Com isso, as possíveis soluções para a equação (3) são:

$$\begin{aligned} &\alpha = 0 \quad e \quad \eta = 0 \\ &\alpha = 0 \quad e \quad \eta \neq 0 \end{aligned} \tag{4}$$

De todas as soluções possíveis, vemos que α é sempre zero, independente do valor de η.

Para que a condição de mínimo seja satisfeita, a derivada segunda da energia livre deve ser positiva, com isso temos:

$$\frac{\partial^2 G}{\partial \eta^2} = 2a + 6c\eta + 12b\eta^2 \tag{5}$$

Para $\eta = 0$, que corresponde a $T > T_C$, devido à definição do parâmetro de ordem, temos que a equação (5) só será positiva se a for positivo.

Para $\eta \neq 0$ (ou seja, $T < T_C$), vamos analisar a segunda derivada G desprezando a constante b na equação (3). Obtemos, então, uma expressão para η dada pela equação (6).

$$\eta = -\frac{2a}{3c} \tag{6}$$

Substituindo a equação (6) na equação (5) sem a constante b temos:

$$\frac{\partial^2 G}{\partial \eta^2} = -4a \tag{7}$$

então, para que a equação (7) seja positiva, a constante a deve ser negativa. Assim, já que a é positiva acima de T_C e negativa abaixo dessa temperatura, concluímos que no ponto crítico, ou seja, em T_C, a constante a é nula.

Nessa teoria assume-se que a função *a(P,T)* não apresenta singularidades no ponto crítico, então Landau propôs a seguinte expressão:

$$a = a_0(T - T_C) \tag{8}$$

onde:

$$\begin{aligned} a > 0 \quad & para \quad T > T_C \\ a = 0 \quad & para \quad T = T_C \\ a < 0 \quad & para \quad T < T_C \end{aligned} \tag{9}$$

Reescrevendo a equação (1) e a sua segunda derivada já com $\alpha = 0$ e aplicando-as no ponto crítico temos:

$$G_C = G_0 + c_C\eta^3 + b_C\eta^4 \tag{10}$$

$$\frac{\partial^2 G_C}{\partial \eta^2} = 6c_C\eta + 12b_C\eta^2 \tag{11}$$

Da equação (11) obtemos que se $c_c = 0$, $b_c > 0$. Dessa forma, se $b > 0$ no ponto crítico, ele será positivo para qualquer ponto nas proximidades dessa região.

Resta-nos duas soluções para *c*. Para $c = 0$, significa que há uma linha de pontos críticos no plano *PT*. Porém, se $c \neq 0$, a transição de segunda ordem só ocorrerá em pontos isolados, como em uma transição líquido-gás.

Escolhemos $c = 0$ [3] pois este é o caso mais interessante, onde há uma linha de pontos críticos, o qual é válido para os supercondutores também. Assim a equação (1) adquire a forma:

$$G = G_0 + a_0(T - T_C)\eta^2 + b\eta^4 \tag{12}$$

A Figura 1 mostra duas curvas da equação (12) para valores positivos e negativos do coeficiente *a*. Note que a curva apresenta mínimos locais fora da origem do sistema de coordenadas para $a<0$. Landau também considerou o coeficiente *b* como sendo praticamente constante quando $T \to T_C$.

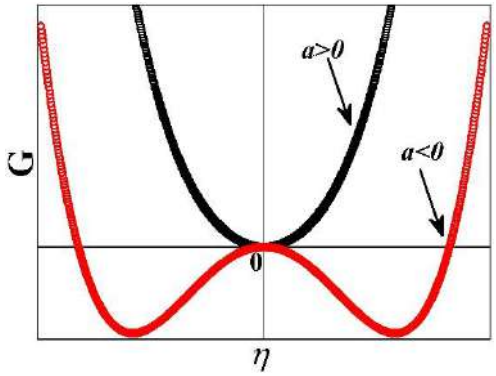

Figura 1: Energia livre de Gibbs em função do parâmetro de ordem η para os valores de *a* da equação (9)

Agora podemos obter uma expressão para η dependente da temperatura próxima ao ponto crítico minimizando a energia livre de Gibbs em relação ao próprio η. Com isso temos:

$$\eta^2 = -\frac{a_0(T - T_C)}{2b} = \frac{|a|}{2b} \tag{13}$$

Desprezando as potências mais altas de η, encontramos a entropia do sistema.

$$S = -\frac{\partial G}{\partial T} = S_0 - a_0\eta^2$$

Com isso temos:

$$\begin{aligned} S &= S_0 && para \quad T > T_C \\ S &= S_0 + \frac{a_0^{\,2}}{2b}(T - T_C) && para \quad T < T_C \end{aligned} \tag{14}$$

No ponto crítico a entropia fica $S = S_0$, ou seja, ela é contínua nesse ponto, como vemos na Figura 2 (a).

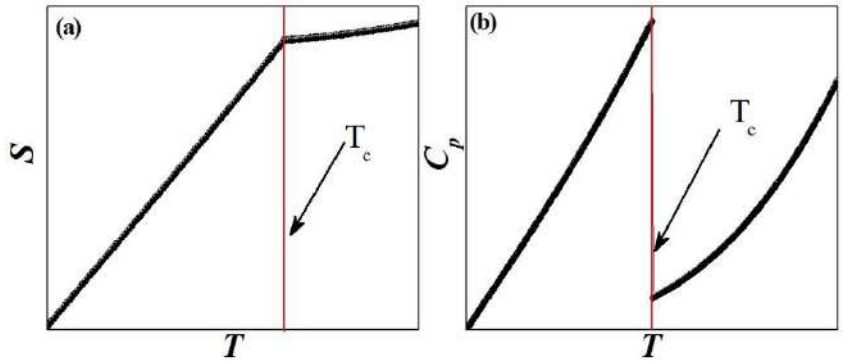

Figura 2: Continuidade da entropia na transição de fase e descontinuidade do calor específico para a mesma transição. Esse comportamento é típico de uma transição de segunda ordem.

O calor específico é dado por:

$$C_P = T\frac{\partial S}{\partial T}\bigg|_P = -T\frac{\partial^2 G}{\partial T^2}\bigg|_P$$

Assim, das equações (14) temos:

$$\begin{aligned} C_P &= C_{P0} && para \quad T > T_C \\ C_P &= C_{P0} + T\frac{a_0^{\,2}}{2b} && para \quad T < T_C \end{aligned} \tag{15}$$

Na Figura 2 (b), é mostrada a descontinuidade do calor específico no ponto crítico.

4. A teoria de Ginzburg – Landau (GL) para supercondutores

A teoria fenomenológica de Ginzburg-Landau (GL) segue a mesma metodologia da teoria de Landau para transições de fase de segunda ordem já que, na ausência de campo magnético, a transição de fase normal-supercondutor também é de segunda ordem. Essa teoria foi publicada em 1950 e uma das motivações de tal trabalho foi a necessidade de descrever a destruição da supercondutividade por um campo magnético ou uma corrente elétrica. Maiores detalhes sobre a teoria GL podem ser obtidos na Ref. 7.

Na teoria GL o parâmetro de ordem do supercondutor é uma função complexa $\Psi(\vec{r})$ que é interpretada como a função de onda "efetiva" dos superelétrons (portadores de carga do estado supercondutor) e $|\Psi(\vec{r})|^2 = n_s$, onde n_s é a densidade dos superelétrons.

$$\Psi(\vec{r}) = |\Psi(\vec{r})| e^{i\phi} = \sqrt{n_s}\, e^{i\phi} \tag{16}$$

Seguindo as mesmas considerações estabelecidas por Landau e analisadas na seção 3, escrevemos a energia livre de Gibbs do supercondutor na ausência de campo magnético, equação 17. É interessante frisar que alguns autores escrevem a energia do estado supercondutor em termos da energia livre de Helmholtz. Porém, esta não leva em consideração o trabalho útil realizado pela magnetização, assim, escreveremos a energia deste estado pela energia livre de Gibbs. Contudo, ao minimiza-las, nota-se que as equações GL independem da energia livre escolhida.

$$G_S = G_n + \int \left\{ \alpha |\Psi|^2 + \frac{\beta}{2} |\Psi|^4 + \frac{1}{4m} \left| -i\hbar \nabla \Psi \right|^2 \right\} d^3 r \tag{17}$$

Onde G_n é a energia livre do estado normal, $\hbar$ é a constante de Planck, β é um coeficiente positivo independente da temperatura (é a constante *b* da teoria de Landau multiplicada por dois), α é função da temperatura dada pela equação (8):

$$\alpha = \alpha_0 (T - T_C) \tag{18}$$

sendo T_C a temperatura crítica acima da qual o material vai para o estado normal e o coeficiente $\frac{1}{4m} \left| -i\hbar \nabla \Psi \right|^2$ é a densidade de energia cinética dos superelétrons inserida na expansão da energia livre pelo fato do parâmetro de ordem do supercondutor ser dependente da posição.

Na presença de campo magnético, a equação (17) deve ser corrigida por dois termos:

- A densidade de energia magnética, dada por $\frac{B^2}{8\pi} - \vec{H} \bullet \vec{M}$, onde $\vec{B}$ é o campo de indução magnética que no interior do supercondutor é zero e assume o valor do campo magnético aplicado, $\vec{H}$, no estado normal e, por fim, $\vec{M}$ é a magnetização do material supercondutor, ou seja, $\vec{M} = 0$ para $T > T_C$ (estado normal) e $\vec{M} = -\frac{\vec{H}}{4\pi}$ para $T < T_C$. Note que estamos trabalhando no sistema cgs.
- A substituição do operador $-i\hbar\nabla$ por $-i\hbar\nabla - \frac{2e}{c}\vec{A}$, onde 2*e* é a carga do superelétron, $\vec{A}$ é o potencial vetor e *c* a velocidade da luz.

Com isso a equação (17) adquire a forma:

$$G_S = G_n + \int \left\{ \alpha |\Psi|^2 + \frac{\beta}{2} |\Psi|^4 + \frac{1}{4m} \left| -i\hbar \nabla \Psi - \frac{2e}{c} \vec{A} \Psi \right|^2 + \frac{B^2}{8\pi} - \vec{H} \bullet \vec{M} \right\} d^3 r \tag{19}$$

Minimizando G_s com relação a $\delta\Psi^*$ obtemos a primeira equação GL e sua condição de contorno:

$$\alpha \Psi + \beta \Psi |\Psi|^2 + \frac{1}{4m} \left(-i\hbar \nabla - \frac{2e}{c} \vec{A} \right)^2 \Psi = 0 \tag{20}$$

$$\left(-i\hbar \nabla \Psi - \frac{2e}{c} \vec{A} \Psi \right) \bullet \vec{n} = 0 \tag{21}$$

onde $\vec{n}$ é o vetor normal à superfície do supercondutor.

A equação (21) nos diz que não há supercorrentes passando pela interface normal – supercondutor. A minimização de G_S com respeito a Ψ dá o complexo conjugado da equação (20). Resta-nos, então, minimizar G_S em relação ao potencial vetor $\vec{A}$. Assim, obtemos a segunda equação de GL.

$$\nabla \times \nabla \times \vec{A} = -\frac{2\pi i\hbar e}{mc}\left(\Psi^*\nabla\Psi - \Psi\nabla\Psi^*\right) - \frac{8\pi e^2}{mc^2}\vec{A}|\Psi|^2 \qquad (22)$$

Esta equação ainda pode ser reescrita usando a lei de Ampère, $\nabla \times \vec{B} = \nabla \times \nabla \times \vec{A} = \frac{4\pi}{c}\vec{J}_S$, adquirindo a forma:

$$\vec{J}_S = -\frac{i\hbar e}{2m}\left(\Psi^*\nabla\Psi - \Psi\nabla\Psi^*\right) - \frac{2e^2}{mc}\vec{A}|\Psi|^2 \qquad (23)$$

Embora as equações GL sejam provenientes de uma teoria fenomenológica simples, elas nos permitem descrever uma gama de propriedades relacionadas aos supercondutores. Não demonstraremos neste trabalho mas, utilizando algumas considerações e aplicando-as nas equações GL, obtém-se a quantização do campo magnético e os comprimentos característicos dos supercondutores, ou seja, a profundidade de penetração de London, λ, e o comprimento de coerência, ξ.

O λ é devido ao fato de que, embora o supercondutor exclua o campo magnético de seu interior, as correntes que o blindam se distribuem por uma certa região de espessura λ. Consequentemente, o fluxo magnético não cai abruptamente para zero dentro do supercondutor, mas sim ele o penetra decaindo ao longo da distribuição das correntes de blindagem. Dessa forma, λ é conhecido por profundidade de penetração e nos indica o quanto o fluxo magnético (ou, o campo magnético) penetra no supercondutor.

Já o conceito de ξ foi formulado em 1953 por Pippard [11,12]. Ele considerou que a densidade de superelétrons não poderia variar rapidamente com a posição, mas variaria apreciavelmente dentro de uma certa distância. Uma conseqüência da existência de ξ é que o contorno entre uma região normal e uma região supercondutora deve ter uma largura finita (i.e., não nula), pois a densidade de superelétrons varia de zero na primeira região até um valor máximo n_S dentro do supercondutor sendo, então, ξ, uma medida da espessura dessa região de variação. A razão λ/ξ é conhecida por parâmetro de GL, κ, e, em geral, independe de T. Este parâmetro é muito importante no cálculo da densidade de energia superficial, σ. Esta, contudo, se anula para $\kappa = 1/\sqrt{2}$ e pode assumir valores positivos e negativos. Com isso, os supercondutores são divididos em duas classes: os do tipo I (SCI), para $\kappa < 1/\sqrt{2}$, onde σ > 0, e os do tipo II (SCII), para $\kappa > 1/\sqrt{2}$, onde σ < 0. Neste último caso, torna-se energeticamente favorável a penetração de fluxo quantizado (Φ_0) no interior dos SCII. Estes *fluxóides* possuem um núcleo de material normal e supercorrentes fluem ao seu redor para confinar o fluxo em tal região que, por sua vez, possui raio igual a ξ. Assim, ao conjunto núcleo normal mais supercorrentes denominamos por vórtice (ver inset do painel inferior da Figura 3). Nos painéis principais da Figura 3, são mostrados os comportamentos magnéticos típicos dos SCI (superior) e SCII (inferior). Neste último, o estado misto está caracterizado por uma exemplificação de rede triangular de vórtices, ou seja, a rede de Abrikosov, como será descrito no próximo parágrafo. Os insets do painel superior exemplificam as curvas de λ e ξ para as situações onde $\kappa < 1/\sqrt{2}$ (painel (a)) e $\kappa > 1/\sqrt{2}$ (painel (b)).

Em 1952, dois anos após a publicação da teoria GL, Alexei Abrikosov, começou a estudar o caso de supercondutores com $\kappa > 1/\sqrt{2}$. Nesse estudo, Abrikosov descobriu que para essa classe de supercondutores, acima de certo campo crítico inferior, H_{C1}, se torna energeticamente favorável a presença de vórtices no interior dos materiais. Além disso, ele previu que conforme o campo externo aumenta sua intensidade, os vórtices se dispõem em uma rede triangular, hoje conhecida por rede de Abrikosov (ver exemplificação no painel inferior da Figura 3). À medida que o campo externo aumenta, os vórtices se tornam mais próximos uns dos outros e começam a se sobrepor. No campo denominado H_{C2}, os núcleos dos vórtices estão totalmente sobrepostos e o estado supercondutor é destruído.

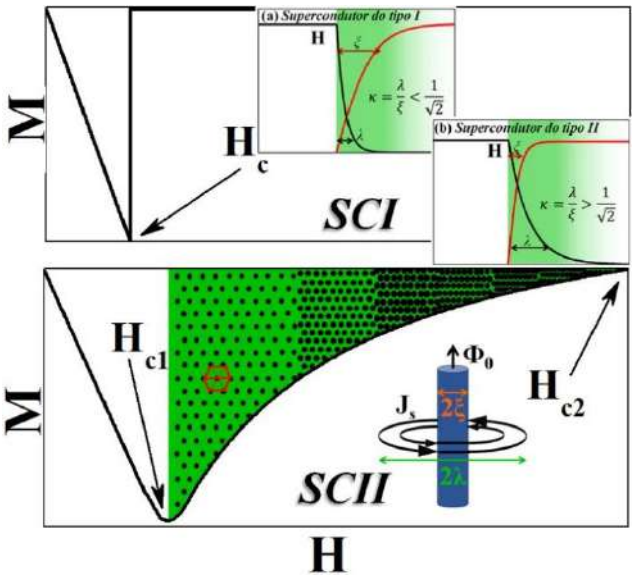

Figura 3: Painel superior exemplifica a resposta magnética de um SCI por uma curva de magnetização em função do campo magnético externo aplicado. No painel inferior, é exemplificada a resposta de um SCII onde o estado misto é caracterizado pela presença de vórtices que se arranjam formando a rede de Abrikosov. Os insets mostram as curvas típicas da penetração do campo magnético (medida por λ) e da variação do parâmetro de ordem (medido por ξ) para os SCI (a) e SCII(b).

Essas previsões ficaram "engavetadas" até 1957 quando Abrikosov finalmente as publicou. Em 2003 ele foi laureado com o prêmio Nobel de Física, que dividiu com Vitaly Ginzburg e Anthony Leggett – o primeiro é o G da teoria GL, o segundo trabalhou com condensação de Bose-Einstein, trabalho que motivou Landau, orientador de Abrikosov, a reunir o seu grupo para dizer que Feynmam, um dos pesquisadores dessa área, havia resolvido o problema de superfluidez. Foi exatamente esse fato que despertou Abrikosov e incentivou sua publicação [10, 11].

5. A teoria de Ginzburg – Landau dependente do tempo (TDGL) e supercondutores mesoscópicos

Em 1966, Schmid publicou um trabalho onde atribuída uma taxa de variação temporal ao parâmetro de ordem e ao potencial vetor na teoria GL. As equações resultantes ficaram conhecidas por TDGL (time-dependent Ginzburg-Landau) [13]. Dessa forma, há a possibilidade de acompanhar a evolução dos vórtices em estados metaestáveis, ou seja, estados entre dois estados estacionários consecutivos. Schmid também fez a inclusão do potencial escalar elétrico que descreve um sistema supercondutor na presença de uma corrente de transporte.

A 1ª equação TDGL é

$$\frac{\hbar^2}{2m_s D}\left(\frac{\partial}{\partial t} + i\hbar e_s \Phi\right)\Psi = -\frac{\delta G_s}{\delta \Psi} \tag{24}$$

e a 2ª equação TDGL

$$\beta\left(\nabla\Phi + \frac{\partial \vec{A}}{\partial t}\right)\Psi = -\frac{\delta G_s}{\delta \vec{A}} \tag{25}$$

onde, Φ é o potencial escalar, β é a condutividade elétrica, D é um coeficiente de difusão, o termo entre parênteses em (25) é o campo elétrico, **E**, de acordo com a lei de Faraday.

O lado direito das equações (24) e (25) correspondem, respectivamente, à 1ª e à 2ª equações GL. A equação (25) também pode ser descrita em termos das densidades de correntes, que fica da seguinte forma:

$$\vec{J} = \beta\vec{E} + \vec{J}_s \tag{26}$$

Muitas vezes é interessante trabalhar com as equações TDGL em sua forma adimensional. Com isso, as distâncias estão em unidades de ξ(0), os campos em termos de $H_{C2}(0)$, T em unidade de T_C e o tempo em unidades do tempo característico $t_0 = \pi\hbar/8k_BT_C$, com k_B a constante de Boltzmann.

$$\left(\frac{\partial}{\partial t} + i\Phi\right)\Psi = -\left(i\nabla - \vec{A}\right)^2\Psi + (1-T)\Psi\left(1-|\Psi|^2\right) \tag{27}$$

$$\beta\left(\nabla\Phi + \frac{\partial\vec{A}}{\partial t}\right) = (1-T)\Re\left[\Psi^*(-i\nabla - \vec{A})\Psi\right] - \kappa^2\nabla\times\nabla\times\vec{A} \tag{28}$$

onde $\vec{B} = \nabla\times\vec{A}$ é o campo a magnético local e, β é a condutividade elétrica, κ é o parâmetro de Ginzburg-Landau e Φ é o potencial escalar. A densidade de supercorrente é dada por:

$$\vec{J}_s = (1-T)\Re\left(\Psi^*(-i\nabla - \vec{A})\Psi\right) \tag{29}$$

Esta teoria tem sido muito usada para o estudo de supercondutores mesoscópicos. Tais materiais tem dimensões da ordem de λ e, por serem muito pequenos, efeitos de confinamento dominam a dinâmica de vórtices e alteram de sobremaneira os comportamentos dos supercondutores quando comparados a materiais volumétricos, os ditos bulks [16-18]. De uma forma geral, no estado estacionário os vórtices, que nos materiais bulk se arranjam numa rede triangular, a rede de Abrikosov, nos mesoscópicos a influência da superfície é tão considerável que o arranjo dos vórtices passa a seguir a simetria do sistema [19,20]. Outro comportamento exótico é a formação de vórtices gigantes, i.e., vórtices que possuem mais do que um quantum de fluxo magnético em seu núcleo [17,20]. Na Figura 4 são mostradas a variação de Ψ ao longo de dois sistemas mesoscópicos quadrados de tamanhos laterais de 12ξ(0) simulados em $T=0{,}1T_c$. Um deles é uma amostra homogênea, sem qualquer defeito, Figura 4(a) e (c). No outro, Figura 4(b) e (d), foram inseridos cinco defeitos em uma das superfícies do mesmo. Estes defeitos tem largura e profundidade de 0,25ξ(0). Na Figura 4(a) e (b) é mostrado um estado não estacionário durante a primeira penetração e, nos respectivos insets, o estado estacionário. Note que no sistema homogêneo, dois vórtices penetram ao mesmo tempo enquanto que no sistema com defeitos, ocorre a penetração de apenas um vórtice. As linhas pretas em tais imagens indicam as correntes de blindagem. Note que estas se deformam ao contornar os defeitos e geram um acúmulo local de linhas de corrente o que, consequentemente, causa um aumento local na corrente crítica do material. Este efeito é conhecido por "current crowding" [21]. Na Figura 4 (c) e (d) são mostrados os arranjos dos vórtices no dois sistemas. Note que, enquanto no sistema homogêneo os vórtices penetrados se arranjam de tal forma a repetir a simetria deste (contorno quadrado), no sistema com defeitos o arranjo é totalmente alterado. Isto mostra que mesmo defeitos muito pequenos podem gerar grandes alterações em sistemas mesoscópicos, tanto na dinâmica de penetração de vórtices quanto no arranjo dos mesmos.

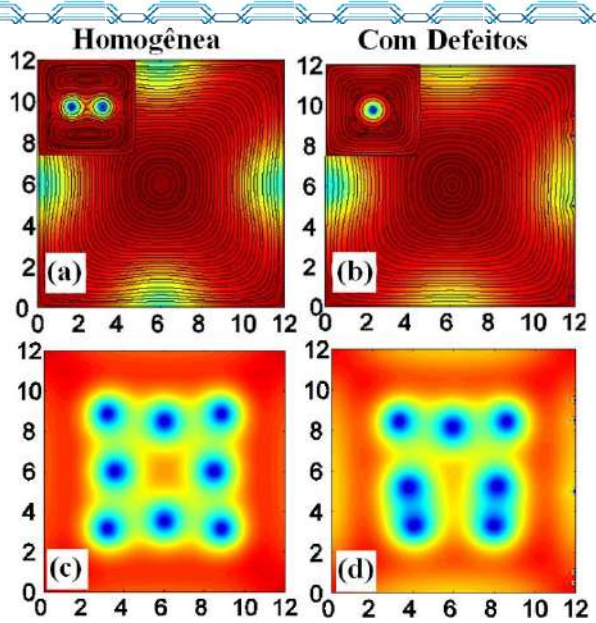

Figura 4: Mapeamento de Ψ ao longo de dois sistemas mesoscópicos de tamanho lateral 12ξ(0). Na simulação foi usado κ=5, que equivale à uma liga Pb-In, com λ = 150 nm, ξ = 30 nm e T_C=7.0 K [5]. Em (a) é mostrado o estado não estacionário da primeira penetração para uma amostra homogênea e o inset mostra o respectivo estado estacionário. Em (b) o mesmo comportamento é mostrado, porém, para um sistema com cinco defeitos em uma das superfícies da amostra. As linha que contornam tais imagens representam as correntes de blindagem onde, no contorno dos defeitos surgem o efeito de acúmulo das linhas de corrente. Em (c) e (d) são mostrados os arranjos dos vórtices para o sistema homogêneo e com defeitos, respectivamente.

Conclusão

Iniciamos nossa análise definindo o conceito de ponto crítico e identificando que, na vizinhança deste, a transição de fase é de segunda ordem. Nesse contexto analisamos a teoria de Landau para tais transições. Esta é baseada na expansão da energia livre do sistema em termos do seu parâmetro de ordem.

Com base na teoria de Landau, introduzimos a teoria fenomenológica de Ginzburg – Landau (GL). Esta é uma importante teoria capaz de explicar muitas características apresentadas pelos supercondutores. Por ela, obtém-se os comprimentos característicos dos supercondutores, i.e., a profundidade de penetração, λ, e o comprimento de coerência, ξ. A razão do primeiro pelo segundo é o parâmetro de Ginzburg-Landau, κ. Assim, para $\kappa < 1/\sqrt{2}$, a energia superficial é positiva, e tem-se os supercondutores do tipo I; por outro lado, para $\kappa > 1/\sqrt{2}$, a energia superficial é negativa, o que define os supercondutores do tipo II. Esses últimos, além de apresentarem exclusão total de fluxo magnético do seu interior até um campo crítico inferior H_{C1}, acima deste passa a ser energeticamente favorável a penetração de fluxo quantizado (os vórtices), em seu interior. Esse estado misto, onde há a convivência de estado normal com o estado supercondutor, perdura até um campo crítico superior denominado H_{C2}, acima do qual há a transição do estado supercondutor para o estado normal. Em 1966, com a inserção da variação temporal na teoria GL, conhecida como TDGL, foi possível estudar regimes dinâmicos em sistemas supercondutores. Assim, como exemplificação, analisamos dois sistemas mesoscópicos, sendo um deles homogêneo e o outro com defeitos superficiais. Nota-se que, mesmo pequenos, com cerca de 1/4 do raio de um vórtice, os defeitos interferem de sobremaneira na dinâmica de vórtices do sistema.

Agradecimentos

Agradecemos à Fapesp, processo n° 2013/17719-8, pelo apoio financeiro.

Referências

1. H. E. Stanley. *Introdution to Phase Transitions and Critical Phenomena*, Oxford University Press, 1971; L. P. Kadanoff, W. Götze, D. Hamblen, R. Hecht, E. A. S. Lewis, V. V. Palciauskas, M. Rayl, J. Swift, D. Aspnes, J. Kane, Rev. Mod. Phys. **39**, 395 (1967)
2. P. Pfetuty, G. Toulouse, *Introdution to the Renormalization Group and to Critical Phenomena*, John Wiley & Sons Ltd, 1977

3. L. D. Landau, E. M. Lifshitz, *Statistical Physics*, Parte 1, 3ª edição, Pergamon Press, 1980
4. L. D. Landau, E. M. Lifshitz, *Statistical Physics*, Parte 2, Pergamon Press, 1980
5. C. P. Poole, H. A. Farach, R. J. Creswick, *Superconductivity*, Academic Press, 1995
6. V. V. Schmidt, *The Physics of Superconductors*, Spring-Verlag, 1997
7. S. H. Pereira, M. G. Félix, Revista Brasileira de Ensino de Física **35**, n.1, 1313 (2013)
8. F. Ostermann, L. M. Ferreira, C. J. H. Cavalcanti, Revista Brasileira de Ensino de Física **20**, n.3, (1998); M. B. S. Costa, A. C. Pavão, Revista Brasileira de Ensino de Física 34, n.2, 2602 (2012)
9. F. Ostermann, P. Pureur, Supercondutividade. 1. ed. São Paulo: Livraria da Física, 2005. v. 1. 78p.
10. A. A. Schimid, Phys. Kondens. Materie **5**, 302 (1966)
11. *Os Superelétrons são os portadores de carga dos materiais supercondutores. São conhecidos também por pares de Cooper e são formados pela interação atrativa, mediada por fônons, entre dois elétrons com spins e momentos lineares opostos.*
12. A. B. Pippard, *Physica* 19, 765, 1973.
13. A. C. Rose-Innes, E. H. Rhoderick, *Introdution to Supercondutivity*, Pergamon Press, 1978.
14. NOBEL PRIZE. *The Nobel Prize in Physics 2003*. Disponível em: < http://www.nobelprize.org/nobel_prizes/physics/laureates/2003/>. Acesso em: 04 nov. 2014.
15. L. C. Ortiz, *Prêmio Nobel de Física de 2003*, Ciência e Tecnologia em São Carlos, nº 1, 2003.
16. R. Zadorosny, E. Sardella, A. L. Malvezzi, P. N. Lisboa-Filho, W. A. Ortiz, Phys. Rev. B **85**, 214511 (2012)
17. E.Sardella, A. L. Malvezzi, P. N. Lisboa-Filho, W. A. Ortiz, Phys. Rev. B **74**, 014512 (2006)
18. L. F. Chibotaru, A. Ceulemans, V. Bruyndoncx, V. V. Moshchalkov, Nature **408**, 833 (2000)
19. B. J. Baelus and F. M. Peeters, Phys. Rev. B **65**, 104515 (2002)
20. B. Xu, M. V. Milošević, Shi-Hsin Lin, F. M. Peeters, B. Jankó, Phys. Rev. Lett. **107**, 057002 (2011)
21. J. R. Clem, K. K. Berggren, Phys. Rev. B **84**, 174510 (2011)

3. Dinâmica de penetração de fluxo magnético em supercondutores

Meus trabalhos com dinâmica de vórtices iniciaram no doutorado, onde, embora não trabalhasse com amostras nanoscópicas (ou mesoscópicas, como indicado no texto anteriormente apresentado), usava-se amostras nanoestruturadas. As nanoestruturas consistiam de uma rede regular de buracos (muitas vezes denominados por antidots, ADs). Em um primeiro trabalho, utilizamos a recém instalada estação de magneto-ótica do Grupo de Supercondutividade e Magnetismo, GSM-UFSCar, para estudar penetração de avalanches de fluxo magnético. Uma das constatações que tivemos é de que a presença da rede ADs guia o fluxo em sua penetração abrupta (avalanche de fluxo) e a morfologia apresentada depende do espaçamento entre os ADs. Além disso, a geometria dos ADs (demonstrado mais tarde, em um artigo do grupo[1]) também é fator de grande influência na morfologia das avalanches de fluxo. Isso se deve ao fata das correntes que circundam os ADs se acumularem nos vértices dos mesmos. Assim, uma maior corrente local, gera uma maior força de Lorentz no fluxo dentro do AD e, com isso, esse fluxo seguirá pelo sentido ditado por tal força.

Em um outro trabalho nessa linha, demonstramos que, sob baixos campos AC, as avalanches de vórtices reutilizam os mesmos canais para entrarem e saírem da amostra. Essa foi a primeira vez que tal comportamento foi verificado. O mesmo era inesperado pelo fato das avalanches de fluxo magnético serem processos estocásticos[2].

[1] M. Motta et all., Phys. Rev. B 89, 134508 (2014)
[2] F. Colauto et all., IEEE Trans. App. Supercond. 25, 7500704 (2015)

J Supercond Nov Magn (2013) 26:2285–2288
DOI 10.1007/s10948-012-1429-0

ORIGINAL PAPER

Morphology of Flux Avalanches in Patterned Superconducting Films

R. Zadorosny · F. Colauto · M. Motta · T.H. Johansen · R. Dinner · M. Blamire · G.W. Ataklti · V.V. Moshchalkov · A.V. Silhanek · W.A. Ortiz

Received: 15 November 2011 / Accepted: 10 January 2012 / Published online: 10 February 2012

Abstract It is well known that under certain circumstances, magnetic fields applied perpendicularly to the plane of superconducting films can trigger flux avalanches. In such cases, the penetration has a tree-like profile. However, in samples where a regular array of antidots, ADs, is present, the avalanches follow the rows of ADs as if they were guiding lines for the abrupt penetration. In this work, we used the magnetooptical imaging technique to study the morphology of flux avalanches in two Nb films with a square lattice of square ADs, each one with a different lateral size, and a plain film for reference. We show that the morphology of the flux avalanches is greatly influenced by the size of the interstitial region.

Keywords Flux avalanches · Magnetooptical imaging · Antidots

R. Zadorosny (✉)
Departamento de Física e Química, Faculdade de Engenharia de Ilha Solteira, Univers Estadual Paulista-UNESP, Caixa Postal 31, 15385-000, Ilha Solteira, SP, Brazil
e-mail: rafazad@dfq.feis.unesp.br

F. Colauto · M. Motta · W.A. Ortiz
Grupo de Supercondutividade e Magnetismo, Departamento de Física, Universidade Federal de São Carlos, 13565-905, São Carlos SP, Brazil

T.H. Johansen · W.A. Ortiz
Centre for Advanced Study, Norwegian Academy of Science and Letters, 0271 Oslo, Norway

T.H. Johansen
Department of Physics, University of Oslo, POB 1048, Blindern, 0316 Oslo, Norway

R. Dinner · M. Blamire
Department of Materials Science, Cambridge University, Pembroke Street, Cambridge CB2 3QZ, UK

G.W. Ataklti · V.V. Moshchalkov · A.V. Silhanek
INPAC—Institute for Nanoscale Physics and Chemistry, Nanoscale Superconductivity and Magnetism Group, Katholieke Universiteit Leuven, Celestijnenlaan 200D, 3001 Leuven, Belgium

A.V. Silhanek
Département de Physique, Université de Liège, 4000 Sart Tilman, Belgium

1 Introduction

Type II superconductors brought to the mixed state by an external applied magnetic field are expected to exhibit a gradient in vortex concentration, which decreases smoothly from the edge to the center of the sample.

However, under certain circumstances, magnetic fields applied perpendicularly to the plane of superconducting films can trigger flux avalanches [1, 2]. These events can be detected by isothermal dc-magnetization (DCM) measurements, as jumps in the magnetic response, and have a close correspondence with abrupt penetration of bundles of vortices observed through magneto-optical imaging (MOI) [3–5]. Since in this case, the flux distribution is highly inhomogeneous, MOI is a very suitable technique to investigate such phenomenon.

Although the insertion of pinning centers is known to be an effective way to avoid the dissipative movement of vortices, it has been demonstrated that thin films decorated with arrays of antidots (ADs) are also subject to the occurrence of avalanches, which follow the rows of ADs as if they were guiding lines for the abrupt penetration [6].

In this work, we have used DCM and MOI techniques to compare the morphology of flux avalanches in three super-

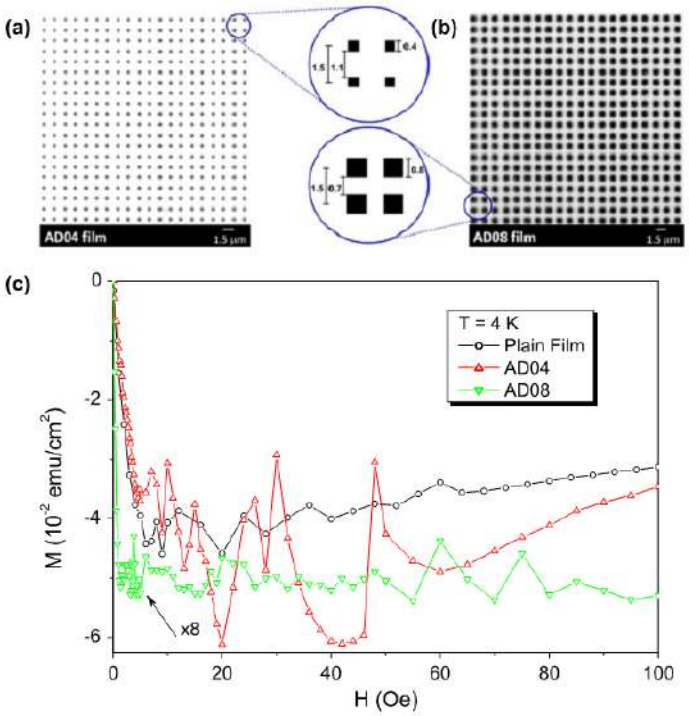

Fig. 1 The *top panels* are schematic pictures of the arrays of ADs for samples AD04 (**a**) and AD08 (**b**). Panel (**c**) shows isothermal magnetization versus applied magnetic field curves for the three samples studied, for $T = 4$ K. Noticeably, at this temperature all samples present signatures of the avalanches (jumps)

conducting films. One is a plain specimen, taken as a reference film, and the other two are patterned films with interstitial regions of different sizes.

2 Materials and Methods

We carried out our investigation with three Nb films of thickness of $t = 50$ nm. Two are patterned films with a square array of square ADs fabricated by electron beam lithography and subsequent lift-off. The Nb was deposited via dc sputtering on top of a SiO_2 insulating substrate. The period of the patterns is $w = 1.5$ μm which correspond to a commensurability field $H_1 = 9.2$ Oe [7–9] at which the densities of vortices and ADs match each other. To have different sizes of the interstitial region, in one film the ADs were fabricated with lateral size of 0.4 μm, and the other with 0.8 μm, as shown schematically in Fig. 1(a) and (b). The samples were named AD04 and AD08, respectively, according to the lateral size of the ADs. The third sample is a plain film taken as a reference specimen. The surface areas are 6.6 mm^2 for the plain film, 6.9 mm^2 for sample AD04, and 7.4 mm^2 for sample AD08. As the areas of the films are similar, their magnetic response could be compared in relative terms, without concern with corrections related to the demagnetizing factors.

Isothermal DCM measurements were carried out in a commercial Quantum Design magnetometer MPMS-5S. For all samples, H was applied perpendicularly to the film plane. To visualize the flux penetration, we used the MOI technique, based on the Faraday effect presented by Bi-substituted yttrium iron garnet films (Bi:YIG) with in plane magnetization [10], which serve as magnetic field sensors. The MOI measurements were performed for low H after a zero field cooled, ZFC, procedure.

3 Results and Discussion

When a superconductor is invaded by flux avalanches, such abrupt penetration can be detected by jumps in DCM measurements. DCM versus applied magnetic field curves, $M(H)$, for all samples are shown in Fig. 1(c), at $T = 4$ K. At this temperature, all samples exhibit flux avalanches. For better visualization, data for sample AD08 was multiplied by a factor 8. This quite low magnetization amplitude for sample AD08 is due to the fact that the ADs are so large—more than a quarter of the film area is missing—that screening capability of the sample is largely suppressed, which reflects in a small diamagnetic response. From panel (c) in Fig. 1, one can also verify that the field for which the first avalanche occurs depends on the existence of an AD lattice, as well as on the size of the ADs, i.e., in sample AD08 the first avalanche is triggered for a magnetic field lower than for the sample AD04 which, in turn, is lower than that

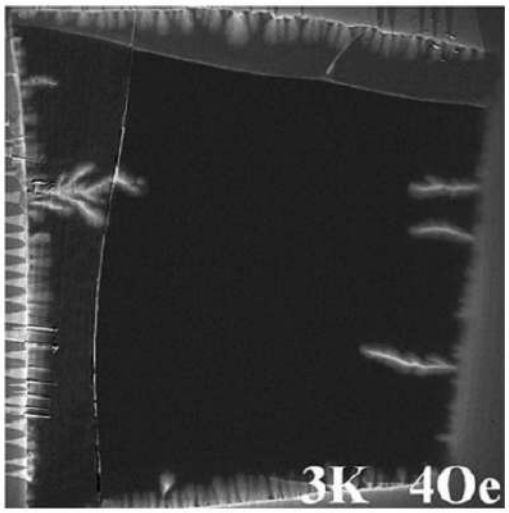

Fig. 2 MO image of flux avalanches for the plain film after a ZFC procedure, to $T = 3$ K, after which a magnetic field of $H = 4$ Oe was applied

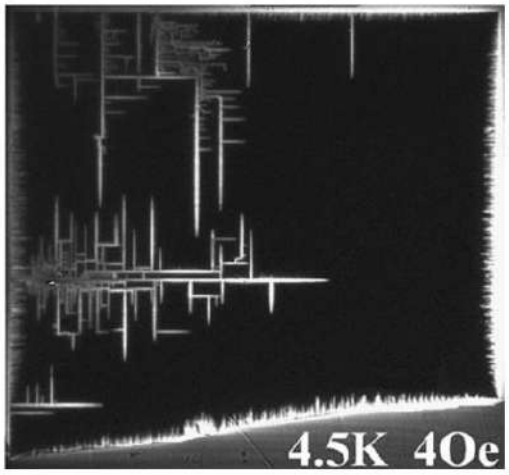

Fig. 3 MO image of flux avalanches for sample AD04 film after a ZFC procedure to $T = 4.5$ K, after which a magnetic field of $H = 4$ Oe was applied

for the plain film. Such behavior indicates that the ADs are avalanche inducers [11, 12].

The pictures obtained by the MOI technique were taken after submitting the samples to a ZFC procedure. For the plain film at $T = 3$ K, as shown in Fig. 2, avalanches develop quite freely. At appropriate values of T and H, both patterned films are invaded by avalanches, as shown in Figs. 3 and 4 for samples AD04 and AD08, respectively. As a matter of fact, the presence of an array of ADs extends the occurrence of avalanches to higher temperatures and applied fields, as compared to the behavior of the plain film,

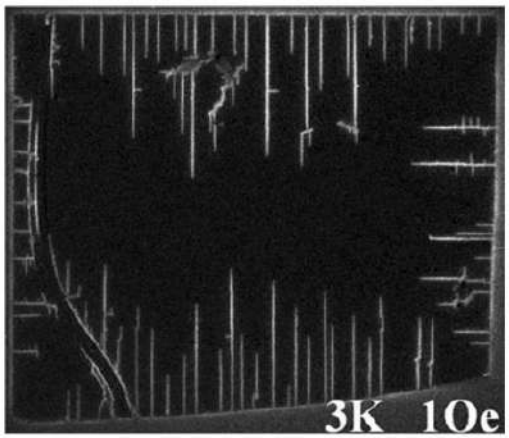

Fig. 4 MO image of flux avalanches for sample AD08, after a ZFC procedure to $T = 3$ K after which a magnetic field of $H = 1$ Oe was applied

in accordance with the description by Hebert and coworkers [13].

Another difference between patterned and plain films is the morphology of the avalanches, as presented in Figs. 2, 3, and 4. It should be noticed that such differences are consistently present throughout the whole region in the HT diagram where thermo-instabilities trigger avalanches. The values of field and temperature for the MO images shown in this paper were chosen in order to emphasize the feature. While in the plain film the spatial shape of the avalanches develops quite freely, in the patterned ones flux penetration is guided by the array of ADs. However, for the sample with smaller ADs, i.e., with the larger interstitial region, the penetration path draws a grid resembling the lattice of ADs, while for the sample with the larger ADs (smaller interstitial region) avalanches rush essentially straight. The reason for this is the enormous difference on the critical current density, J_c, which is stronger in AD04 than in AD08, as already pointed out earlier, when we discussed the amplitude of the magnetization for both samples (Fig. 1(c)). It is an experimental fact that avalanches occur in films with high J_c, since such samples shield more magnetic flux, implying in an increase of the external magnetic pressure over the normal-superconducting interface. In such cases, flux avalanches are triggered, and during their abrupt penetration, finger-like channels are formed, perpendicularly to the sample surface (and so to the shielding currents, since these avalanches are driven by the Lorentz force acting on entering vortices). Around this main fingers, supercurrents flow to shield the neighboring superconducting region. If the magnetic pressure is high inside this main finger, avalanches would be triggered from those channels into the superconducting sea, forming secondary branches that would have the profile shown in Fig. 3 for AD04. On the other hand, the

substantially smaller J_c of sample AD08 seems to be too low to trigger further abrupt bursts of flux invasion, and no secondary avalanches appear.

4 Conclusions

The present study enabled us to conclude that arrays of ADs in superconducting films act as inducers of flux avalanches, whose morphology is related to the shielding capability of the sample, and consequently, with the shape and relative size of the avenues of superconducting material forming the interstitial regions.

Acknowledgements This work was partially supported by the Methusalem Funding of the Flemish Government, the NES-ESF program, the Belgian IAP, the Fund for Scientific Research-Flanders (FWO-Vlaanderen), the UK Engineering and Physical Sciences Research Council, and by the Brazilian funding agencies FAPESP and CNPq. AVS is grateful for the support from the FWO-Vlaanderen. THJ acknowledges the financial support of the Norwegian Research Council.

References

1. Johansen, T.H., Baziljevich, M., Shantsev, D.V., Goa, P.E., Galperin, Y.M., Kang, W.N., Kim, H.J., Choi, E.M., Kim, M.-S., Lee, S.I.: Supercond. Sci. Technol. **14**, 726 (2001)
2. Denisov, D.V., Rakhmanov, A.L., Shantsev, D.V., Galperin, Y.M., Johansen, T.H.: Phys. Rev. B **73**, 014512 (2006)
3. Menghini, M., Wijngaarden, R.J., Silhanek, A.V., Raedts, S., Moshchalkov, V.V.: Phys. Rev. B **71**, 104506 (2005)
4. Colauto, F., Choi, E.M., Lee, J.Y., Lee, S.I., Yurchenko, V.V., Johansen, T.H., Ortiz, W.A.: Supercond. Sci. Technol. **20**, L48 (2007)
5. Colauto, F., Patino, E.J., Blamire, M.G., Ortiz, W.A.: Supercond. Sci. Technol. **21**, 045018 (2008)
6. Menghini, M., Wijngaarden, R.J., Silhanek, A.V., Raedts, S., Moshchalkov, V.V.: Phys. Rev. B **71**, 104506 (2005)
7. Harada, K., Kamimura, O., Kasai, H., Matsuda, T., Tonomura, A., Moshchalkov, V.V.: Science **274**, 1167 (1996)
8. Reichhardt, C., Zimányi, G.T., Scalettar, T., Hoffmann, A., Schuller, I.K.: Phys. Rev. B **64**, 052503 (2001)
9. Silhanek, A.V., Van Look, L., Jonckheere, R., Zhu, B.Y., Raedts, S., Moshchalkov, V.V.: Phys. Rev. B **72**, 014507 (2005)
10. Helseth, L.E., Solovyev, A.G., Hansen, R.W., Ilyashenko, E.I., Baziljevich, M., Johansen, T.H.: Phys. Rev. B **66**, 064405 (2002)
11. Motta, M., Zadorosny, R., Colauto, F., Ortiz, W.A., Johansen, T.H., Dinner, R.B., Blamire, M.G., Ataklti, G.W., Moshchalkov, V.V., Silhanek, A.V.: Phys. Rev. B (submitted)
12. Silhanek, A.V., Raedts, S., Moshchalkov, V.V.: Phys. Rev. B **70**, 144504 (2004)
13. Hébert, S., Van Look, L., Weckhuysen, L., Moshchalkov, V.V.: Phys. Rev. B **67**, 224510 (2003)

PHYSICAL REVIEW B 84, 214529 (2011)

Visualizing the ac magnetic susceptibility of superconducting films via magneto-optical imaging

M. Motta,[1] F. Colauto,[1] R. Zadorosny,[1,*] T. H. Johansen,[2,3] R. B. Dinner,[4] M. G. Blamire,[4] G. W. Ataklti,[5] V. V. Moshchalkov,[5] A. V. Silhanek,[5,6] and W. A. Ortiz[1,3]

[1]*Departamento de Física, Universidade Federal de São Carlos, 13565-905 São Carlos, SP, Brazil*
[2]*Department of Physics, University of Oslo, POB 1048, Blindern, NO-0316 Oslo, Norway*
[3]*Centre for Advanced Study, Norwegian Academy of Science and Letters, NO-0271 Oslo, Norway*
[4]*Department of Materials Science, University of Cambridge, Pembroke Street, Cambridge CB2 3QZ, UK*
[5]*INPAC - Institute for Nanoscale Physics and Chemistry, Nanoscale Superconductivity and Magnetism Group, Katholieke Universiteit Leuven, Celestijnenlaan 200D, B-3001 Leuven, Belgium*
[6]*Département de Physique, Université de Liège, B-4000 Sart Tilman, Belgium*

(Received 8 February 2011; revised manuscript received 4 October 2011; published 30 December 2011)

We have established a link between the global ac response and the local flux distribution of superconducting films by combining magnetic ac susceptibility, dc magnetization, and magneto-optical measurements. The investigated samples are three Nb films: a plain specimen, used as a reference sample, and other two films patterned with square arrays of antidots. At low temperatures and small ac amplitudes of the excitation field, the Meissner screening prevents penetration of flux into the sample. Above a certain ac drive threshold, flux avalanches are triggered during the first cycle of the ac excitation. The subsequent periodic removal, inversion, and rise of flux occurs essentially through the already-created dendrites, giving rise to an ac susceptibility signal weakly dependent on the applied field. The intradendrite flux oscillation is followed, at higher values of the excitation field, by a more drastic process consisting of creation of new dendrites and antidendrites. In this more invasive regime, the ac susceptibility shows a clear field dependence. At higher temperatures a smooth penetration occurs, and the flux profile is characteristic of a critical state. We have also shown that the regime dominated by vortex avalanches can be reliably identified by ac susceptibility measurements.

DOI: 10.1103/PhysRevB.84.214529 PACS number(s): 74.78.Na, 74.78.Fk, 74.25.Dw, 74.25.Op

I. INTRODUCTION

Superconductivity is a state of matter characterized by a diamagnetic response caused by the exclusion of magnetic flux from its interior. In type II superconductors, the resulting field-dependent magnetic moment can be linked to the internal distribution of the quantum units of flux, so-called vortices. Indeed, a picture of the flux distribution at microscopic scales can be indirectly achieved from integrated response techniques, via the assumption of certain predetermined models. Arguably, the most successful and popular mapping between the microscopic and macroscopic superconducting worlds is the Bean critical state model.[1,2] This model allows one to estimate, from magnetization and susceptibility measurements, the maximum current a superconductor can bear before dissipating, i.e., its critical current. The basic assumptions validating the Bean model are the existence of a continuous flux distribution throughout the specimen and a field-independent critical current. Clearly, such restrictive conditions do not account for all possible scenarios of flux distribution. Attempts for adjusting to more realistic situations included the decrement of critical current with magnetic field,[3] the presence of edge barriers,[4,5] and the existence of a finite lower critical field.[6,7] In most cases, these improvements result in marginal corrections to the simpler Bean approximation.

A situation in which the Bean critical state model fails dramatically occurs when sudden flux bursts develop as a consequence of a thermomagnetic instability.[8] Under these circumstances, any estimation of the critical current based on global response techniques is futile and local magnetic probes become imperative. An unambiguous identification of the field range dominated by avalanches can be obtained through the field dependence of the magnetization, which exhibits clear jumps within the instability region.[9–11] However, signatures of the avalanche regime in the ac susceptibility are not easy to recognize, most specially for values of the ac drive h sufficiently small to avoid disturbance on the flux distribution which one intends to probe. For larger values of h, however, both components of the ac susceptibility, $\chi = \chi' + j\chi''$, are reentrant in temperature and applied field; i.e., shielding becomes stronger and dissipation decreases upon increase of either of those two variables. This reentrant behavior has also been observed earlier in Pb films[12,13] and ascribed to the occurrence of flux avalanches. The present work reveals the cause for such change of the diamagnetic response through investigations of the early stages of flux penetration in Nb films. In our approach we performed magnetic measurements employing global techniques—namely, susceptibility and magnetization—as well as magneto-optical imaging (MOI). Our experiments revealed that the first avalanches, while serving as a track for flux entrance, do also guide flux exit, thus suggesting why the initial ac response of the superconducting film is nearly constant for variations of the applied field H or temperature T. Upon increase on H or T, the ac response reenters, i.e., becomes more diamagnetic as the avalanches cease.

II. SAMPLES AND EXPERIMENTAL TECHNIQUES

The samples investigated consist of Nb films of approximately rectangular shape, with thickness $d = 50$ nm. Their lateral dimensions appear in Table I. Two of them have a square array of antidots (ADs) fabricated by electron-beam lithography. The Nb was deposited via dc sputtering on top

TABLE I. Superconducting critical temperature T_c, coherence length $\xi_{GL}(0)$, penetration depth $\lambda_{GL}(0)$, and lateral dimensions l and w for the three samples investigated.

Sample	T_c (K)	$\xi_{GL}(0)$ (nm)	$\lambda_{GL}(0)$ (nm)	l (mm)	w (mm)
Pristine	7.91	9.4	168.0	3.0	2.5
AD04	7.40	9.1	170.0	2.7	2.6
AD08	6.42	9.1	173.0	2.7	2.5

of a SiO_2 insulating substrate. Our preliminary investigations included a variety of similar samples, all of them leading to comparable results. The present report, however, is restricted to results on only three samples, one of each type. Thus, the sample investigated through magnetic measurements is the very same which was imaged using the MO technique. The patterned samples—named AD04 and AD08—have antidots with sizes 0.4 μm and 0.8 μm, respectively. The third specimen—the reference sample—is a plain film of Nb. The period of the patterns is $a = 1.5$ μm, which corresponds to a commensurability field $H_1 = \frac{\Phi_0}{a^2} = 9.2$ Oe at which the densities of vortices and antidots match each other.[14] Using the expression for the upper critical field and for the dirty limit,[15] the zero-temperature superconducting coherence length, $\xi_{GL}(0)$, and the penetration depth, $\lambda_{GL}(0)$, were estimated. The obtained values are shown in Table I, as well as the superconducting transition temperature at zero field, T_c. Noticeably, a drop in T_c results from the insertion of antidots.

Measurements were made for temperatures ranging from 2 K up to T_c, and the ac sinusoidal drive was simulated, in MOI experiments, by cycling the dc field in complete loops made up of 0.1 Oe steps. Ac susceptibility and dc magnetization measurements were carried out with commercial Quantum Design equipment (MPMS and PPMS). The susceptibility measurements were recorded using a fixed frequency of 1 kHz, for values of the excitation field within the ±15 Oe interval. Prior to fixing the value of the excitation frequency, we verified that the susceptibility response is independent of frequency within 5 orders of magnitude, up to values above 1 kHz. In all cases, the excitation field h and the external magnetic field H were applied perpendicular to the film plane. The magneto-optical imaging technique employed relies on the occurrence of the Faraday effect[16] on a magnetic indicator film placed on top of the superconducting specimen. The indicators used in the present work are Bi-substituted yttrium iron garnet films (Bi:YIG) with in-plane magnetization. Data for the so-called Cole-Cole plots of the susceptibility, i.e., its imaginary part χ'' as a function of the real part χ', were taken isothermally, varying the ac drive. Data normalization of the susceptibility was performed using the reference value χ_0 of its real component, which represents the Meissner plateau, measured in the PPMS at $T = 2$ K with a drive amplitude $h = 20$ mOe, in the absence of magnetic field.[17]

III. RESULTS AND DISCUSSION

It is well known that thin films of most superconducting materials exhibit flux avalanches within specific intervals of temperature and applied field.[9–11,18–25] Such behavior is intimately correlated to thermomagnetic instabilities experienced by the material when heat generated by a sudden displacement of vortices cannot be dissipated, creating thus an increase in the local temperature. This warmer region, in turn, has its pinning capability reduced, being thus likely to host even more vortex motion, reinforcing the process.[26,27] There is a threshold temperature T_{th} above which no avalanches occur and a rather smooth penetration of the magnetic flux is observed. It has been shown that T_{th} can be substantially increased if antidots are introduced into the specimen.[9,12,13,28,29] In this case, the most relevant difference, compared to plain films, is that vortices are guided preferentially along the rows of ADs.[13,29] This aspect will be further discussed later in this paper. Above T_{th}, flux invades the sample gradually, and the system appears to obey a critical-state regime. Assuming the simplest of such critical-state regimes, i.e., the Bean model, one can obtain the superconducting critical current density J_c by measuring the field h at which the magnetic flux front reaches a characteristic geometry-dependent penetration distance.[30,31] If one considers a thin disk of thickness d and diameter $2R \gg d$, the two-dimensional effective penetration depth in the perpendicular geometry is $\Lambda = \frac{2\lambda^2}{d}$. For $\Lambda \ll 2R$, the field amplitude at which χ'' peaks, h_p, corresponds to 72% of the full penetration field and can be related to the critical current density by the expression $J_c = \frac{1.03h_p}{d}$.[32] On the other hand, an approximate expression for J_c has been recently developed by Chen and co-authors[33] for films of rectangular shape. We have employed Eq. (20) of Ref. 33 to calculate J_c of our rectangular samples:

$$J_c = \frac{4.85\Upsilon_0(\gamma)}{(3-\gamma^{-1})w} h_p, \tag{1}$$

where $\gamma = l/w$, $\tau = d/w$, and

$$\Upsilon_0(\gamma) = \frac{\arctan(1 - 0.7223\gamma^{-0.954} + 0.3522\gamma^{-2.57} - 0.141\gamma^{-3.66})}{\tau}. \tag{2}$$

Figure 1 compiles results obtained from isothermal ac susceptibility measurements on the three films, taken with the PPMS in zero applied field,[17] using the excitation amplitude $h \leqslant 15$ Oe as the external variable. Panel (a) shows $J_c(\frac{T}{T_c})$ obtained as discussed in the previous paragraph, with h_p determined from the peak in $\chi''(h)$ curves. We have used the reduced variable $t = \frac{T}{T_c}$ to unify the superconducting domain of all studied samples. Curves for the plain film and sample AD04 have two distinct regions: At higher temperatures, $J_c(T)$ is smooth, with upward curvature; below

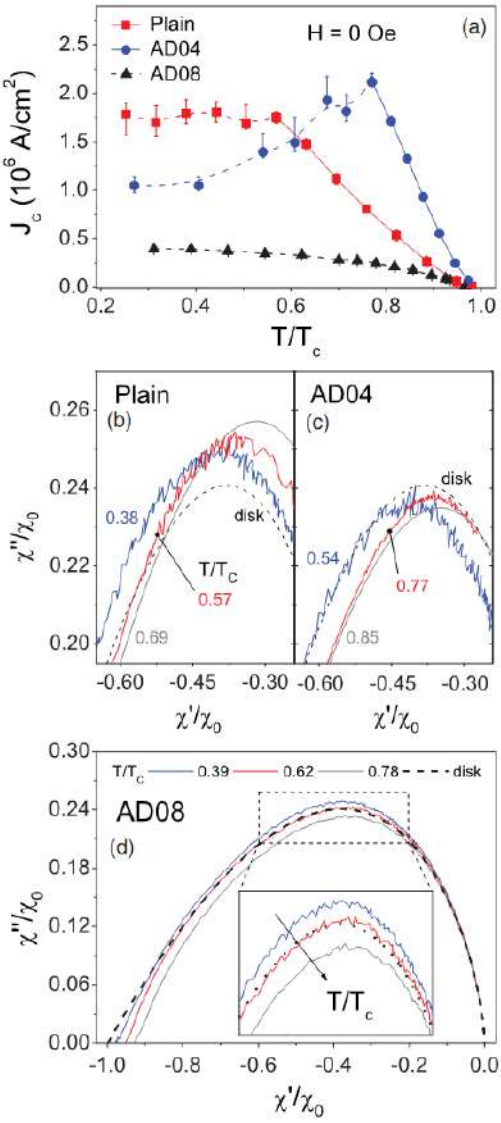

FIG. 1. (Color online) Panel (a): Temperature dependence of the critical current in the absence of a dc field (see main text and Ref. 17), as determined from the peak on the imaginary part of the susceptibility measured as a function of the excitation amplitude. Panels (b)–(d): Cole-Cole plots, at different temperatures, for the studied samples: pristine (b), AD04 (c), and AD08 (d). The theoretical plot for a thin circular disk is also shown. Smoothness or noisiness of the Cole-Cole plots emphasizes different regimes (critical state or avalanches) of flux penetration.

a certain limiting temperature, however, it deviates from this canonical behavior, a change that is intimately connected to the appearance of avalanches in both specimens, as explained later in this paper. The equivalent curve for sample AD08 is quite different: A downward curvature is maintained throughout the whole interval, as a consequence of avalanches being present within the entire temperature domain. As a matter of fact, values of J_c shown for temperatures below the avalanche threshold should not be interpreted as representative of the critical current density, since they were obtained under the erroneous assumption that the system is in a critical-state regime. In the avalanche regime, the actual critical current is a local, extremely inhomogeneous variable, which cannot be properly described by a unique global value. Nonetheless, displaying all points in a single picture stresses the idea that a frontier between both regimes can be reliably obtained from ac susceptibility measurements. It should be noticed that the curves in Fig. 1(a) confirm that the inclusion of ADs of moderate size promotes an increase in J_c[34] and T_{th}.[9,13] Comparing the high-T portions of $J_c(T)$ for the plain film and sample AD04, one clearly sees this improvement, as well as the relative enlargement of the area where avalanches occur. For sample AD08, however, this comparison does not apply, since avalanches take place in the whole temperature window.

A second important signature of the occurrence of avalanches that can be drawn from susceptibility measurements is depicted in panels (b) through (d) of Fig. 1, which show Cole-Cole plots of the susceptibility. Displaying data in such a manner can be quite advantageous to emphasize the occurrence of different regimes of vortex matter. For example, all Cole-Cole plots for a system obeying a critical state dynamics should collapse into one single universal plot, irrespective of the values of applied field, temperature, frequency, and amplitude of the ac drive. Panel (b) shows results around the peak for the pristine film, taken at three different values of T: For temperatures below the threshold limit for avalanches ($t = 0.38$ and 0.57), $\chi''(\chi')$ is very noisy, contrasting with the behavior observed at higher temperatures ($t = 0.69$), for which the curves are noticeably smooth. A similar set of curves is shown in panel (c) for sample AD04, which exhibits avalanches for $t = 0.54$ and $t = 0.77$, but not for $t = 0.85$. Complete Cole-Cole plots for sample AD08 are shown in panel (d) for $t = 0.39$, $t = 0.62$, and $t = 0.78$. The inset features the central portion of the curves, emphasizing the noisy behavior which, for this sample, is present over the entire range of temperatures. It should be noticed that, at the left lower part of Fig. 1(d), χ'' goes to zero while χ' is not -1 for larger values of T. The reason for this behavior is that the initial screening on curves $\chi'(h)$ remains flat but imperfect, while there is essentially no dissipation [$\chi''(h) \sim 0$]. This means that some flux enters but remains pinned. Since this behavior is also exhibited by sample AD08 and the pristine film, one is led to associate it with the intrinsic pinning of Nb. We will return to this point further ahead.

It is also worth comparing the experimental results with those expected theoretically. Chen *et al.*[33] have shown that the ac susceptibility of rectangular films can be adequately treated using the same expression derived by Clem and Sanchez for an infinitely thin circular disk.[32] This result, also included in all Cole-Cole plots of Fig. 1, indicates that, at all temperatures, the plain-film response [panel (b)] is different from that obtained for the Bean approximation, a result that is possibly due to the fact that J_c is not field independent, as assumed in that simple model. As a matter of fact, the Bean model predicts a peak at $\chi'_{max} = 0.38$, whereas the assumption of a field dependence on J_c shifts the peak to the right and up,[35] just as observed for the pristine film. On the other hand, the Cole-Cole plots for the

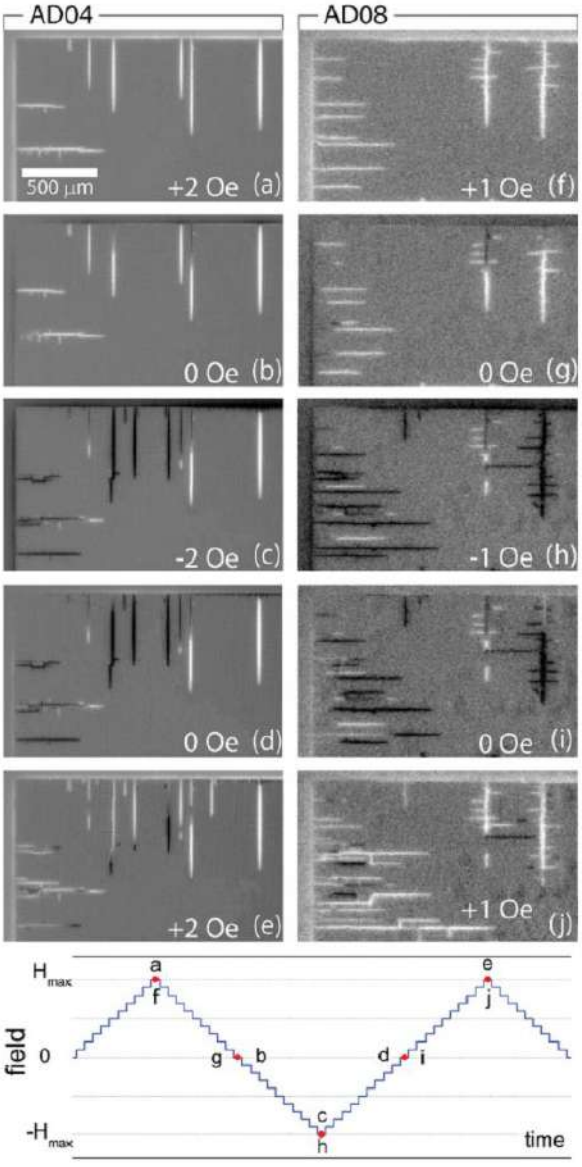

FIG. 2. (Color online) MO images taken at 3 K. White indicates positive flux, dark negative, medium gray stands for zero flux (screened). Panels (a) to (e) are for sample AD04: After zero-field cooling, field increased to 2 Oe (a), decreased to zero (b) and −2 Oe (c), and increased back to zero (d) and 2 Oe (e). Same protocol followed for sample AD08, panels (f) to (j), with field extremes of ±1 Oe. Bottom panel: Sketch of time evolution of the applied field during data collection.

patterned samples deviate from the one predicted by Bean's model in a nonsystematic manner, so that the difference cannot be ascribed to a specific mechanism—e.g., the introduction of creep or of a field-dependent J_c.[35–37]

We turn now the discussion to the images of profiles of flux penetration and exit at relatively small fields. Such images where taken after cyclic field excursions, as in the case

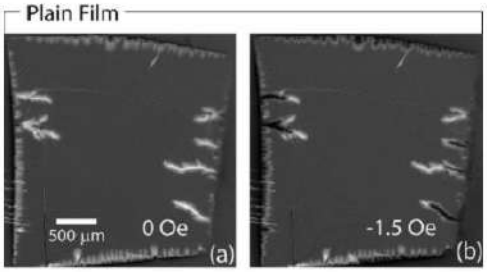

FIG. 3. MO images of the pristine film, taken at 3 K, following the same protocol depicted in Fig. 2: After zero-field cooling, field was cycled between ±4 Oe. Panel (a) was taken at 0 Oe after the first half cycle of the field; panel (b) is for −1.5 Oe.

of those performed during susceptibility measurements. To emulate the magnetic history imprinted by the ac excitation, the external field was ramped up and down in steps of 0.1 Oe. However, given the time needed to acquire images, on the order of 100 ms, the cycles were not sinusoidal, but steplike, as roughly indicated at the bottom of Fig. 2. The similarity among this procedure and that taking place during a sinusoidal cycle in a susceptibility measurement is ensured by the frequency independence of the ac measurements. Figures 2 and 3 present some selected MO images for the three samples studied here. All pictures were taken for $T = 3$ K. White regions correspond to positive penetrated flux, dark areas represent negative flux (antiflux), while medium gray stands for unpenetrated portions of the sample (zero flux). Panels (a) to (e) in Fig. 2 are for sample AD04: After a zero-field cooling procedure, the field was increased to 2 Oe (a), decreased back to zero (b) and to −2 Oe (c), and then increased again to zero (d) and finally to 2 Oe (e). All steps were performed with the ramp rate of 20 Oe/s. We find that near 1.4 Oe, abrupt avalanches suddenly invade the sample from the edge, in the form of finger-type dendrites, clearly guided by the rows of ADs (a). Upon decrease of the field, reversed flux penetrates the sample through the same tracks [(b) and (c)], transforming them progressively into antidendrites. When the field is increased again [(d) and (e)], the tracks are penetrated once more by positive flux, so that the original dendrites are gradually restored. The same behavior is seen in panels (f) to (j) for sample AD08, for which the field protocol is just the same as for AD04, with field extremes of ±1 Oe. This feature is also presented by the pristine sample, as exemplified in panels (a) and (b) of Fig. 3, taken respectively at fields zero and −1.5 Oe, after a field excursion to 4 Oe.

It is worth mentioning that all samples studied here exhibit dendritic penetration at certain values of field and temperature. However, for experiments repeated under the same conditions, flux dendrites follow different tracks during each run. This further emphasizes that the onset of flux avalanches is governed by an instability condition. The lattice of antidots is nevertheless causing some degree of guidance for the full avalanche, in contrast to the dendritic penetration in unpatterned samples.

We have also used magnetic measurements and MO imaging to investigate the reentrant behavior of susceptibility curves. The inset of Fig. 4(a) shows the temperature

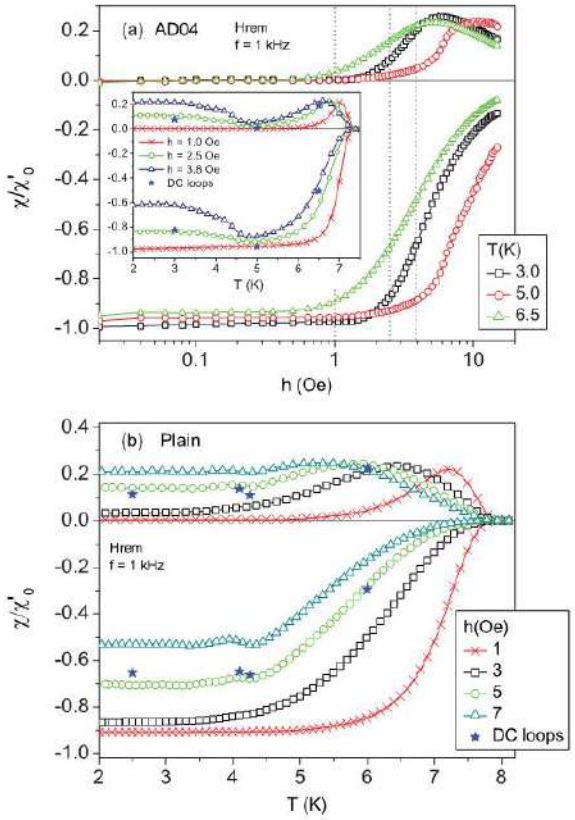

FIG. 4. (Color online) (a): Real and imaginary parts of χ as a function of the ac amplitude, taken at $T = 3$, 5, and 6.5 K. The inset shows the temperature dependence of the same quantities, measured with $h = 1$, 2.5, and 3.8 Oe. Stars represent values of both components, at 3, 5, and 6.5 K, calculated from magnetization loops (see text). (b): Similar to inset in (a) for the pristine film.

dependence of χ' and χ'', measured with ac amplitudes of 1.0, 2.5, and 3.8 Oe, for sample AD04. For the lower value of h, one sees the ordinary ac response of a superconductor; at larger amplitudes, however, the reentrant behavior appears, as already seen earlier in Pb films:[12] Upon increase of the temperature, the real part first decreases, to a more diamagnetic level, and then increases toward zero at the transition. The imaginary part is also odd, starting at a relevant dissipation level and then decreasing before peaking as the transition is approached. One can also follow the evolution of both susceptibility components with the excitation field at fixed temperatures. The main graph of Fig. 4(a) shows isothermal measurements at 3, 5, and 6.5 K. It is rather intriguing that the loss of diamagnetism starts earlier for 3 K than for 5 K, a feature that is also matched by the peaks on χ''. Further increasing T, however, restores the ordinary behavior; i.e., the transition is broadened and starts at lower amplitudes h. The vertical dashed lines on the main panel are guiding lines to connect both experiments: For $h = 1$ Oe, the real part χ' increases monotonically as the temperature changes from 3 to 5, and then to 6.5 K. The imaginary part is also monotonous: negligible for 3 and 5 K, and nonzero at 6.5 K. On the other hand, for $h = 2.5$ Oe both components have an initial decrease as T is switched from 3 to 5 K, followed by an increase, for T growing from 5 to 6.5 K. This feature is even more pronounced at large h. One can also notice that, for small values of h, $\chi'(h) \sim -1$ at low temperatures (e.g., 3 K), but is less negative for larger values of T, whereas the corresponding $\chi''(h) \sim 0$ in all temperatures. As discussed earlier, this is due to efficient pinning: Flux enters the sample but is prevented from moving. For this reason, the left-lower parts of the Cole-Cole plots for all samples studied here do not collapse, as seen, for example, in Fig. 1(d) for sample AD08. This reentrant behavior, discussed here for sample AD04, is also presented by the pristine film, as illustrated in Fig. 4(b) for the temperature dependence of χ' and χ'' for a variety of values of the excitation amplitude. However, as sample AD08 exhibits avalanches in the whole temperature interval, there is no transition between different dynamic regimes, and therefore no reentrance could occur, as is actually the case.

Invoking frequency independence of the susceptibility, one can emulate an ac measurement by cycling the dc field and capturing images of the penetration profile of the sample at adequate values of H. Panels (a)–(c) on Fig. 5 show hysteresis loops for sample AD04 at temperatures 3 K, 5 K, and 6.5 K, respectively. At 3 K one sees a hysteretic loop whose nonvanishing area is due to the viscous motion of entering and exiting vortices within the AD-guided dendrites [panel (d)]. As shown on panel (c), at 6.5 K the loop is wide open, as could be expected for temperatures approaching T_c. The corresponding image is shown on panel (f), with a critical-state-like envelope and a certain "microtexture." Flux entrance is not abrupt, as in an avalanche, exhibiting a filamentary though smooth penetration. Mostly interesting, however, is the fact that the magnetic response at 5 K is nonhysteretic,[38] which means

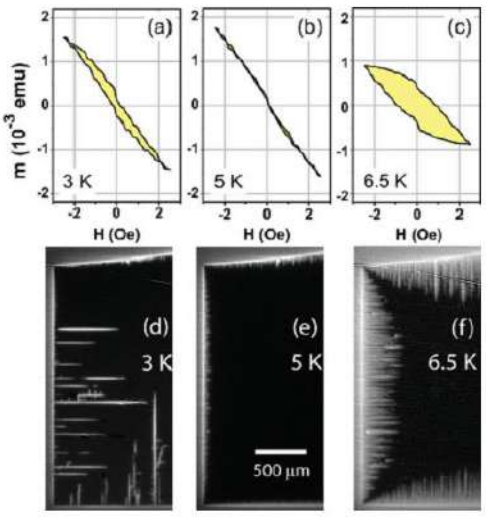

FIG. 5. (Color online) Panels (a)–(c): Hysteresis loops for sample AD04 at temperatures 3, 5, and 6.5 K. The area of the loop, which is nonzero at 3 K, closes down at 5 K and reopens at 6.5 K. Panels (d)–(f) are the corresponding images at the maximum field (2.5 Oe), taken immediately after the virgin curve.

that, upon increase of the temperature, the loop first closes down and then opens up again. The MO image, represented on panel (e), shows quite clearly that the heart of the sample is not penetrated by magnetic flux at 5 K and 2.5 Oe. We have also compared hysteresis loops and MO images for the pristine sample, obtaining similar results. The collapse of the loop, however, does not occur for sample AD08 which, as already discussed, always exhibits avalanches. We take this as an additional evidence that the closing down of the loop is a feature intimately related to the suppression of avalanches in samples AD04 and pristine.

One further evidence that ac measurements can be emulated using dc magnetization loops arises from the argument that χ' is the average slope of the magnetization loop (throughout one full cycle), whereas χ'' is related to the energy losses per sample volume per cycle by

$$\chi'' = \frac{\oint M\, dH}{\pi H_m^2} = \frac{A}{\pi H_m^2}, \tag{3}$$

where A is the area of the magnetization hysteresis loop, which extends from $-H_m$ to $+H_m$.[32,39] Employing this reasoning, we calculated both components of χ using data from the dc loops. As an illustration we have included, in the inset of Fig. 4(a), stars representing such results as obtained from the ±2.5 Oe loops measured at 3, 5, and 6.5 K. A similar procedure for the pristine film, taken with $H_m = 5$ Oe, leads to the set of stars on Fig. 4(b). One can thus conclude that the reentrant behavior of χ'—i.e., a reinforced diamagnetism—is related to the temperature limit for the occurrence of avalanches.[10,11]

As a final remark, we comment on the filamentary structure of the penetrated flux on sample AD04 at high temperatures. Panel (f) in Fig. 5 shows this clearly: While the penetration front has the typical format of a critical-state regime, it is in fact an envelope for a filamentary finger-type structure. Noticeably, however, no avalanches take place at that temperature, and the filamentary inner structure develops smoothly. From time to time, the smooth penetration is perturbed by small amounts of flux entering the film. Minor fluctuations seen on $M(H)$ at 6.5 K [Fig. 5(c)] are the corresponding signatures of those tiny perturbations. This interesting feature, which is in straight connection with the existence of the array of ADs, can be compared with another occurrence of a filamentary structure, observed by Welling *et al.* in a YBCO film with an array of ADs.[40] Flux penetration in the form of thin filaments was also observed in YBCO films deposited on vicinal cut substrates.[41–44]

IV. CONCLUSIONS

Combining magneto-optical visualization of penetrated flux with magnetic ac susceptibility and dc magnetization measurements, we have investigated the early stages of flux penetration on Nb films with and without arrays of antidots. Our results show that ac susceptibility measurements can be used to detect vortex avalanches, either constructing $J_c(T)$ curves or monitoring the occurrence of a noisy behavior in Cole-Cole plots. We have also shown that, in the low-field regime, the roots of most dendrites are reused during the process of entrance and exit of flux, although some new dendrites and antidendrites might also be created at different points along the sample edges. From hysteresis loops measured at different temperatures, we were able to calculate both components of the ac susceptibility. MO images taken at several points of those loops enabled us to establish a reliable link among those three experimental techniques and, through this correspondence, visualize the flux distribution throughout the sample after an ac field cycle.

ACKNOWLEDGMENTS

This work was partially supported by the Methusalem Funding of the Flemish Government, the NES-ESF program, the Belgian IAP, the Fund for Scientific Research-Flanders (FWO-Vlaanderen), the UK Engineering and Physical Sciences Research Council, and the Brazilian funding agencies FAPESP and CNPq. A.V.S. is grateful for the support from the FWO-Vlaanderen. T.H.J. acknowledges the financial support of the Norwegian Research Council. W.A.O. thanks the Centre for Advanced Study (Norway) for the hospitality during the last stage of this work.

*Present address: Faculdade de Engenharia, UNESP - Universidade Estadual Paulista, Departamento de Física e Química, 15385-000 Ilha Solteira, SP, Brazil.

[1]C. P. Bean, Phys. Rev. Lett. **8**, 250 (1962).
[2]C. P. Bean, Rev. Mod. Phys. **36**, 31 (1964).
[3]Y. B. Kim, C. F. Hempstead, and A. R. Strnad, Phys. Rev. **129**, 528 (1963).
[4]H. A. Ullmaier, Phys. Status Solidi **17**, 631 (1966).
[5]J. R. Clem, J. Appl. Phys. **50**, 3518 (1979).
[6]M. V. Indenbom, Th. Schuster, H. Kuhn, H. Kronmüller, T. W. Li, and A. A. Menovsky, Phys. Rev. B **51**, 15484 (1995).
[7]A. V. Silhanek, J. Gutierrez, R. B. G. Kramer, G. W. Ataklti, J. Van de Vondel, V. V. Moshchalkov, and A. Sanchez, Phys. Rev. B **83**, 024509 (2011).
[8]D. V. Denisov, D. V. Shantsev, Y. M. Galperin, Eun-Mi Choi, Hyun-Sook Lee, Sung-Ik Lee, A. V. Bobyl, P. E. Goa, A. A. F. Olsen, and T. H. Johansen, Phys. Rev. Lett. **97**, 077002 (2006).
[9]S. Hebert, L. Van Look, L. Weckhuysen, and V. V. Moshchalkov, Phys. Rev. B **67**, 224510 (2003).
[10]F. Colauto, E. M. Choi, J. Y. Lee, S. I. Lee, V. V. Yurchenko, T. H. Johansen, and W. A. Ortiz, Supercond. Sci. Technol. **20**, L48 (2007).
[11]F. Colauto, E. J. Patino, M. G. Blamire, and W. A. Ortiz, Supercond. Sci. Technol. **21**, 045018 (2008).
[12]A. V. Silhanek, S. Raedts, and V. V. Moshchalkov, Phys. Rev. B **70**, 144504 (2004).
[13]M. Menghini, R. J. Wijngaarden, A. V. Silhanek, S. Raedts, and V. V. Moshchalkov, Phys. Rev. B **71**, 104506 (2005).

[14]Matching effects are less pronounced at the temperature interval reported here (i.e., not very close to T_c). The commensurability field, characteristic of the lattice of ADs, is a reference for the window of magnetic fields at which the events treated here take place.
[15]V. V. Schmidt, *The Physics of Superconductors*, edited by P. Muller and A. V. Ustinov (Springer, Berlin, 1997).
[16]L. E. Helseth, R. W. Hansen, E. I. Il'yashenko, M. Baziljevich, and T. H. Johansen, Phys. Rev. B **64**, 174406 (2001).
[17]The level of control of the zero-field condition was different for the 3 experimental setups employed: below 30 mOe at the MPMS, below 250 mOe at the MOI, and around 1 Oe at the PPMS.
[18]P. Leiderer, J. Boneberg, P. Brüll, V. Bujok, and S. Herminghaus, Phys. Rev. Lett. **71**, 2646 (1993).
[19]C. A. Duran, P. L. Gammel, R. E. Miller, and D. J. Bishop, Phys. Rev. B **52**, 75 (1995).
[20]T. H. Johansen, M. Baziljevich, D. V. Shantsev, P. E. Goa, Y. M. Galperin, W. N. Kang, H. J. Kim, E. M. Choi, M.-S. Kim, and S. I. Lee, Europhys. Lett. **59**, 599 (2002).
[21]A. V. Bobyl, D. V. Shantsev, T. H. Johansen, W. N. Kang, H. J. Kim, E. M. Choi, and S. I. Lee, Appl. Phys. Lett. **80**, 4588 (2002).
[22]I. A. Rudnev, S. V. Antonenko, D. V. Shantsev, T. H. Johansen, and A. E. Primenko, Cryogenics **43**, 663 (2003).
[23]S. C. Wimbush, B. Holzapfel, and C. Jooss, J. Appl. Phys. **96**, 3589 (2004).
[24]I. A. Rudnev, D. V. Shantsev, T. H. Johansen, and A. E. Primenko, Appl. Phys. Lett. **87**, 042502 (2005).
[25]D. V. Denisov, A. L. Rakhmanov, D. V. Shantsev, Y. M. Galperin, and T. H. Johansen, Phys. Rev. B **73**, 014512 (2006).
[26]M. Baziljevich, A. V. Bobyl, D. V. Shantsev, E. Altshuler, T. H. Johansen, and S. I. Lee, Physica C **369**, 93 (2002).
[27]F. Colauto, E. Choi, J. Y. Lee, S. I. Lee, E. J. Patino, M. G. Blamire, T. H. Johansen, and W. A. Ortiz, Appl. Phys. Lett. **96**, 092512 (2010).
[28]S. Kolesnik, V. Vlasko-Vlasov, U. Welp, G. W. Crabtree, T. Piotrowski, J. Wrobel, A. Klimov, P. Przystupski, T. Skoskiewicz, and B. Dabrowski, Physica C **341-348**, 1093 (2000).
[29]V. Vlasko-Vlasov, U. Welp, V. Metlushko, and G. W. Crabtree, Physica C **341-348**, 1281 (2000).
[30]E. H. Brandt and M. Indenbom, Phys. Rev. B **48**, 12893 (1993).
[31]E. Zeldov, J. R. Clem, M. McElfresh, and M. Darwin, Phys. Rev. B **49**, 9802 (1994).
[32]J. R. Clem and A. Sanchez, Phys. Rev. B **50**, 9355 (1994).
[33]D.-X. Chen, C. Navau, N. Del-Valle, and A. Sanchez, Physica C **470**, 89 (2010).
[34]V. V. Moshchalkov, M. Baert, V. V. Metlushko, E. Rosseel, M. J. Van Bael, K. Temst, Y. Bruynseraede, and R. Jonckheere, Phys. Rev. B **57**, 3615 (1998).
[35]D. V. Shantsev, Y. M. Galperin, and T. H. Johansen, Phys. Rev. B **61**, 9699 (2000).
[36]E. H. Brandt, Phys. Rev. B **55**, 14513 (1997).
[37]E. H. Brandt, Phys. Rev. B **58**, 6523 (1998).
[38]Notice that the same scale is used for the 3 magnetic loops shown. Further amplification of the 5 K loop would evidence some amount of hysteresis, due to penetration at the borders.
[39]R. B. Goldfarb and A. F. Clark, IEEE Trans. Magnetics, MAG-21, 332 (1985).
[40]M. S. Welling, R. J. Wijngaarden, C. M. Aegerter, R. Wördenweber, and P. Lahl, Physica C **404**, 410 (2004).
[41]Ch. Jooss, R. Warthmann, and H. Kronmüller, Phys. Rev. B **61**, 12433 (2000).
[42]A. Polyanskii, R. L. S. Emergo, J. Z. Wu, T. Aytug, D. K. Christen, G. K. Perkins, and D. Larbalestier, Phys. Rev. B **72**, 174509 (2005).
[43]M. Djupmyr, G. Cristiani, H.-U. Habermeier, and J. Albrecht, Phys. Rev. B **72**, 220507(R) (2005).
[44]V. V. Yurchenko, A. J. Qviller, P. B. Mozhaev, J. E. Mozhaeva, J. B. Hansen, C. S. Jacobsen, I. M. Kotelyanskii, A. V. Pan, and T. H. Johansen, Physica C **470**, 799 (2010).

4. Dinâmica de Vórtices em supercondutores mesoscópicos

Embora os trabalhos apresentados na seção 3 tenham sido parcialmente desenvolvidos quando eu já estava na UNESP, não foi possível dar continuidade em estudos correlatos por conta desse fato. Dessa forma, intensifiquei meus estudos em dinâmica de vórtices usando simulações computacionais as quais resolvem as equações de Ginzburg-Landau dependentes do tempo (TDGL). Esses estudos foram feitos em colaboração com o Prof. Edson Sardella da UNESP de Bauru e, desde então, temos trabalhado junto tanto que fundamos um grupo de pesquisa, o Grupo de Supercondutividade e Materiais Avançados (GSMA). As equações TDGL são expressas na equação (4.1).

$$\frac{\hbar^2}{2m^*D}\left(\frac{\partial}{\partial t}+\frac{ie^*}{\hbar}\varphi\right)\psi=-\frac{1}{2m^*}\left(-i\hbar\boldsymbol{\nabla}-\frac{e^*}{c}\boldsymbol{A}\right)^2\psi+\alpha\psi+\beta|\psi|^2\psi,$$
$$\frac{4\pi}{c}\sigma\left(\frac{1}{c}\frac{\partial \boldsymbol{A}}{\partial t}+\nabla\varphi\right)=\frac{4\pi}{c}\boldsymbol{J_s}-\boldsymbol{\nabla}\,\mathrm{x}\,\boldsymbol{\nabla}\,\mathrm{x}\,\boldsymbol{A}\,, \qquad (4.1)$$

sendo a densidade de supercorrente:

$$\boldsymbol{J_s}=\frac{e^*}{m^*}\mathrm{Re}\left[\bar{\psi}\left(-i\hbar\boldsymbol{\nabla}-\frac{e^*}{c}\boldsymbol{A}\right)\psi\right], \qquad (4.2)$$

onde D é o coeficiente de difusão, σ é a condutividade elétrica, $\boldsymbol{A}$ o potencial vetor, sendo $\boldsymbol{B}=\boldsymbol{\nabla}\,\mathrm{x}\,\boldsymbol{A}$, $\alpha=\alpha(T)=\alpha_0(T-T_c)$ para $T<T_c$ e $\alpha=0$ para $T>T_c$, sendo $\alpha_0>0$ e β uma constante positiva que independe da temperatura.

É conveniente escrevermos as equações TDGL em unidades reduzidas, pois como elas só admitem soluções numéricas, na forma adimensional tem-se um menor número de parâmetros para ser considerado. As unidades que usamos são tais que:

$$\psi=\psi_0\tilde{\psi}\,,$$
$$T=T_c\tilde{T}\,,$$
$$\boldsymbol{\nabla}=\frac{1}{\xi(0)}\tilde{\boldsymbol{\nabla}}\,,$$
$$t=\frac{\xi(0)^2}{D}\tilde{t}\,,$$
$$\boldsymbol{A}=H_{c2}(0)\xi(0)\tilde{\boldsymbol{A}}\,,$$
$$\varphi=\frac{H_{c2}(0)D}{c}\tilde{\varphi}\,,$$
$$\boldsymbol{\nabla}\,\mathrm{x}\,\boldsymbol{\nabla}\,\mathrm{x}\,\boldsymbol{A}=H_{c2}\,\tilde{\boldsymbol{\nabla}}\,\mathrm{x}\,\tilde{\boldsymbol{\nabla}}\,\mathrm{x}\,\tilde{\boldsymbol{A}}\,, \qquad (4.3)$$

onde $H_{c2}(0)=\phi_0/2\pi\xi^2$ é o campo crítico superior dos supercondutores do tipo II e $\phi_0=hc/2e$ o quantum de fluxo magnético.

Substituindo as equações (4.3) nas equações (4.1) e (4.2), obtemos as equações TDGL na forma normalizada, como segue:

$$\left(\frac{\partial}{\partial t}+i\varphi\right)\psi=-(-i\boldsymbol{\nabla}-\boldsymbol{A})^2\psi+(1-T)\psi(1-|\psi|^2), \qquad (4.4)$$
$$\Sigma\left(\frac{\partial \boldsymbol{A}}{\partial t}+\boldsymbol{\nabla}\varphi\right)=\boldsymbol{J_s}-\kappa^2\,\boldsymbol{\nabla}\,\mathrm{x}\,\boldsymbol{\nabla}\,\mathrm{x}\,\boldsymbol{A}\,, \qquad (4.5)$$
$$\boldsymbol{J_s}=(1-T)\,\mathrm{Re}\,[\bar{\psi}(-i\boldsymbol{\nabla}-\boldsymbol{A})\psi]\,, \qquad (4.6)$$

onde os til's das equações foram suprimidos e $\Sigma=4\pi\sigma D\lambda^2(0)/c^2\xi^2(0)$.

As equações TDGL são invariantes de calibre (*gauge invariance*) o que significa que elas descrevem uma simetria global, pois não apresentam variações sob transformações de simetria. Essas transformações são as seguintes:

$$\begin{aligned} \psi &= \psi' e^{-i\chi}, \\ \boldsymbol{A} &= \boldsymbol{A}' - \boldsymbol{\nabla}\chi\,, \\ \varphi &= \varphi' + \frac{\partial \chi}{\partial t}. \end{aligned} \qquad (4.7)$$

Aplicando as transformações descritas em (4.7), as equações TDGL permanecem invariantes com as novas funções. Para exemplificar, vamos tomar a equação (4.5). Para o lado esquerdo da equação, temos que:

$$\Sigma\left(\frac{\partial \boldsymbol{A}}{\partial t} + \boldsymbol{\nabla}\varphi\right) = \beta\frac{\partial}{\partial t}(\boldsymbol{A}' - \boldsymbol{\nabla}\chi) + \beta\boldsymbol{\nabla}\left(\varphi' + \frac{\partial \chi}{\partial t}\right) = \beta\left(\frac{\partial \boldsymbol{A}'}{\partial t} + \boldsymbol{\nabla}\varphi'\right). \quad (4.8)$$

Para a equação da densidade de corrente:

$$\begin{aligned} \boldsymbol{J_s} &= (1-T)\ \mathrm{Re}\,[\psi^*(-i\boldsymbol{\nabla} - \boldsymbol{A})\psi] \\ &= (1-T)\ \mathrm{Re}\, e^{i\chi}\left[\bar{\psi}'\left(-i\boldsymbol{\nabla} - (\boldsymbol{A}' - \boldsymbol{\nabla}\chi)\right)\psi'\right]e^{-i\chi} \\ &= (1-T)\ \mathrm{Re}\, e^{i\chi}\,\bar{\psi}'[-i\boldsymbol{\nabla} - \boldsymbol{A}']\psi' e^{-i\chi} \\ &= (1-T)\ \mathrm{Re}\,[\bar{\psi}'(-i\boldsymbol{\nabla} - \boldsymbol{A}')\psi']\,. \end{aligned} \quad (4.9)$$

Dessa forma $\boldsymbol{J_s}$ também é invariante de calibre. Usando a propriedade de que o rotacional do gradiente é nulo $\boldsymbol{\nabla} \times \boldsymbol{\nabla}\chi = 0$, fazemos a seguinte transformação:

$$\kappa^2\,\boldsymbol{\nabla}\,\mathrm{x}\,\boldsymbol{\nabla}\,\mathrm{x}\,\boldsymbol{A} = \kappa^2\,\boldsymbol{\nabla}\,\mathrm{x}\,\boldsymbol{\nabla}\,\mathrm{x}\,(\boldsymbol{A}' - \boldsymbol{\nabla}\chi) = \kappa^2\,\boldsymbol{\nabla}\,\mathrm{x}\,\boldsymbol{\nabla}\,\mathrm{x}\,\boldsymbol{A}'.$$

Assim, finalizamos a demonstração da invariância de calibre para a equação (4.5).

As equações TDGL não podem ser resolvidas analiticamente. Dessa forma, recorremos à sua solução numérica onde tomamos como base o trabalho de Gropp e colaboradores, publicado em 1996[3]. Este trata da simulação numérica em supercondutores do tipo II através das equações TDGL, utilizando o método de variáveis de ligação (ψ-U). Tal método emprega o uso de um campo auxiliar U, onde cada uma de suas componentes está associada a uma componente do potencial vetor que, em coordenadas cartesianas, fica:

$$U_{x(x,y,z)} = exp\left(-i\kappa\int_{xo}^{x} Ax(\xi,y,z)d\xi\right), \qquad (4.10)$$

$$U_{y(x,y,z)} = exp(-i\kappa\int_{yo}^{y} Ay(x,\eta,z)\,d\eta), \qquad (4.11)$$

$$U_{z(x,y,z)} = exp(-i\kappa\int_{zo}^{z} Az(x,y,\zeta)\,d\zeta). \qquad (4.12)$$

Então reescrevemos cada componente do potencial vetor em termos dos campos auxiliares. Para o caso de amostras em duas dimensões, que é o nosso caso, negligenciamos a componente U_z.

[3] W. D. Gropp et all., J. Comput.Phys. 123, n. 22, p. 254-266 (1996).

Fazendo uma derivada das equações (4.10) e (4.11), expressamos as componentes A_x e A_y do potencial vetor em termos dos campos auxiliares U_x e U_y, respectivamente:

$$A_x = -\frac{1}{i\kappa}\left(U_x^* \frac{\partial U_x}{\partial x}\right), \tag{4.13}$$

$$A_y = -\frac{1}{i\kappa}\left(U_y^* \frac{\partial U_y}{\partial y}\right), \tag{4.14}$$

onde utilizamos as seguintes propriedades do campo auxiliar: a de ser complexo e a de ser uni modular, i.e., ${U_x}^{-1} = {U_x}^*$ e $U_y^* = {U_y}^{-1}$.

$$A_u = -\frac{1}{i\kappa}\left(U_u^* \frac{\partial U_u}{\partial u}\right), \tag{4.15}$$

onde o índice u indica as coordenadas x, y.

Como o campo auxiliar e o parâmetro de ordem estão em função das coordenadas espaciais e do tempo (as quais não estão explícitas), podemos utilizar a regra do produto para escrever a seguinte expressão:

$$\frac{1}{i\kappa}\frac{\partial(U_u\psi)}{\partial u} = \frac{1}{i\kappa}\frac{\partial U_u}{\partial u}\psi + \frac{1}{i\kappa}\frac{\partial \psi}{\partial u}U_u \ , \tag{4.16}$$

comparando (4.16) com (4.15) temos:

$$\frac{1}{i\kappa}\frac{\partial(U_u\psi)}{\partial u} = -A_u U_u\,\psi + \frac{1}{i\kappa}\frac{\partial \psi}{\partial u}U_u \ , \tag{4.17}$$

e utilizando a propriedade $U_u^* = {U_u}^{-1}$, vem:

$$\frac{1}{i\kappa}U_u^*\frac{\partial(U_u\psi)}{\partial u} = \frac{1}{i\kappa}\frac{\partial \psi}{\partial u} - A_u\,\psi \ . \tag{4.18}$$

Substituindo (4.18) em (4.4) e (4.6), reescrevemos as equações da TDGL em termos do campo auxiliar.

$$\frac{\partial \psi}{\partial t} = \frac{1}{\kappa^2}\sum_{u=x,y} {U_u}^* \frac{\partial^2(U_u\psi)}{\partial u^2} - \psi + |\psi^2|\psi, \tag{4.19}$$

$$\beta\left(\frac{\partial \boldsymbol{A}}{\partial t}\right) + \nabla \times \boldsymbol{B} = \boldsymbol{J}_{su} = \frac{1}{2i\kappa}\left[\left(U_u^*\psi^*\frac{\partial(U_u\psi)}{\partial u}\right) - \left(U_u\psi\frac{\partial(U_u^*\psi^*)}{\partial u}\right)\right]. \tag{4.20}$$

Esse método tem a importante característica de preservar a invariância de calibre das equações TDGL. Agora iremos modelar o sistema que será constituído de uma malha supercondutora. Para isso, suporemos uma amostra isotrópica bidimensional, em que a_x e a_y são as dimensões das células unitárias que compõem a malha. Dessa forma, as regiões de contorno para tais condições estarão em um intervalo dado por:

$$\Omega_{ij} = x_i < x < x_{i+1}\,, y_j < y < y_{j+1} \tag{4.21}$$

No qual

$$x_i = x_1 + (i-1)a_x,$$

$$y_j = y_1 + (j-1)a_y. \tag{4.22}$$

Temos que o tamanho das coordenadas é dado em função do tamanho da célula unitária onde: $i = 1 \ldots n_x + 1$ e $j = 1 \ldots n_y + 1$.

Temos que a região supercondutora $\Omega_{i,j}^{SC}$ está dentro do espaço delimitado por (4.21) entretanto, no perímetro da malha não conseguimos calcular diretamente as grandezas físicas. Estas são obtidas pela estimativa a partir das grandezas físicas que estão dentro de uma região efetiva, como exemplificado na Figura 4.1, cujos intervalos são:

$$\Omega_{sc} i,j = x_1 + \frac{1}{2}a_x < x < x_{n-1} + \frac{1}{2}a_x ,$$

$$y_1 + \frac{1}{2}a_y < y < y_{n-1} + \frac{1}{2}a_y . \quad (4.22)$$

São nestes intervalos de contorno que serão calculadas as grandezas físicas pertinentes do problema. Para fins de discretização, especificaremos quais as variáveis que iremos utilizar e onde as calcularemos na malha. Para cada variável temos o que segue.

Parâmetro de ordem:

$$\psi_{ij}\ i = 1 \ldots N_x + 1;\ j = 1 \ldots N_y + 1, \quad (4.23)$$

Variável de ligação:

$$U_{x,ij} = U_x(x_{i+1}, y_j)U_x^*(x_i, y_j),$$

$$U_{y,ij} = U_y(x_i, y_{j+1})U_y^*(x_i, y_j) , \quad (4.24)$$

onde:

$$U_{x,ij} = \exp\left(-i\kappa \int_{xi}^{xi+1} A_x(\xi, y, z)d\xi\right),$$

$$U_{y,ij} = \exp\left(-i\kappa \int_{yj}^{yj+1} A_y(x, \eta, z)d\eta\right). \quad (4.25)$$

O potencial vetor e a respectiva localização dos componentes deste são:

$$A_{xij} = A_x\left(x_i + \tfrac{1}{2}a_x , y_j\right), i = 1 \ldots N_x; j = 1 \ldots N_y + 1 ,$$

$$A_{yij} = A_y\left(x_i , y_j + \tfrac{1}{2}a_y\right), i = 1 \ldots N_x + 1; j = 1 \ldots N_y. \quad (4.26)$$

O campo de indução magnética:

$$B_{zij} = B_z(x_i + \tfrac{1}{2}a_x , y_j + \tfrac{1}{2}a_y)\ i = 1 \ldots N_x; j = 1 \ldots N_y . \quad (4.27)$$

A densidade de supercorrente J_s:

$$J_{sxij} = J_{sx}\left(x_i + \tfrac{1}{2}a_x , y_j\right) \quad i = 1 \ldots N_x; j = 1 \ldots N_y + 1,$$

$$J_{syij} = J_{sy}\left(x_i , y_j + \tfrac{1}{2}a_y\right) \quad i = 1 \ldots N_x + 1; j = 1 \ldots N_y. \quad (4.28)$$

A Figura 4.1 mostra a malha de discretização e os pontos onde são calculadas as grandezas físicas referentes às equações de (4.25) a (4.29). Onde N_x, N_y determinam o número total de células unitárias em cada direção por toda a amostra, a_x e a_y são as dimensões da célula unitária.

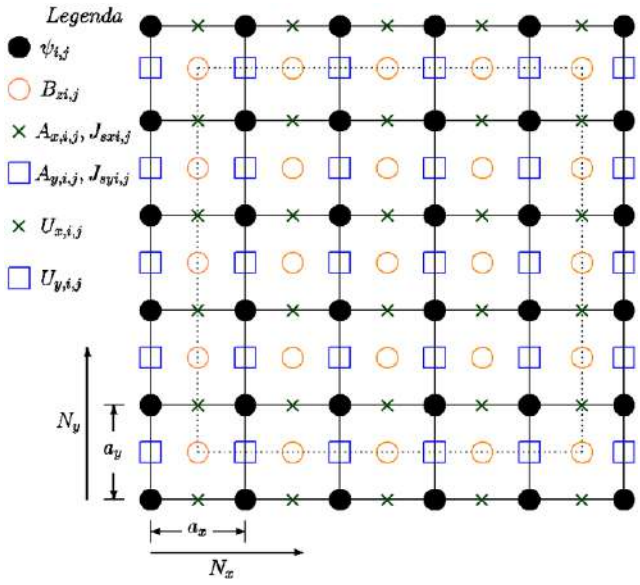

Figura 4.1: Malha supercondutora bidimensional. A legenda mostra onde cada quantidade é calculada na malha.

Generalizando (4.26) em termos de u, temos que seus limites de integração correspondem às dimensões de uma célula unitária, assim:

$$U_{uij} = \exp(-i\kappa a_u A_{uij}).$$

Logo,

$$A_{uij} = \frac{1}{-i\kappa a_u} \ln U_{uij}. \tag{4.30}$$

Para expressarmos B_z em termos dos campos auxiliares, faremos algumas transformações. Utilizando o teorema de Stokes temos que:

$$\exp\left(-i\kappa \int_s B_z \, dx\, dy\right) = \exp(-i\kappa \oint \boldsymbol{A} \,.\, d\boldsymbol{l}). \tag{4.31}$$

Expandindo (4.31) em séries de Taylor até o segundo termo, obtemos uma função linear então:

$$\exp\left(-i\kappa \int_s B_z \, dx\, dy\right) = 1 - i\kappa B_{zij} a_x a_y, \tag{4.32}$$

sendo a integral de superfície $a_x a_y$ correspondente à área de uma célula unitária.

A integral de linha da equação (4.31) e a equação (4.30) nos permitem calcular o valor de B_{zij} para cada célula unitária utilizando as variáveis de ligação em x e y no contorno da célula unitária, como mostra a Figura 4.1. Dessa forma, temos dois campos auxiliares em x e y:

$$\exp(-i\kappa \oint_{cel} \boldsymbol{A} \,.\, d\boldsymbol{l}) = U^*_{x;ij+1} U^*_{y;ij} U_{x;ij} U_{y;i+1j} = W_{zij}, \tag{4.33}$$

onde utilizamos o termo abreviativo W_{zij}. Comparando (4.33) com (4.32) temos:

$$B_{zij} = \frac{1-U^*_{x;ij+1}U^*_{y;ij}U_{x;ij}U_{y;i+1j}}{i\kappa a_x a_y} = \frac{1-W_{zij}}{i\kappa a_x a_y}. \quad (4.34)$$

A discretização da componente x da densidade de corrente (4.23), em termos das variáveis discretas, de acordo com (4.29), fica:

$$J_{sxij} = \frac{1}{2i\kappa}\left[(U_x^*\psi^*)\left(x_i + \tfrac{1}{2}a_x, y_j\right)\left(\frac{\partial U_x\psi}{\partial x}\right)\left(x_i + \tfrac{1}{2}a_x, y_j\right)\right],$$

$$-\left[U_x\psi\left(x_i + \tfrac{1}{2}a_x, y_j\right)\left(\frac{\partial U_x^*\psi^*}{\partial x}\right)\left(x_i + \tfrac{1}{2}a_x, y_j\right)\right]. \quad (4.35)$$

Primeiramente, vamos aproximar $\left(x_i + \frac{1}{2}a_x, y_j\right)$ pelo valor médio de (x_i, y_j) e (x_{i+1}, y_j) que é o próximo ponto onde é efetuado o cálculo em relação a um ponto de referência. Assim temos que:

$$U_x\psi\left(x_i + \tfrac{1}{2}a_x, y_j\right) = \tfrac{1}{2}(U_{xij}\psi_{i+1j} + \psi_{ij}). \quad (4.36)$$

Para o termo diferencial, vamos utilizar a definição de derivada aplicada aos pontos (x_i, y_j) e (x_{i+1}, y_j) fazendo uma aproximação para a dimensão da componente x da célula unitária, assim:

$$\frac{\partial U_x\psi}{\partial x}\left(x_i + \tfrac{1}{2}a_x, y_j\right) = \frac{U_{xij}\psi_{i+1j} - \psi_{ij}}{a_x}. \quad (4.37)$$

Substituindo (4.27) e (4.36) em (4.35) temos:

$$J_{sxij} = \frac{1}{2i\kappa a_x}\left(U_{xij}\psi^*_{ij}\psi_{i+1j} - U^*_{xij}\psi_{ij}\psi^*_{i+1j}\right). \quad (4.38)$$

Para J_{syij}, temos que:

$$J_{syij} = \frac{1}{2i\kappa}\left(U_y^*\psi^*\right)\left(x_i, y_j + \frac{1}{2}a_y\right)\left(\frac{\partial U_y\psi}{\partial y}\right)\left(x_i, y_j + \frac{1}{2}a_y\right) -$$

$$U_y\psi\left(x_i, y_j + \frac{1}{2}a_y\right)\left(\frac{\partial U_y^*\psi^*}{\partial y}\right)\left(x_i, y_j + \frac{1}{2}a_y\right). \quad (4.39)$$

Utilizando o procedimento análogo ao do cálculo de J_{sxij}, temos:

$$U_y\psi\left(x_i, y_j + \frac{1}{2}a_y\right) = \tfrac{1}{2}\left(U_{yij}\psi_{i,j+1} + \psi_{i,j}\right)$$

e

$$\left(\frac{\partial U_y\psi}{\partial y}\right)\left(x_i, y_j + \frac{1}{2}a_y\right) = \frac{U_{yij}\psi_{i,j+1} - \psi_{i,j}}{a_y} \quad (4.40)$$

Assim, J_{syij} torna-se:

$$J_{syij} = \frac{1}{2i\kappa a_y}\left(U_{yij}\psi^*_{ij}\psi_{ij+1} - U^*_{yij}\psi_{ij}\psi^*_{ij+1}\right) \quad (4.41)$$

As condições de contorno externo da amostra homogênea bidimensional serão descritas na sequência.

Para o campo de indução:

$$B_{z;1,j} = H \; ; \; B_{z;N_x,j} = H \; j = 2 \ldots N_y,$$

$$B_{z;i,1} = H \; ; \; B_{z;i,N_y} = H \; i = 2 \ldots N_x, \tag{4.42}$$

onde H é o campo magnético aplicado, assim, no perímetro da amostra, o campo de indução é igual ao campo aplicado.

O parâmetro de ordem em $i = 1$ e $i = N_{x+1}$ temos:

$$\psi_{1,j} = U_{x;1,j}\psi_{2,j} \qquad j = 2 \ldots N_y \rightarrow \text{borda esquerda (oeste da amostra)},$$

$$\psi_{N_x+1,j} = U^*_{x;N_x-1,j}\psi_{N_x,j} \quad j = 2 \ldots N_y \rightarrow \text{borda direita (leste da amostra)}.$$

(4.43)

O parâmetro de ordem em $j = 1$ e $j = N_{y+1}$ temos:

$$\psi_{i,1} = U_{y;i,1}\psi_{i,2} \qquad i = 2 \ldots N_x \rightarrow \text{borda de cima (norte da amostra)},$$

$$\psi_{i,N_y+1} = U^*_{y;i,N_y-1}\psi_{i,N_y} \; i = 2 \ldots N_x \rightarrow \text{borda de baixo (sul da amostra)}.$$

(4.44)

As condições de contorno do parâmetro de ordem apresentadas em (4.43) e (4.44) não incluem os "cantos" da amostra, como mostra a Figura 4.1. Para tais fins, iremos calculá-las utilizando uma média dos valores de seus pontos vizinhos. Então, para os quatro cantos temos:

$$\psi_{1,1} = \frac{1}{2}\left(\psi_{2,1} + \psi_{1,2}\right),$$

$$\psi_{1,Ny+1} = \frac{1}{2}\left(\psi_{2,Ny+1} + \psi_{1,Ny-1}\right),$$

$$\psi_{Nx+1,1} = \frac{1}{2}\left(\psi_{Nx-1,1} + \psi_{Nx+1,2}\right),$$

$$\psi_{Nx+1,Ny+1} = \frac{1}{2}\left(\psi_{Nx-1,Ny+1} + \psi_{Nx+1,Ny-1}\right). \tag{4.45}$$

O cálculo do campo auxiliar no perímetro da amostra é obtido através de seus pontos vizinhos de acordo com a equação (4.33), assim, temos para U_x e U_y respectivamente:

$$U_{x;i,1} = U_{x;i,2}U^*_{y;i+1,1}U_{y;i,j}\exp(-i\kappa \oint \boldsymbol{A}\,.\,d\boldsymbol{l}) \; ; i = 2 \ldots Nx - 1,$$

$$U_{x;i,Ny+1} = U_{xi,Ny-1}U^*_{y;i,Ny}U_{y;i+1,Ny}conj[\exp(-i\kappa \oint \boldsymbol{A}\,.\,d\boldsymbol{l})] \; ; i = 2 \ldots Nx - 1,$$

$$U_{y;1,j} = U^*_{x;1,j+1}U_{x;1,j}U_{y;2,j}conj[\exp(-i\kappa \oint \boldsymbol{A}\,.\,d\boldsymbol{l})] \; ; j = 1 \ldots Ny,$$

$$U_{y;Nx+1,j} = U_{x;Nx,j+1}U^*_{x;Nx,j}U_{y;Nx-1,j}\exp(-i\kappa \oint \boldsymbol{A}\,.\,d\boldsymbol{l}) \; ; j = 1 \ldots Ny, \tag{4.46}$$

onde o termo $conj$ significa que estamos fazendo o conjugado da função complexa entre colchetes.

Entretanto, o conjunto de equações (4.46) não levam em conta os cantos do campo auxiliar que é obtido de maneira análoga, porém, os termos denotados com V estão atrasados em um passo de tempo em relação aos termos com U nesta nossa aproximação, assim:

$$U_{x;1,1} = U_{x;1,2}U^*_{y;2,1}V_{y;1,1}\exp(-i\kappa \oint \boldsymbol{A}.d\boldsymbol{l})$$

$$U_{x;1,Ny+1} = U_{x;1,Ny}V^*_{y;1,Ny}U_{y;2,Ny}conj[\exp(-i\kappa \oint \boldsymbol{A}.d\boldsymbol{l})]$$

$$U_{x;Nx,Ny+1} = U_{x;Nx,Ny}U^*_{y;Nx,Ny}V_{y;Nx+1,Ny}conj[\exp(-i\kappa \oint \boldsymbol{A}.d\boldsymbol{l})]$$

$$U_{x;Nx,1} = U_{x;Nx,2}V^*_{y;Nx+1,1}U_{y;Nx,1}\exp(-i\kappa \oint \boldsymbol{A}.d\boldsymbol{l}) \qquad (4.47)$$

Dessa forma, temos as condições de contorno apresentadas pela equação (4.21), as quais determinam o perímetro da amostra.

Por fim, faremos a discretização referente às equações (4.19) e (4.20). De acordo com as condições de contorno da equação (4.23), vamos fazer a discretização, primeiramente, para cada célula unitária e, em seguida, para toda a malha. Assim, temos:

$$\int_{y_j+1/2a_y}^{y_j+1/2a_y}\int_{x_i-1/2a_x}^{x_i+1/2a_x}(\psi - |\psi^2|\psi) \rightarrow (\psi_{ij} - |\psi_{ij}^2|\psi_{ij}) \text{ para célula unitária} \qquad (4.48)$$

em toda malha o termo referente ao condensado fica:

$$\sum_{j=2}^{N_y}\sum_{i=2}^{N_x}(\psi_{ij} - |\psi_{ij}^2|\psi_{ij}) \qquad (4.49)$$

Para o termo da energia cinética, primeiramente vamos fazer uma aproximação da derivada parcial utilizando o método das diferenças finitas onde a série de Taylor será truncada na derivada de segunda ordem, pois corresponde ao operador da energia cinética. Então temos:

$$f(x) - f(a) = \frac{\partial^2(U_x\psi)}{\partial x^2}\frac{(x-a)^2}{2!} \qquad (4.50)$$

como $f(x) = (U_x\psi_{i+1j})$, $f(a) = \psi_{ij}$ e $x - a = a_x$ para a célula unitária, substituindo-as em (4.50), temos:

$$\frac{\partial^2(U_x\psi)}{\partial x^2} = \frac{(U_{x;i+1j}\psi_{i+1j} - 2\psi_{ij} - U_{x;i-1j}\psi_{i-1j})}{(a_x)^2} \qquad (4.51)$$

o termo $2!\,(U_x\psi_{i+1j} - \psi_{ij}) = (U_{x;i+1j}\psi_{i+1j} - 2\psi_{ij} - U_{x;i-1j}\psi_{i-1j})$ pois, no caso dessa aproximação de segunda ordem, pegamos dois pontos vizinhos para um dado valor de i, tendo como referência um certo U_{xij} e ψ_{ij}.

Vamos expressar genericamente (4.51) e, em toda malha, o termo da energia cinética fica:

$$\int_{\Omega_{sc}}\frac{\partial^2(U_u\psi)}{\partial u^2} = \sum_{j=2}^{N_y}\sum_{i=2}^{N_x}\frac{(U_{x;i+1j}\psi_{i+1j} - 2\psi_{ij} - U_{x;i-1j}\psi_{i-1j})}{(a_x)^2} + \frac{(U_{y;ij+1}\psi_{ij+1} - 2\psi_{ij} - U_{y;ij-1}\psi_{ij-1})}{(a_y)^2} \qquad (4.52)$$

substituindo (4.52) em (4.19) e utilizando a equação (4.25) obtemos:

$$\frac{1}{\kappa^2}\sum_{u=x,y}U_u^*\frac{\partial^2(U_u\psi)}{\partial u^2} \rightarrow \frac{1}{\kappa^2}\sum_{j=2}^{N_y}\sum_{i=2}^{N_x}\sum_{ciclica}\left|\frac{U_{xij}\psi_{i+1j} - 2\psi_{ij} - U^*_{x;i-1j}\psi_{i-1j}}{a_x{}^2}\right| \qquad (4.53)$$

onde utilizamos o processo de permutação cíclica das coordenadas.

Por último, o cálculo da densidade de corrente total, que em nosso caso é o de um sistema 2D, fica:

$$\nabla \times \boldsymbol{B} = \frac{\partial B_{zij}}{\partial y}\hat{\imath} - \frac{\partial B_{zij}}{\partial x}\hat{\jmath} = \frac{\partial}{\partial y}\frac{1-W_{zij}}{i\kappa a_x a_y}\hat{\imath} - \frac{\partial}{\partial x}\frac{1-W_{zij}}{i\kappa a_x a_y}\hat{\jmath}\,. \tag{4.54}$$

onde o valor de B_{zij} foi substituído pelo valor da equação (4.34). Fazendo as aproximações das derivadas com as dimensões da célula unitária, a equação 4.54 fica:

$$\frac{\partial}{\partial y}\frac{1-W_{zij}}{i\kappa a_x a_y}\hat{\imath} - \frac{\partial}{\partial x}\frac{1-W_{zij}}{i\kappa a_x a_y}\hat{\jmath} = \frac{W_{zij}-W_{zi-1j}}{i\kappa a_y^2 a_x} - \frac{W_{zij}-W_{zij-1}}{i\kappa a_x^2 a_y} \tag{4.55}$$

Neste ponto temos os elementos que nos permitem escrever as equações de movimento da TDGL em termos de **U** e ψ, bem como as condições de contorno e as variáveis discretas. Assim, para a primeira equação da TDGL, temos:

$$\frac{\partial \psi_{ij}}{\partial t} = (\pounds_{\psi}[\psi, \mathbf{U}])_{ij} \tag{4.56}$$

onde $(\pounds_{\psi}[\psi, \mathbf{U}])_{ij}$ corresponde às equações (4.49) e (4.53). Para a malha supercondutora, temos:

$$(\pounds_{\psi}[\psi, \mathbf{U}])_{ij} = \sum_{j=2}^{N_y}\sum_{i=2}^{N_x}\left[\left(1 - \left|\psi_{ij}^2\right|\right)\psi_{ij} + \frac{1}{\kappa^2}\sum_{ciclica}\left|\frac{U_{xij}\psi_{i+1j} - 2\psi_{ij} - U^*_{x;i-1j}\psi_{i-1j}}{{a_x}^2}\right|\right] \tag{4.57}$$

Para a equação de movimento da segunda equação da TDGL, temos que transformar a taxa de variação do potencial vetor no tempo em termos do campo auxiliar. Então, fazendo a derivada da componente U_{xij} da equação (4.30) em relação ao potencial vetor, temos:

$$\frac{\partial U_{xij}}{\partial A_{xij}} = -i\kappa a_x\left[\exp\left(-i\kappa a_x A_{xij}\right)\right] = -i\kappa a_x U_{xij} \tag{4.58}$$

utilizando o operador $\frac{\partial}{\partial t}$, e comparando com a equação (4.26) temos:

$$\frac{\partial U_{xij}}{\partial t} = \frac{\partial}{\partial t}\left(U_{xij}\, U^*_{xi+1j}\right) = -i\kappa a_x \frac{\partial A_{xij}}{\partial t} \tag{4.59}$$

de acordo com a segunda equação da TDGL temos que:

$$\frac{\partial A_{xij}}{\partial t} = \frac{1}{\beta}\left(J_{sxij} - \frac{\partial}{\partial y}\frac{1-W_{zij}}{i\kappa a_x a_y}\hat{\imath}\right) \tag{4.60}$$

substituindo o termo entre parênteses pelas equações (4.38) e (4.55) temos:

$$\frac{\partial U_{xij}}{\partial t} = \frac{-i}{\beta}U_{xij}\left[Im\left(U_{xij}\psi^*_{ij}\psi_{i+1j}\right) - \kappa a_x \frac{B_{zij}-B_{zij-1}}{a_y}\right] \tag{4.61}$$

Vamos denotar o termo entre colchetes pela notação $(\pounds_{\boldsymbol{U}}[\psi, \mathbf{U}])_{ij}$, portanto:

$$\frac{\partial U_{xij}}{\partial t} = \frac{-i}{\beta}U_{xij}(\pounds_{\boldsymbol{U}}[\psi, \mathbf{U}])_{ij} \tag{4.62}$$

a equação de movimento para U_{yij} é obtida de maneira análoga.

A evolução temporal das equações (4.55) e (4.61) são obtidas por meio da integração numérica por passo, ou seja, fixamos um tempo (t), e somamos um pequeno intervalo de tempo (Δt), então temos:

$$\int_0^{t+\Delta t} \partial\psi_{ij} = \int_0^{t+\Delta t} (\pounds_\psi[\psi, \mathbf{U}])_{ij}\, \partial t \rightarrow$$

$$\psi_{ij}(t+\Delta t) = \psi_{ij}t + (\pounds_\psi[\psi, \mathbf{U}])_{ij}\Delta t \qquad (4.63)$$

onde: $(\pounds_\psi[\psi, \mathbf{U}])_{ij}t = \psi_{ij}t$ é o parâmetro de ordem em um passo de tempo anterior ao do termo com Δt. Para U_{xij} temos:

$$\int_0^{t+\Delta t} \frac{\partial U_{xij}}{U_{xij}} = \int_0^{t+\Delta t} \frac{-i}{\beta} (\pounds_{\boldsymbol{U}}[\psi, \mathbf{U}])_{ij}\ \partial t \rightarrow$$

$$U_{xij}(t+\Delta t) = U_{uij}(t) exp\left(\frac{-i}{\beta}(\pounds_{\boldsymbol{U}}[\psi, \mathbf{U}])_{ij}\right)\Delta t \qquad (4.64)$$

o componente U_{yij} é obtido de maneira análoga.

4.1. Perfil das correntes supercondutoras ao redeor de ADs quadrados

Eembora não seja possível estudarmos avalanches com a atual técnica usando as equações TDGL, podemos obter os mecanismos físicos envolvidos em tais eventos. Assim, um trabalho foi feito focado no acúmulo de correntes nos vértices de ADs. Foram considerados 16 ADs distribuídos em uma rede quadrada onde, em uma amostra, o espaçamento entre eles foi de 1ξ(0) e, na outra, de 14 ξ(0). Foi demostrado que os efeitos de acúmulo de corrente que ocorrem nos vértices dos ADs são dependentes do tamanho das amostras contudo, a amplitude de J nesses vértices não depende do espaçamento entre eles.

IEEE TRANSACTIONS ON APPLIED SUPERCONDUCTIVITY, VOL. 25, NO. 3, JUNE 2015 8800604

Profile and Crowding of Currents in Mesoscopic Superconductors With an Array of Antidots

D. Okimoto, E. Sardella, and R. Zadorosny

***Abstract*—Studies with mesoscopic superconducting materials have made significant advances in the last decades. One of the applications of such systems is in devices for single-photon and single-electron detectors. However, depending on the geometry of these systems, crowding current effects take place, and as a consequence, the total critical current could decrease, which facilitates the penetration of vortices. This effect could be also responsible for a variety of penetration morphologies of flux avalanches in macroscopic samples. Thus, in this paper, we used the time-dependent Ginzburg–Landau theory to study the crowding current effects in mesoscopic superconducting systems with an array of antidots. It is demonstrated that the profile of the currents is influenced by the antidots, i.e., in the vertices of the antidots, the intensity of the currents increases and distinguishably presents profiles, which depends on the size of the systems. Thus, we demonstrate that the distance between the antidots influences the current crowding effect, and the fabrication of future devices should be thought in order to minimize such effect.**

***Index Terms*—Antidots, crowding current (CC), mesoscopic, TDGL.**

I. Introduction

THE advances of nanofabrication techniques on the last decades stimulated significantly studies with materials in the meso and nanometric scales. Particularly, superconducting materials with such sizes are known as mesoscopic systems and exhibit a variety of behaviors which arise due to confinement effects [1]–[11]. As a consequence, such specimens can be used in applications like single photon [12]–[15] and single electron [16] detectors, amplifiers [17] and imaging of single magnetic quantum flux (single vortex) [18].

Another possible application is related to the control of the vortex penetration and motion by such mesoscopic systems since this can avoid dissipation and, consequently, should increase the critical current density, J_c, and the upper critical field, H_{c2} of the material. However, an effect described by Hagedorn and Hall in 1963 [19], i.e., the crowding current (CC) effect, initially applied to non-superconducting materials, can interfere on the functioning of the cited devices.

Manuscript received August 11, 2014; accepted November 15, 2014. Date of publication November 26, 2014; date of current version February 16, 2015. This work was supported in part by the Brazilian Agencies Funduncsp/PROPe under Grant 2115/002/14-PROPe/CDC and in part by the São Paulo Research Foundation (FAPESP) under Grants 2013/17719-8 and 2012/04388-0.

D. Okimoto and R. Zadorosny are with the Grupo de Desenvolvimento e Aplicações de Materiais, Departamento de Física e Química, Faculdade de Engenharia, Universidade Estadual Paulista, 15385-000 Ilha Solteira-SP, Brazil (e-mail: rafazad@yahoo.com.br).

E. Sardella is with the Departamento de Física, Faculdade de Ciências, Universidade Estadual Paulista, 17033-360 Bauru-SP, Brazil.

Color versions of one or more of the figures in this paper are available online at http://ieeexplore.ieee.org.

Digital Object Identifier 10.1109/TASC.2014.2376175

The CC effect is characterized by an agglomeration of the current lines in the regions where such current needs to suddenly change its flow direction, as to contour edges and defects. This crowding of the current can cause a decreasing of the total critical current of the system [20]–[26] and, as a consequence, these regions became good channels for the vortex penetration and the beginning of a resistive state. Some authors have already reported that the CC effect is also responsible for a variety of morphologies acquired by dendritic penetrations in systems with antidots, ADs, with different geometries [21]–[23], [27], [28]. In such case, the crowding of the current maximizes the Lorentz force over the magnetic flux trapped in the ADs and then guides the propagation of the flux avalanches by depinning the vortices.

In the present work we used the time-dependent Ginzburg–Landau theory to analyze the current crowding effect in mesoscopic superconducting materials with a square array of sixteen square antidots of fixed size. We varied the distances between the antidots and, consequently, the size of the systems. Thus, we analyzed the crowding of the currents in the vicinity of the ADs.

II. Theoretical Formalism

In the Ginzburg–Landau, GL, formalism the superconducting state is described locally by a complex order parameter ψ which the value of $|\psi|^2$ represents the density of Cooper pairs. In the case of type II superconductors the nucleation of vortices inside the material became energetically favorable. In the presence of an external field, flux could penetrate the material which causes the appearance of superconducting currents to shield the material. Then, to determine the local field, h, the order parameter, ψ, and the superconducting current density, $\mathbf{J}_s$, in the system, the normalized time dependent Ginzburg–Landau equations, TDGL, were used

$$\left(\frac{\partial}{\partial t}+i\varphi\right)\psi=-(-i\nabla-\mathbf{A})^2\psi+(1-T)\psi\left(1-|\psi|^2\right)$$

$$\beta\left(\frac{\partial \mathbf{A}}{\partial t}+\nabla\varphi\right)=\mathbf{J}_s-\kappa^2\nabla\times\mathbf{h} \tag{1}$$

where the supercurrent density is given by

$$\mathbf{J}_s=(1-T)\mathrm{Re}\left[\psi^*(-i\nabla-\mathbf{A})\psi\right]. \tag{2}$$

$\mathbf{A}$ is the vector potential which is related to the local magnetic field as $\mathrm{h}=\nabla\times\mathbf{A}$, and φ is the scalar potential. With the normalization, all the distances are in units of the coherence length at zero temperature $\xi(0)$; the magnetic field is in units of the

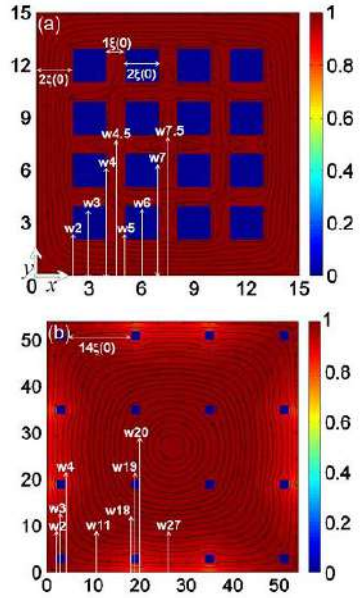

Fig. 1. Simulated systems (a) S_1 and (b) S_2. The notation $w\#$ indicates the fixed position in the x axis, and the arrows indicate the direction along the y axis, where the values of J_s were analyzed. The ADs were inserted at a distance of $2\xi(0)$ from the borders. However, the distance between them was changed by increasing the size of the system such that $d = 1\xi(0)$ for S_1 and $d = 14\xi(0)$ for S_2. This implies that the ADs in the S1 system covered an area of around 28%, and in S2, this percentage is ~2%.

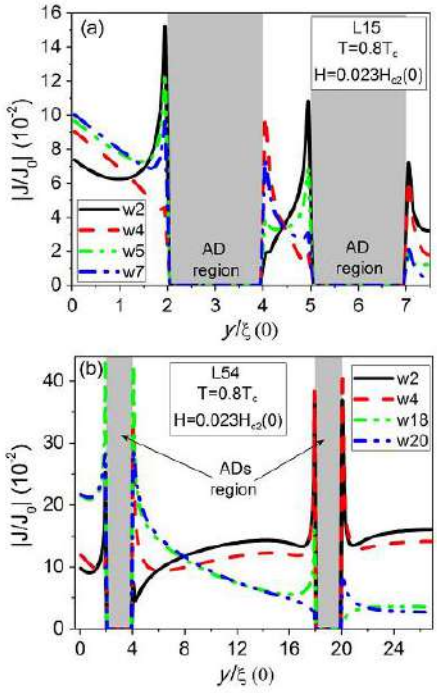

Fig. 2. Modulus of J_s along the y axis and for fixed positions for x coordinate, as illustrated in Fig. 1. The currents are amplified in most of the ADs vertices due to crowding effects. The (a) smaller system S_1 is more affected by the decreasing of J_s than the (b) larger one S_2, as can be seen by the evolution of the peaks in the vicinity of the vertices of different ADs.

zero temperature upper critical field $H_{c2}(0)$; the temperature T is in units of the critical temperature T_c; the current is in units of the depairing current J_0; the time is in units of the characteristic time $t_0 = \pi\hbar/8k_BT_c$; κ is the Ginzburg–Landau parameter; β is the relaxation time of $\mathbf{A}$, related to the electrical conductivity.

The TDGL equations are gauge invariant under the transformations $\psi' = \psi e^{i\chi}$, $\mathbf{A}' = \mathbf{A} + \nabla\chi$, $\varphi' = \varphi - \partial\chi/\partial t$ [29]. Thus, we conveniently choose the zero-scalar potential gauge, that is, $\varphi' = 0$ at all times and positions.

III. Results and Discussion

In our simulations, we worked with $\kappa = 5$, which is equivalent to a Pb-In alloy [30]. Thus, to study the effects of an array of ADs in mesoscopic superconductors, two square systems with different lateral sizes, $L = 15\xi(0)$ (which will be labeled S_1) and $54\xi(0)$ (which will be labeled S_2), were studied. In those systems, square ADs with lateral size of $2\xi(0)$ were disposed in a square array which counted with sixteen specimens, as shown in Fig. 1. The distance between the border of the systems and the ADs was maintained fixed as $2\xi(0)$. On the other hand, the distances d between the ADs were changed by increasing L. Fig. 1 shows the two simulated systems. The vertical arrows indicate the position for which the profile of the modulus of $\mathbf{J}_s$ (hereafter only J_s) was obtained, i.e., the notation $w\#$ indicates the fixed position in the x axis and the arrows indicate the direction along the y axis where the values of J_s were taken. Then, in Fig. 1(a) is shown the S_1 system and in Fig. 1(b) is shown the S_2 system. The black lines indicate the circulation of $\mathbf{J}_s$. For comparison, all the analysis were carried out in the Meissner state and at a fixed temperature and external applied magnetic field, $T = 0.8T_c$ and $H = 0.23H_{c2}(0)$, respectively.

In order to analyze how the profile of the J_s is affected by the ADs, we plotted $J(y)$ at fixed positions $w\#$. Fig. 2 shows such curves which were taken in the vicinity of the border of the ADs. Following the square symmetry of the system, the curves were ordered from outer to the inner border of the ADs. In general, and in both S_1 and S_2 systems, the currents are amplified at the vertices of the ADs as expected due to the CC. However, such amplification does not occur in all vertices which could be associated with the distance between the ADs and with the fact that the distribution of J_s decreases in the deeper regions in the system. The J_s distribution is also distinguishably affected in the superconducting region in between the ADs for S_1 and S_2, as can be verified in panels (a) and (b) of Fig. 2. Such behavior evidences that the profile of the currents is highly influenced by the distance of separation of the ADs and, consequently in this work, by the covered area of the system with ADs, i.e., the ADs in S_1 system covered an area of around 28% and in S_2 this percentage is ~2%. An interesting behavior is shown in panel 2(b) where J_s at $w2$ and $w4$ positions increases in the region between the ADs, i.e., in $4\xi(0) < y < 16\xi(0)$. On the other hand, at positions $w18$ and $w20$ (in the vicinity of the inner ADs), J_s decreases between neighboring ADs.

In Fig. 3 is shown the profile of J_s along the line which crosses the ADs in the middle, as denoted by the curves $w3$ and $w6$ for S_1 and $w3$ and $w19$ for S_2. The curves $w7$ and $w20$

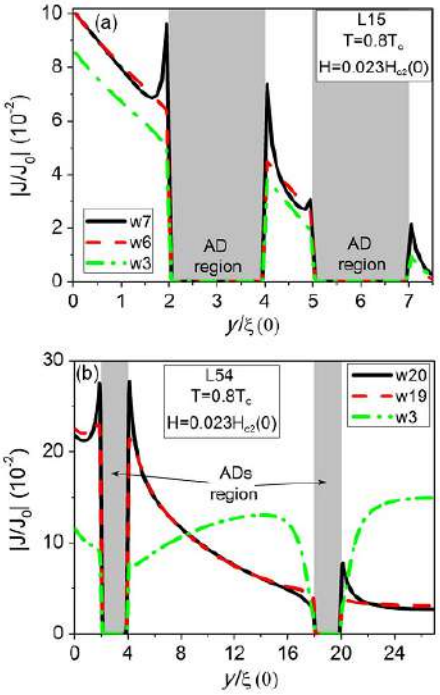

Fig. 3. Modulus of J_s along the y axis at fixed position of the x coordinate, which passes through the center of the ADs. In comparison with the curves, which pass in the vicinity of the ADs border—$w7$ for S_1 and $w20$ for S_2—in such regions, there is no presence of the crowding effects.

are inserted only for comparison purpose with the crowding effects which occur in the vertices. In general, there is no such effect in those regions. On the other hand, the presence of ADs do not affect the general behavior of J_s in those positions for both systems. The exception is the curve $w3$ for S_2 [panel Fig. 3(b)] for which J_s increases in between the ADs. This behavior should be related to the proximity to the border of the system where J_s increases as approximates to the middle of the lateral side ($y = L/2$).

The profile of J_s in the region between the ADs are shown in Fig. 4. The blue bars in such figure indicate the region which has an AD in the neighborhood. The curves of $w4.5$ and $w11$ for S_1 and S_2 respectively, are those in the vicinity of the left border of the system. Both curves present a similar behavior for which J_s does not vanish at the position $y = L/2$. Nonetheless, the curves $w7.5$ and $w27$ vanish at the center of the system. Besides some similar aspects, the profile of J_s is clearly influenced by the proximity of the ADs in S_1, but not by those of S_2.

IV. Conclusion

In this work we analyzed the profile of the modulus of the current in two mesoscopic superconducting systems with an array of ADs. It was shown that the crowding of the currents occurs in the vertices of the ADs even with the decreasing of J as the center of the systems are reached. It is worth to emphasize that in the smaller system, the ADs cover around 28% of the area of such system whereas the larger one presents only ~2% of covered area. Then, with a rouge distance between the ADs

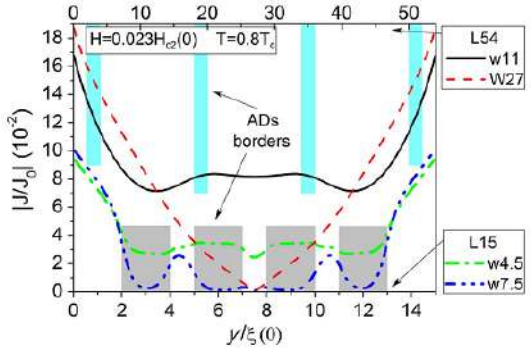

Fig. 4. Modulus of J_s along the y axis at fixed position of the x coordinate, which passes in between the ADs. The profile of the current is influenced by the ADs in S_1, but not in S_2. Such behavior is due to the proximity of the ADs, as indicated by the bars.

in the larger system, the J_s lines have enough space to accommodate in such regions. In this way, the crowding effect produces similar amplifications of J_s in the vertices of all ADs. On the other hand, the current crowding in the smaller system is highly dependent of the decreasing of J_s in the deeper regions. Thus, with such behavior, it is shown that the crowding of the currents in large systems (with a larger distance between the ADs) produces a similar amplification of J_s in the vertices of the ADs with that presented by systems with ADs closer to each other. Such systems should be used in future fluxonics devices. The behaviors demonstrated in this work can also be extended to real thin films since the currents are distributed along the entire system.

References

[1] M. R. Connoly, M. V. Miloševi, S. J. Bending, J. R. Clem, and T. Tamegai, "Continuum vs. discrete flux behaviour in large mesoscopic $Bi_2Sr_2CaCu_2O_{8+\delta}$ disks," *EPL*, vol. 85, no. 1, Jan. 2009, Art. ID. 17008.

[2] V. A. Schweigert, F. M. Peeters, and D. Singha, "Vortex phase diagram for mesoscopic superconducting disks," *Phys. Rev. Lett.*, vol. 81, no. 3, p. 2783, Sep. 1998.

[3] A. S. Melnikov *et al.*, "Evidence of a Lifshitz transition in the high-pressure behavior of the intermetallic compound $AuIn_2$," *Phys. Rev. B*, vol. 65, Apr. 2002, Art. ID. 140503(R).

[4] G. R. Berdiyorov, A. D. Hernádez-Nieves, M. V. Miloševi, F. M. Peeters, and D. Domínguez, "Flux-quantum-discretized dynamics of magnetic flux entry, exit, and annihilation in current-driven mesoscopic type-I superconductors," *Phys. Rev. B*, vol. 85, Mar. 2012, Art. ID. 092502.

[5] A. Müller, M. V. Miloševi, S. E. C. Dale, M. A. Engbarth, and S. J. Bending, "Superactivation of quantum nonlocality," *Phys. Rev. Lett.*, vol. 109, no. 19, Nov. 2012, Art. ID. 197003.

[6] E. Sardella, A. L. Malvezzi, P. N. Lisboa-Filho, and W. A. Ortiz, "Temperature-dependent vortex motion in a square mesoscopic superconducting cylinder: Ginzburg–Landau calculations," *Phys. Rev. B*, vol. 74, 2006, Art. ID. 014512.

[7] J. J. Palacios, "Metastability and paramagnetism in superconducting mesoscopic disks," *Phys. Rev. Lett.*, vol. 84, p. 1796, 2000.

[8] V. R. Misko, B. Xu, and F. M. Peeters, "Formation and size dependence of vortex shells in mesoscopic superconducting niobium disks," *Phys. Rev. B*, vol. 76, Jul. 2007, Art. ID. 024516.

[9] H. J. Zhao *et al.*, "Vortex states in mesoscopic superconducting squares: Formation of vortex shells," *Phys. Rev. B*, vol. 78, Sep. 2008, Art. ID. 104517.

[10] T. Cren, L. Serrier-Garcia, F. Debontridder, and D. Roditchev, "Vortex fusion and giant vortex states in confined superconducting condensates," *Phys. Rev. Lett.*, vol. 107, Aug. 2011, Art. ID. 097202.

[11] D. S. Golubovic, M. V. Miloševi, F. M. Peeters, and V. V. Moshchalkov, "Magnetically induced splitting of a giant vortex state in a mesoscopic superconducting disk," *Phys. Rev. B*, vol. 71, May 2005, Art. ID. 180502.

[12] G. N. Gol'tsman *et al.*, "Picosecond superconducting single photon optical detector," *Appl. Phys. Lett.*, vol. 79, no. 6, pp. 705–707, Aug. 2001.
[13] A. J. Kerman *et al.*, "Constriction-limited detection efficiency of superconducting nanowire single-photon detectors," *Appl. Phys. Lett.*, vol. 90, no. 10, Mar. 2007, Art. ID. 101110.
[14] S.N. Dorenbus *et al.*, "Low noise superconducting single photon detectors on silicon," *Appl. Phys. Lett.*, vol. 93, no. 13, Sep. 2008, Art. ID. 131101.
[15] G. R. Berdiyorov, M. V. Miloševi, and F. M. Peeters, "Spatially dependent sensitivity of superconducting meanders as single-photon detectors," *Appl. Phys. Lett.*, vol. 100, no. 26, Jun. 2012, Art. ID. 262603.
[16] M. Rosticher *et al.*, "A high efficiency superconducting nanowire single electron detector," *Appl. Phys. Lett.*, vol. 97, no. 18, Nov. 2010, Art. ID. 183106.
[17] B. H. Eom, P. K. Day, H. G. LeDuc, and J. Zmuidzinas, "A wideband, low-noise superconducting amplifier with high dynamic range," *Nature Phys.*, vol. 8, pp. 623–627, Jul. 2012.
[18] D. Vasyukov *et al.*, "A scanning superconducting quantum interference device with single electron spin sensitivity," *Nature Nanotech.*, vol. 8, pp. 639–644, Sep. 2013.
[19] F. B. Hagedorn and P. M. Hall, "Right-angle bends in thin strip conductors," *J. Appl. Phys.*, vol. 34, no. 1, pp. 128–133, 1963.
[20] W. A Jones *et al.*, "Impact of edge-barrier pinning in superconducting thin films," *Appl. Phys. Lett.*, vol. 97, no. 26, Dec. 2010, Art. ID. 262503.
[21] J. R. Clem and K. K. Berggren, "Geometry-dependent critical currents in superconducting nanocircuits," *Phys. Rev. B*, vol. 84, Nov. 2011, Art. ID. 174510.
[22] J. R. Clem, Y. Mawatari, G. R. Berdyorov, and F. M. Peeters, "Predicted field-dependent increase of critical currents in asymmetric superconducting nanocircuits," *Phys. Rev. B*, vol. 85, Apr. 2012, Art. ID. 144511.
[23] O.-A. Adami *et al.*, "Current crowding effects in superconducting corner-shaped Al microstrips," *Appl. Phys. Lett.*, vol. 102, no. 5, Feb. 2013, Art. ID. 052603.
[24] D. Henrich *et al.*, "Geometry-induced reduction of the critical current in superconducting nanowires," *Phys. Rev. B*, vol. 86, 2012, Art. ID. 144504.
[25] J. I. Vestgarden and T. H. Johansen, "Modeling non-local electrodynamics in superconducting films: The case of a right angle corner," *Supercond. Sci. Technol.*, vol. 25, no. 10, Oct. 2012, Art. ID. 104001.
[26] H. L. Hortensius, E. F. C. Driessen, T. M. Klapwijk, K. K. Berggren, and J. R. Clem, "Critical-current reduction in thin superconducting wires due to current crowding," *Appl. Phys. Lett.*, vol. 100, no. 18, Apr. 2012, Art. ID. 182602.
[27] R. Zadorosny *et al.*, "Morphology of flux avalanches in patterned superconducting films," *J. Supercond. Novel Magn.*, vol. 26, no. 6, pp. 2285–2288, Jun. 2013.
[28] M. Motta *et al.*, "Controllable morphology of flux avalanches in microstructured superconductors," *Phys. Rev. B*, vol. 89, Apr. 2014, Art. ID. 134508.
[29] W. D. Gropp *et al.*, "Numerical simulation of vortex dynamics in type-II superconductors," *J. Comput. Phys.*, vol. 123, no. 2, pp. 254–266, Feb. 1996.
[30] C. P. Poole, Jr., H. A. Farach, and R. J. Creswick, "Prozorov ruslan," in *Superconductivity.*, 2nd ed. Amsterdam, The Netherlands: Elsevier, 2007, p. 670.

4.2. Estudos dos limites de comportamentos de macro para mesoscópico e de macro para volumétrico (bulk)

Como a definição de supercondutor mesoscópico é muito genérica, em um trabalho consideramos amostras quadradas de vários tamanhos e em diferentes temperaturas de banho térmico. Dessa forma, mostramos que o limite mesoscópico se dá quando a rede de vórtices passa por um *crossover* onde há uma mescla de rede de Abrikosov com uma rede que segue a simetria da amostra (no nosso caso, quadrada). Adicionalmente, evidenciou-se, também, que este limite está bem acima dos valores apresentados pela profundidade de penetração do material, $\lambda(T)$.

PHYSICAL REVIEW B **85**, 214511 (2012)

Crossover between macroscopic and mesoscopic regimes of vortex interactions in type-II superconductors

Rafael Zadorosny,[1] Edson Sardella,[2] André Luiz Malvezzi,[3] Paulo Noronha Lisboa-Filho,[3] and Wilson Aires Ortiz[4,5]

[1]*Faculdade de Engenharia de Ilha Solteira, Universidade Estadual Paulista, Departamento de Física e Química, Caixa Postal 31, 15385-000, Ilha Solteira, São Paulo, Brazil*

[2]*Universidade Estadual Paulista, Instituto de Pesquisas Meteorológicas, CEP 17048-699 Bauru, São Paulo, Brazil*

[3]*Universidade Estadual Paulista, Departamento de Física, Faculdade de Ciências, Caixa Postal 473, 17033-360, Bauru, São Paulo, Brazil*

[4]*Departamento de Física, Universidade Federal de São Carlos, 13565-905, São Carlos, São Paulo, Brazil*

[5]*Centre for Advanced Study, Norwegian Academy of Science and Letters, NO-0271, Oslo, Norway*

(Received 1 November 2011; revised manuscript received 23 May 2012; published 11 June 2012)

In the present work we report the existence of a crossover between the macroscopic and mesoscopic regimes of vortex interactions in type-II superconductors. Our findings rely on a systematic procedure to determine this crossover, which is based on the influence of the surface on the vortex structure of small superconductors. An adjacent result that we have found is that near this regime transformation, the vortex lattice develops a progressive change of symmetry, from square to hexagonal, which is intimately related to the meso-to-macro crossover. Our numerical simulations have been done for a long superconducting cylinder of square cross section for a wide range of length scales and temperatures.

DOI: 10.1103/PhysRevB.85.214511 PACS number(s): 74.25.−q, 74.20.De, 74.78.Na

I. INTRODUCTION

In condensed matter physics, samples are usually considered to be large enough that the influence of finite dimensions on their properties is negligible; therefore, bulk behavior is assumed. This is not the case, however, in many situations of interest. Examples range from quantum size effects in metallic nanoparticles[1,2] and microfluidics,[3] to cluster size effects.[4] Hallmark physical ingredients in these systems are large surface-to-volume ratio and one or more dimensions of the sample approaching a relevant fundamental scale.

Mesoscopic superconductors also constitute a class of materials where size effects can play a relevant role to determine the vortex arrangement throughout the specimen.[5–16] In fact, even when only a few quanta of magnetic flux are nucleated into a mesoscopic sample, vortex interactions with other vortices and with the screening currents circulating around the edges give rise to a variety of configurations, such as giant vortices, multivortex states, or even hybrid states of both types. These configurations are strongly influenced by both the geometry and size of the sample. The occurrence of giant vortices in coherence length-sized samples have been predicted by several theoretical calculations,[17–22] although in some exotic confined geometries, such as a circular sector,[23] they were not observed.

Several authors have tried to detect this state experimentally. Kanda *et al.*[9–11] used multiple small tunnel junction measurements. They found that, by putting several small tunnel junctions symmetrically distributed on the disk edge, for some vorticities, they could not find any significant difference in the voltages at the contacts. This is taken as an indication of the occurrence of a giant vortex state. Some other authors have attempted to observe giant vortices by direct imaging technique. By using SQUID microscopy, in Refs. 14–16 they could not find giant vortex states in mesoscopic superconducting square and triangle samples. However, on using the Bitter pattern decoration technique in a niobium superconducting disk, Grigorieva *et al.*[13] observed clusters of multivortex states coexisting with giant vortices. In another work, Cren *et al.*[12] studied the vortex states in ultrathin single nanocrystals of Pb with random geometries via scanning tunneling microscopy. The images were taken under several values of applied field and at very low temperature. They showed that under certain conditions of magnetic field and sample size, a giant vortex is formed and in the vicinity of the core center the order parameter evolves as $|\psi| \propto r^L$ where L is the vorticity.

In the present work we show strong evidence that there exists a region of crossover between these vortex states in mesoscopic superconductors and the Abrikosov hexagonal vortex lattice in macroscopic superconductors. We have done so by studying the influence of the surface on the vortex configuration as a function of the sample size and temperature. Based on the physics governing the crossover between the mesoscopic and macroscopic behavior, we developed a criterion to determine a length scale that delineates the frontier between those two regimes. One could speculate that this crossover would occur for sample sizes of the order of the penetration depth $\lambda(T)$. As our results will show later on, the length scale that delimits the mesoscopic-macroscopic frontier differs quite significantly from what one might suspect.

The problem treated here was investigated within the scope of the Ginzburg-Landau theory. It is not uncommon to find papers arguing whether the Ginzburg-Landau theory could be applicable or not to the study of superconductivity at a mesoscopic level. This relevant issue has been discussed in detail in Refs. 17,24, and 25. In the latter, the authors have made a comparative analysis between the phenomenological Ginzburg-Landau theory and the microscopic Bogolyubov-De Gennes theory, for a mesoscopic superconducting square. They conclude that both theories produce very similar results.

The outline of this paper is as follows. First we provide a brief overview of the theoretical model used to obtain the equilibrium configurations of the superconducting state. Then, we describe the numerical method employed to solve the time-dependent Ginzbug-Landau (TDGL) equations for a superconductor in the presence of an external applied magnetic

field. The remainder of the paper is devoted to presentation and discussion of the results that emerge from our numerical simulations.

II. THEORETICAL FORMALISM

The superconducting state is usually described by the complex order parameter ψ. The quantity $|\psi|^2$ represents the electronic density of Cooper pairs. In the regions where $|\psi|^2$ is small, superconductivity is suppressed. At the center of the vortex $|\psi|^2 = 0$, whereas the local magnetic field $\mathbf{h}$ is maximum. The order parameter and the local magnetic field can be determined by the Ginzburg-Landau equations which, in their time-dependent formalism, are expressed by[26]

$$\left(\frac{\partial}{\partial t} + i\Phi\right)\psi = -(-i\nabla - \mathbf{A})^2\psi + (1-T)\psi(1-|\psi|^2)\,,$$
$$\beta\left(\frac{\partial \mathbf{A}}{\partial t} + \nabla\Phi\right) = \mathbf{J}_s - \kappa^2\nabla\times\mathbf{h}\,, \tag{1}$$

where $\mathbf{J}_s = (1-T)\Re[\psi^*(-i\nabla - \mathbf{A})\psi]$ is the supercurrent density; ψ is the order parameter, $\mathbf{A}$ is the vector potential, related to the local magnetic field as $\mathbf{h} = \nabla\times\mathbf{A}$, and Φ is the scalar potential. Here, the distances are measured in units of the coherence length at zero temperature $\xi(0)$; the magnetic field is in units of the zero temperature upper critical field $H_{c2}(0)$; the temperature T is in units of the critical temperature T_c; the time is in units of the characteristic time $t_0 = \pi\hbar/8k_BT_c$; κ is the Ginzburg-Landau parameter; β is the relaxation time of $\mathbf{A}$, related to the conductivity. We have adopted a linear dependence with respect to temperature for the phenomenological parameters in the Ginzburg-Landau theory [i.e., $H_{c2}(T) = H_{c2}(0)(1-T)$]. For small size superconductors this is also valid for temperatures well below T_c, despite the microscopic derivation of the TDGL equations being valid only for T very close to T_c.[27] Notice that the TDGL equations and their discretized form[21,28] are gauge invariant under the transformations $\psi' = \psi e^{i\chi}$, $\mathbf{A}' = \mathbf{A} + \nabla\chi$, $\Phi' = \Phi - \partial\chi/\partial t$. We chose the zero-scalar potential gauge, that is, $\Phi = 0$ at all times and positions.

In order to solve the TDGL equations, we have used the link variables method as delineated in Ref. 28. There are several extensions of this method. For instance, in Ref. 29 it has been adapted for very thin superconductors and in Ref. 23 for circular geometries. The simulations were carried out for samples with square geometry submitted to external magnetic fields applied along the cylinder axis, which is considered infinite. In principle, the TDGL equations can provide all transient states for a fixed external applied magnetic field. However, in this work we are only interested in the stationary states. We solved these equations starting from zero applied field, which was then increased adiabatically in small steps, $\Delta H = 10^{-4}$, until superconductivity was completely destroyed. At each step we let the system attain its equilibrium configuration and use such state as the initial condition for the next applied field.

III. RESULTS AND DISCUSSION

Let us now turn to the presentation of the results that arise from the numerical solution of equations (1). Our simulations have been carried out by using $\beta = 1$ and $\kappa = 5$ for a large number of superconducting square samples of side L, given in units of $\xi(0)$. Since we are interested only in the stationary states, this choice of β is adequate for the purposes. The lateral dimensions of the sample were varied in steps of $\Delta L = 1$ [also expressed in units of $\xi(0)$] and the temperature of simulations ranged from $T = 0$ to $T = 0.9375$ (in units of T_c).

The crucial issue here is to define a robust criterion to determine the characteristic size regulating the threshold among mesoscopic and macroscopic behavior. The following discussion depicts the reasoning that led us to stipulate this norm. It is well known that vortices nucleate at the central portions of the surface (i.e., not at the corners). Their complete development is preceded by a progressive deformation of the screening current mainstream which, otherwise, while the sample is in the Meissner phase, is parallel to the faces. As the applied field H is raised, this deformation proliferates into the sample until a vortex is completed. At this point, what was just a twist at the inception of the penetration process, becomes a curled screening current, enclosing the ingoing vortex. Thus, the pursuit for the threshold of the genuine mesoscopic behavior is equivalent to the search for the range of the interaction among vortices, which are just nucleating at the surfaces. Since this interaction is mediated by the superconducting regions, it should be detectable through all relevant superconducting properties (e.g., the order parameter, the magnitude and shape of the screening currents, and even the sample magnetization M).

Figure 1 illustrates this correlation for two samples of different sizes. As will become clear throughout this discussion, the largest among them ($L = 76$) has a macroscopic behavior, while the other ($L = 26$) exhibits mesoscopic superconductivity. The magnetization versus field curves shown in Fig. 1(a) for both samples exhibit clear jumps at the field H_j, corresponding to the first entrance of vortices into the sample. Noticeably, $M(H)$ for sample $L = 26$ develops a local minimum at H_m, nonexistent for sample $L = 76$. This minimum reflects a delay (in field) of vortex invasion, due to the repulsive interaction between the entities, which are nucleating at the borders [see Fig. 1(b), upper $L = 26$ panel]. Differently from the case for the larger sample [Fig. 1(b), upper $L = 76$ panel], the excessive proximity of the surfaces in sample $L = 26$ causes a strong repulsion between each vortex and its counterparts, even while embryonic at the other surfaces, which causes a non-negligible degradation on the screening capability, due to the extra repulsive barrier. This degradation is clearly manifested on $M(H)$ curves, whose deviation from the Meissner response for a bulk sample ($-4\pi M = H$) increases with decreasing L. The upper $L = 26$ and $L = 76$ panels in Fig. 1(b) also capture the situation, delineating the order parameter at the field H_j. The color code is such that dark red regions are fully screened, while dark blue tones represent strongly suppressed superconductivity. While four vortices[30] are being generated at the surfaces of both samples, the order parameter at the very center of the macroscopic sample ($L = 76$) is preserved, even though vortices are just about to enter; contrarily, the tones

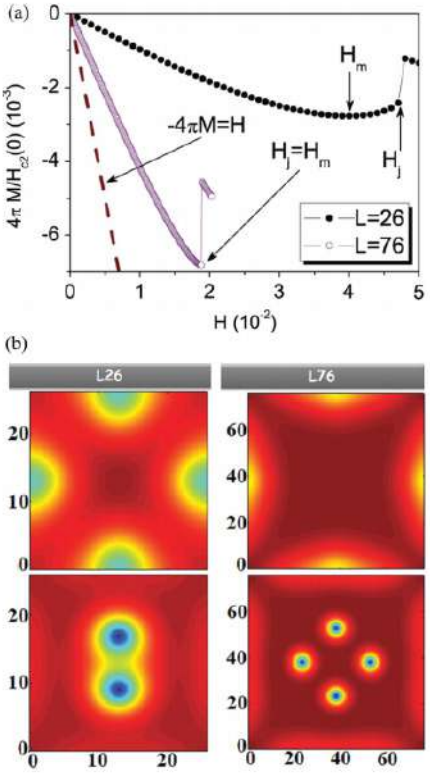

FIG. 1. (Color online) (a) Magnetization versus field curves for samples $L = 26$ and $L = 76$ at $T = 0.875$. As L increases, H_j and H_m (seen for $L = 26$) tend to approach each other and the minimum on the magnetization curve, coincident with H_j for $L = 76$, disappears for $L > 76$, on the magnetization curve disappears. (b) Upper and lower $L = 26$ panels show the order parameter for this sample, immediately before and after the first entrance of vortices (H_j and $H_j + 10^{-4}$, respectively). The same applies for the upper and lower $L = 76$ panels. Noticeably, as discussed in the text, only two vortices appear for $L = 26$. Notice also that the sample sizes are represented as equal, although their side ratio is $76/26 \approx 3$.

at the central portion of the mesoscopic sample ($L = 26$) are somewhat lighter, indicating that screening currents are already circulating in that region, and the nucleating vortices do interact with each other. The lower $L = 26$ and $L = 76$ panels in Fig. 1(b) depict the situation immediately after vortex entrance (i.e., at $H = H_j + 10^{-4}$) further emphasizing the repulsion among the entities that are being formed. While for the larger sample, all nucleating vortices manage to enter at H_j, the mesoscopic sample is not able to host all four at once and, as they would not fit along, only two vortices enter.

Even though one can visualize such differences and, accordingly, infer the existence of a limiting frontier among both regimes, it is not an easy task to assign a specific value of L for the threshold size. As will be further discussed in this paper, the meso-to-macroscopic frontier separates a region of pure macroscopic behavior from another where mesoscopic and macroscopic characteristics coexist. Based on our simulations for a large number of samples with different sizes, we came

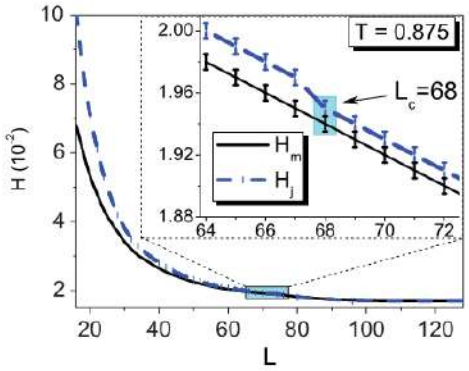

FIG. 2. (Color online) Size dependence of H_j and H_m, indicating that both superimpose (within the precision bar of the simulations) above the threshold value L_c. The zoomed area highlights the saturation point.

to the conclusion that the occurrence of local minima on the magnetization curves is due solely to the additional repulsion among vortices, which become important when the sample dimensions are sufficiently small, a feature that we take as the guiding line to quantify the meso-macro threshold criterion for such a rather subtle crossover. Thus, for a fixed temperature, we take the critical size L_c as that for which $H_m = H_j$. This means that, for sizes greater than L_c, the sample behaves as a macroscopic superconductor, in the sense that vortices nucleating at opposite sides do not interact before entering: below L_c, the mesoscopic regime dominates, as a consequence of the size of the sample being smaller than the interaction range. Figure 2 shows the size dependence of H_m and H_j for $T = 0.875$. The zoomed up box emphasizes the difference among both quantities; the vertical bars correspond to the width of the field step in our simulations, $\Delta H = 10^{-4}$. Taking the critical size as that above which the vertical bars start to overlap, we determined $L_c = 68$ for this temperature.

We have also investigated the surface contribution to the magnetic free energy of the system in the whole range of values of L studied here. At the jump, this energy term is proportional to the difference among two field integrals, between zero and H_j, of the magnetization: the bulk (i.e., surface-free) case, exhibiting a perfect Meissner response ($-4\pi M = H$), and the finite sample, for which the magnetization is affected by repulsion among nucleating vortices. To illustrate this point, the energy of the state of the sample immediately before the first penetration is shown in Fig. 3, as a function of the sample size. As can be seen, such energy decreases monotonically with L and its derivative saturates, within a certain precision indicated by the error bars, at a length scale that is quite close to $L_c(T)$ found by the criterion described previously. Our search for other evidences of this regime transformation included the size dependence of the initial slope of $M(H)$, which also exhibits a smooth variation with respect to L.

The following remarkable characteristics of this meso-to-macroscopic crossover were observed: (i) for $L > L_c$, at any temperature, the symmetry of the vortex lattice is hexagonal, as shown in the upper $L = 96$ panel of Fig. 4, which also indicates that it is destroyed upon increase of the field, from $H = 0.126$

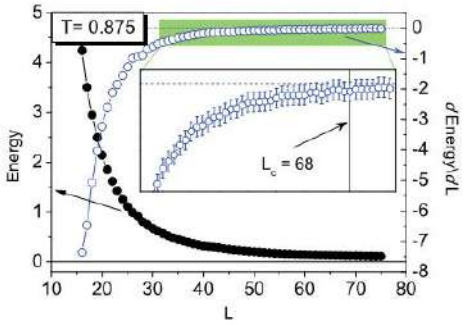

FIG. 3. (Color online) Black circles: energy as a function of L; blue circles: derivative of the energy with respect to L. The energy was calculated as $\int_0^{H_j} B\,dH$, where B is the induction, and H_j is the field right before the first entrance of vortices; in this calculation, only the magnetic field energy inside the superconductor is accounted for. The temperature is $T = 0.875$.

to $H = 0.127$, and that superconductivity remains only at the borders. Notice that there is a quite close coincidence between this field and $H_{c2}(T = 0.875) = 1 - 0.875 = 0.125$, which represents the applied field sufficient to destroy the vortex lattice for a bulk superconductor. We will comment further about it later on. (ii) For $L \ll L_c$ the vortex lattice most predominantly has square symmetry; depending on T and L, one can also have giant vortex states coexisting with single vortices.[20,21] Such behavior can be seen in the lower $L = 20$ panel of Fig. 4; for $H = 0.110$, two vortices penetrate the sample and a giant vortex with two flux quanta is formed at the center. Nonetheless, for $H = 0.126$, two more vortices enter into the sample and the giant vortex splits in four separate entities, following the fourfold symmetry of the problem. (iii) The most interesting characteristic of the meso-to-macro occurs for $L \lesssim L_c$; for high external applied fields, that is, close to the Abrikosov upper critical field $H_{c2}(T)$, when the density of vortices is large, the lattice develops a progressive crossover from hexagonal to square symmetry. We illustrate this scenario in the $L = 64$ panels of Fig. 4 for $T = 0.875$. As shown in this figure, for applied fields still low but sufficient to form a vortex lattice ($H = 0.110$) the symmetry is hexagonal. As we increase the field, the symmetry is somewhat mixed, with hexagons at the central portions of the sample and squares closer to the edges, as illustrated for $H = 0.113$ and $H = 0.123$. For even higher fields ($H = 0.127$), the lattice is eventually destroyed and surface superconductivity survives only at the surface.

We have also studied the system for lower temperatures, as exemplified in Fig. 5 for $T = 0.3125$, at which $L_c = 38$. To describe the vortex configurations around L_c, two samples were chosen, one right below ($L = 36$) and the other right above ($L = 40$) the crossover value. For $H = 0.600$, vortices are displayed in hexagonal lattices for both samples. However, at $H = 0.620$ and $H = 0.694$, triangular and square vortex lattices coexist for sample $L = 36$, whereas for these same values of the applied field, the vortex lattice remains triangular for sample $L = 40$. Eventually, at sufficiently high applied fields, the vortex lattice is entirely destroyed on both samples; for $T = 0.3125$ the suppression of the vortex

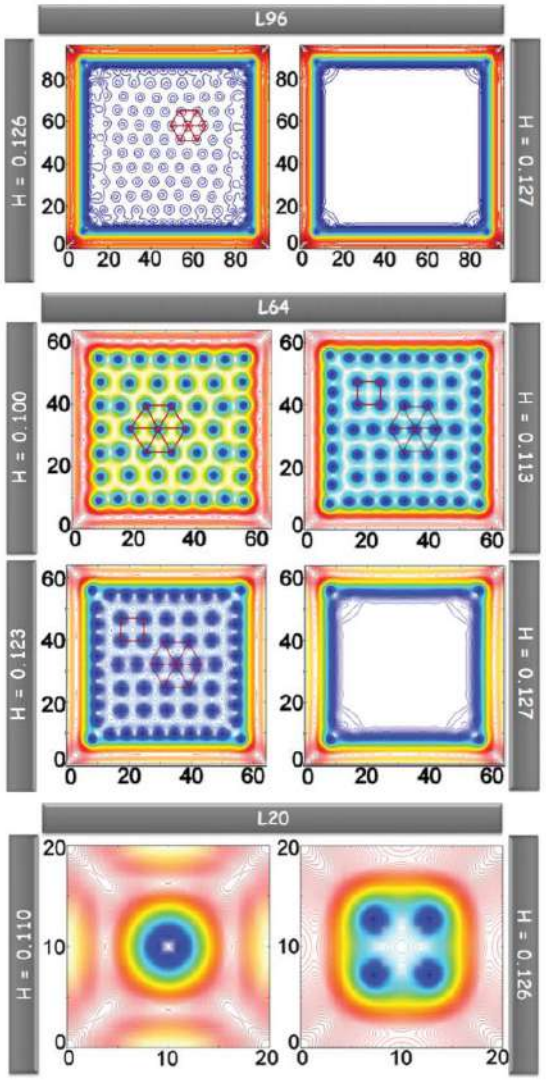

FIG. 4. (Color online) Vortex lattice for samples $L = 96$, $L = 64$, and $L = 20$ for several values of the external field at temperature $T = 0.8750$. The upper panel shows that a hexagonal vortex lattice is maintained until the suppression of superconductivity in the center of the sample $L = 96$. In the middle panel, the crossover of the vortex lattice, that takes place below the threshold line, is shown for sample $L = 64$. The lower panel shows that, far below the threshold line L_c (in this case $L = 20$), the vortices follow the symmetry of the sample due to size effects.

lattice occurs at $H = 0.695$. Again, notice that this field, as already seen for $T = 0.875$, is very close to the upper critical field $H_{c2}(T = 0.3125) = 1 - 0.3125 = 0.6875$. We see thus that, for different temperatures, the value of the applied field sufficient to destroy the lattice, but not superconductivity at the surface, is quite close to the Abrikosov field $H_{c2}(T)$ for bulk samples. We take this as a robust evidence of the accuracy of our simulations. At $T = 0.875$, only surface superconductivity remains on sample $L = 64$ for $H \geqslant 0.127$ (Fig. 4); the same

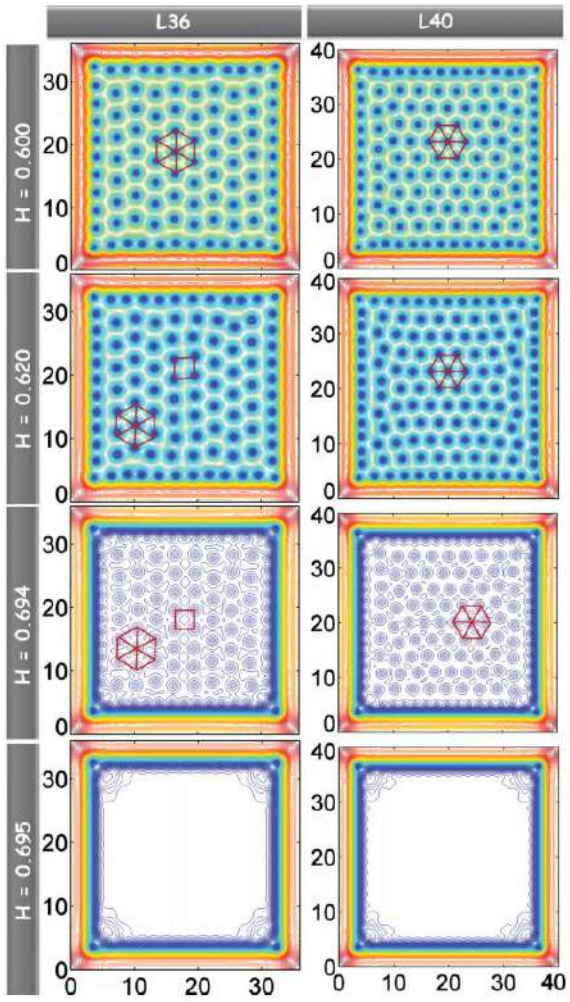

FIG. 5. (Color online) Vortex lattice for samples $L = 36$ and $L = 40$ for several values of the external field, at $T = 0.3125$. Notice that, for the macro sample ($L = 40$), vortices always form a hexagonal lattice. A crossover between hexagonal and square lattices takes place for the mesoscopic sample ($L = 36$). Right below L_c, the system starts developing a hexagonal lattice for low densities of vortices, but still carries vestiges of the mesoscopic regime as this density increases, developing a mixture of square and hexagonal vortex lattice.

at $T = 0.3125$ (Fig. 5) feature occurs for samples $L = 36$ and $L = 40$ for $H \gtrsim 0.695$.

As stressed before, the vortex lattice always displays hexagonal symmetry for sample dimensions above L_c. A quantitative evidence, that the picture that comes out from the simulations indeed corresponds to a triangular lattice, can be obtained from the structure factor of the system. Figure 6 shows contour plots of the order parameter [Figs. 6(a) and 6(c)] and the corresponding structure factors of the vortex lattice for sample $L = 128$ at $H = 0.126$ [Fig. 6(b)] and $H = 0.127$ [Fig. 6(d)]. Considering the peak values of the structure factor in Fig. 6(b), we obtained the vector basis oriented

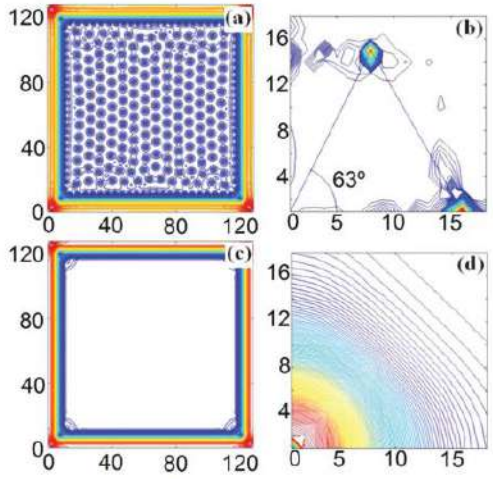

FIG. 6. (Color online) Topology of the superconducting density of the Cooper pairs $|\psi|^2$, and its corresponding structure factors, for sample $L = 128$. Top: $H = 0.126$, bottom: $H = 0.127$. Notice that the vortex lattice disappears abruptly at $H = 0.127$ [panels (c) and (d)], close to the Abrikosov bulk upper critical field $H_{c2}(T = 0.875) = 0.125$. The structure factor was calculated as the absolute value of the fast Fourier transform of $|\psi|$.

as approximately an equilateral triangle, as expected for an Abrikosov type-II superconductor. Notice that just a small increase in the applied field destroys the vortex lattice and the peaks in the structure factor disappear [Figs. 6(c) and 6(d)]. It is therefore clear that, for $L = 128$, the system is already in the macroscopic regime, exhibiting a genuine Abrikosov lattice, which disappears along with volume superconductivity.

In order to construct an L-T phase diagram, we repeated, for several temperatures, the procedure employed to determine L_c, as discussed above and exemplified in Figs. 1 and 2. The resulting phase diagram is shown in Fig. 7. Such diagram separates the region where the superconductor behaves predominantly as a macroscopic sample from that where a mesoscopic behavior takes place. We have used the expression $L_c(T) = L_0(1 - T)^n$ to fit the data, considering L_0 and n as free adjustable parameters. The value of L_0 corresponds to the length scale for which the mesoscopic-macroscopic transformation occurs at zero temperature; n is the critical exponent. The best fit, shown in Fig. 7 along with the data, gives $L_0 = 36.5$ and $n = -0.292 \approx -2/7$. Thus, it is clear that the length scale for the crossover between both regimes is much larger than the London penetration depth $\lambda(T) = \kappa/\sqrt{1 - T}$. A comparison between $L_c(T)$ and $\lambda(T)$ can be seen in Fig. 7. In real units, if we take $\xi(0) = 10$ nm, which is a typical size of low T_c type-II superconductors, then the value of $L_c(T)$ would range from 365 to 1150 nm as T varies from zero to 0.9375. This is of the same order of magnitude where size effects disappear in nanoparticle systems.[31]

The threshold line changes very little for different materials, as one can infer from the two curves shown in Fig. 7, for $\kappa = 5$ and $\kappa = \infty$. Not only the values for the infinity κ limit of the TDGL equations differ only a few percent from those obtained for $\kappa = 5$, but also the overall tendency of the two curves is similar, to an extent that the fitting exponent for both

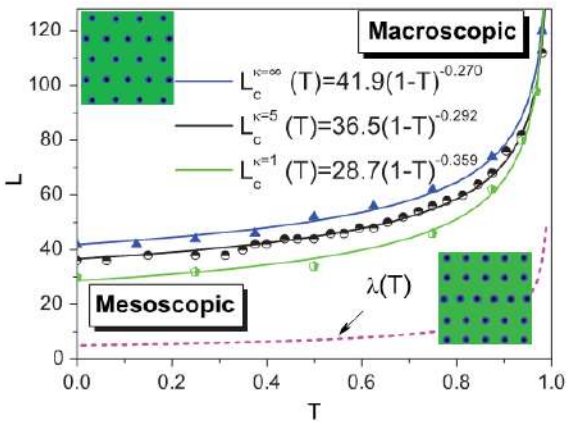

FIG. 7. (Color online) The L_c-T phase diagram; above the critical line the superconductor behaves as a macroscopic sample; below it, a mesoscopic behavior takes place. The insets indicate that for $L > L_c$ the lattice is always hexagonal, whereas for $L < L_c$ the system may develop other types of symmetries (see text). $\lambda(T)$ for $\kappa = 5$ is also shown for comparison.

is virtually the same ($\sim -2/7$), as evidenced in Fig. 7. It is not surprising that there is no significant differences between the characteristics of the $L_c(T)$ curves, since the vortex states are indistinguishable for $\kappa \gtrsim 5$, as it was demonstrated in Ref. 32. For low values of κ the $L_c(T)$ curve presents the same dependence with T, however, if such curve is compared with that one for $\kappa = 5$, significant changes can be observed in the value of the n exponent, which is approximately $-5/14$, and the value of L_0.

Recently, Connolly *et al.*[33] have made a similar study in order to find the meso-to-macro crossover for a superconducting disk. They used a criterion based in the competition between Abrikosov vortex lattice and shell-like ordering. As a result, they obtained that the crossover occurs in the diameter range of $[20\lambda(T), 40\lambda(T)]$ [in our units, $(20\kappa/\sqrt{1-T}, 40\kappa/\sqrt{1-T})$], which differs from our results for large κ.

As a final remark, we can surely say that our mapping of the frontier between the mesoscopic and macroscopic length scale could be an important guide for the fabrication of samples with desirable dimensions for which one can observe mesoscopic effects in superconductivity.

IV. CONCLUSION

In short, based on the physical evidence that, in the mesoscopic regime, vortices nucleating at the sample surface interact with each other even at the very early stages of their inception, we have developed a systematic procedure to determine the crossover between mesoscopic and macroscopic regimes of superconductivity in small samples. The progressive change of symmetry of the vortex lattice, from square to hexagonal, is intimately related to the meso-to-macro crossover and further emphasizes the robustness of our criterion.

ACKNOWLEDGMENTS

The authors thank the Brazilian agencies Fundação de Amparo à Pesquisa do Estado de São Paulo (FAPESP) and Conselho Nacional de Desenvolvimento Científico e Tecnológico (CNPq) for financial support. W.A.O. acknowledges the Centre for Advanced Study (Norway) for the hospitality during the last stage of this work.

[1]W. P. Halperin, Rev. Mod. Phys. **58**, 533 (1986).
[2]Y. G. Sun and Y. N. Xia, Science **298**, 2176 (2002).
[3]D. J. Harrison, K. Fluri, K. Seiler, Z. H. Fan, C. S. Effenhauser, and A. Manz, Science **261**, 895 (1993).
[4]F. Baletto and R. Ferrando, Rev. Mod. Phys. **77**, 371 (2005).
[5]A. K. Geim, S. V. Dubonos, J. G. S. Lok, M. Henini, and J. C. Maan, Nature (London) **396**, 144 (1998).
[6]A. K. Geim, S. V. Dubonos, I. V. Grigorieva, K. S. Novoselov, F. M. Peeters, and V. A. Schweigert, Nature (London) **407**, 55 (2000).
[7]M. Morelle, J. Bekaert, and V. V. Moshchalkov, Phys. Rev. B **70**, 094503 (2004).
[8]D. S. Golubovic, M. V. Milošević, F. M. Peeters, and V. V. Moshchalkov, Phys. Rev. B **71**, 180502 (2005).
[9]A. Kanda, B. J. Baelus, F. M. Peeters, K. Kadowaki, and Y. Ootuka, Phys. Rev. Lett. **93**, 257002 (2004).
[10]B. J. Baelus, A. Kanda, F. M. Peeters, Y. Ootuka, and K. Kadowaki, Phys. Rev. B **71**, 140502 (2005).
[11]M. V. Milošević, A. Kanda, S. Hatsumi, F. M. Peeters, and Y. Ootuka, Phys. Rev. Lett. **103**, 217003 (2009).
[12]T. Cren, L. Serrier-Garcia, F. Debontridder, and D. Roditchev, Phys. Rev. Lett. **107**, 097202 (2011).
[13]I. V. Grigorieva, W. Escoffier, V. R. Misko, B. J. Baelus, F. M. Peeters, L. Y. Vinnikov, and S. V. Dubonos, Phys. Rev. Lett. **99**, 147003 (2007).
[14]S. Okayasu, T. Nishio, Y. Hata, J. Suzuki, I. Kakeya, K. Kadowaki, and V. V. Moshchalkov, IEEE Trans. Appl. Supercond. **15**, 696 (2005).
[15]T. Nishio, Q. Chen, W. Gillijns, K. De Keyser, K. Vervaeke, and V. V. Moshchalkov, Phys. Rev. B **77**, 012502 (2008).
[16]T. Nishio, S. Okayasu, J. Suzuki, and K. Kadowaki, Physica C **412**, 379 (2004); **414**, 379 (2004).
[17]L. F. Chibotaru, A. Ceulemans, V. Bruyndoncx, and V. V. Moshchalkov, Nature (London) **408**, 833 (2000).
[18]V. A. Schweigert, F. M. Peeters, and P. S. Deo, Phys. Rev. Lett. **81**, 2783 (1998).
[19]A. S. Mel'nikov, I. M. Nefedov, D. A. Ryzhov, I. A. Shereshevskii, V. M. Vinokur, and P. P. Vysheslavtsev, Phys. Rev. B **65**, 140503 (2002).
[20]B. J. Baelus and F. M. Peeters, Phys. Rev. B **65**, 104515 (2002).
[21]E. Sardella, A. L. Malvezzi, P. N. Lisboa-Filho, and W. A. Ortiz, Phys. Rev. B **74**, 014512 (2006).

[22]B. Xu, M. V. Milošević, S. H. Lin, F. M. Peeters, and B. Janko, Phys. Rev. Lett. **107**, 057002 (2011).
[23]E. Sardella, P. N. Lisboa-Filho, and A. L. Malvezzi, Phys. Rev. B **77**, 104508 (2008).
[24]L. F. Chibotaru, A. Ceulemans, V. Bruyndonex, and V. V. Moshchalkov, Phys. Rev. Lett. **86**, 1323 (2001).
[25]L. F. Chibotaru and V. V. Moshchalkov (private communication).
[26]A. Schmid, Phys. Kondens. Mater. **5**, 302 (1966).
[27]R. Geurts, M. V. Milošević, and F. M. Peeters, Phys. Rev. B **81**, 214514 (2010).
[28]W. D. Gropp, H. G. Kaper, G. K. Leaf, D. M. Levine, M. Palumbo, and V. M. Vinokur, J. Comput. Phys. **123**, 254 (1996).
[29]M. V. Milošević and R. Geurts, Physica C **470**, 791 (2010).
[30]Fourfold symmetry: first penetration involves simultaneous nucleation of four vortices.
[31]A. S. Barnard, Rep. Prog. Phys. **73**, 1 (2010).
[32]Q. Du, M. D. Gunzburger, and J. S. Peterson, Phys. Rev. B **51**, 16194 (1995).
[33]M. R. Connolly, M. V. Milošević, S. J. Bending, J. R. Clem, and T. Tamegai, Europhys. Lett. **85**, 17008 (2009).

Um dos resultados do trabalho ora apresentado, mostrava que quanto menor a amostra, mais a reta Meissner se aproxima daquela de um supercondutor volumétrico (bulk). Assim, juntamente com minha aluna de IC, na época, publicamos o trabalho a seguir. Como não é possível simular amostras muito grandes por TDGL, devido ao altíssimo tempo computacional, acabamos por fazer uma projeção do limite "bulk".

Physica C 492 (2013) 75–79

Contents lists available at SciVerse ScienceDirect

Physica C

journal homepage: www.elsevier.com/locate/physc

Study of the threshold line between macroscopic and bulk behaviors for homogeneous type II superconductors

A. Presotto [a], E. Sardella [b,c], R. Zadorosny [a,*]

[a] Grupo de Desenvolvimento e Aplicações de Materiais, Faculdade de Engenharia de Ilha Solteira, Universidade Estadual Paulista – UNESP, Departamento de Física e Química, Caixa Postal 31, CEP 15385-000 Ilha Solteira, SP, Brazil
[b] Faculdade de Ciências, Universidade Estadual Paulista – UNESP, Departamento de Física, Caixa Postal 473, CEP 17033-360 Bauru, SP, Brazil
[c] UNESP – Universidade Estadual Paulista, IPMet – Instituto de Pesquisas Metereológicas, CEP 17048-699 Bauru, SP, Brazil

ARTICLE INFO

Article history:
Received 6 March 2013
Received in revised form 13 May 2013
Accepted 21 May 2013
Available online 10 June 2013

Keywords:
TDGL
Bulk
Macroscopic

ABSTRACT

In this work we solved the time dependent Ginzburg–Landau equations to simulate homogeneous superconducting samples with square geometry for several lateral sizes. As a result of such simulations we notice that in the Meissner state, when the vortices do not penetrate the superconductor, the response of small samples are not coincident with that expected for the bulk ones, i.e., $4\pi M = -H$. Thus, we focused our analyzes on the way which the $M(H)$ curves approximate from the characteristic curve of bulk superconductors. With such study, we built a diagram of the size of the sample as a function of the temperature which indicates a threshold line between macroscopic and bulk behaviors.

1. Introduction

The advances in nanofabrication techniques which occurred on the last decades stimulated the production and, consequently, experimental and theoretical studies of superconducting samples with sizes of the order of their fundamental lengths, i.e., $\lambda(T)$ and $\xi(T)$. In such materials the superconducting properties and the vortex dynamics are hugely affected by confinement effects. As a consequence, multi and giant vortex states takes place [1–20] as well as the coexistence of vortex and antivortex pairs.[6] Such systems also present others exotic behaviors as non-quantized vortex penetration [21] and the arrangement of the vortex lattice in several geometries which follow the symmetry of the samples [1,4,8,22–31].

Recently, theoretical studies with mesoscopic superconductors of type I shown that an applied current in a slab induced the penetration and annihilation of single quantized vortex in the intermediate state [32]. The confinement effects can also induced the suppression of the intermediate state and drastically changed the size and temperature dependence of the critical fields of such materials [33].

It is interesting to note that, in all cited works, the mesoscopic superconductors are treated, generically, as materials of reduced dimensions of the order of $\lambda(T)$ or $\xi(T)$. However, no much attention is done on the real sizes for which a sample could be defined as a mesoscopic specimen. Thus, it is worth to emphasize that the knowledge of the relation between size and superconducting behavior is very important to guide the researchers in their theoretical and experimental studies. Recently, Connolly et al. [34] published a work where they used a criterion based on the competition between the Abrikosov vortex lattice and a shell-like ordering to define a meso-to-macroscopic crossover of a superconducting disk. With the same purpose, the authors of the Ref. [26] proposed the existence of a threshold line between mesoscopic and macroscopic superconducting behaviors. For the mesoscopic-like behavior, the confinement effects are strong enough to induce a crossover of the the vortex lattice and the vortices arrangement follows the symmetry of the sample. Nevertheless, the macroscopic behavior is mainly characterized by some volumetric properties like the value of the upper critical field $H_{c2}(T)$ and the presence of the hexagonal vortex lattice. However, in this state the outer vortices are influenced by the surface and are arranged in a kind of shell.

A possible question that should arise from such analysis is about the typical sizes for which the surface effects could be neglected. Thus, in the present work we determined a possible threshold line between the macroscopic and bulk behaviors. This last one have been defined as the samples for which the influence of the surface on the vortex dynamics could be neglect. In this way, the outline of our work is as follow. First, in Section 2, we provide an overview of the theoretical formalism used to run the simulations. Next, in Section 3 we describe some definitions used in this paper and an overview of a previous work which was the motivation for the present one. In the remainder Sections 4 and 5 we dis-

* Corresponding author. Tel.: +55 18 3743 1903; fax: +55 18 3742 4868.
E-mail addresses: rafazad@yahoo.com.br, rafazad@dfq.feis.unesp.br (R. Zadorosny).

0921-4534/$ - see front matter © 2013 Elsevier B.V. All rights reserved.
http://dx.doi.org/10.1016/j.physc.2013.05.017

cuss our results and the criteria used to obtain the crossover line between macro-to-bulk behaviors and present our conclusions.

2. Theoretical formalism

The phenomenological theory developed by Ginzburg and Landau (GL for short) [35] is a very important tool to study the behavior of type I and type II superconductors. In such theory, the superconducting state is described by a complex order parameter ψ, for which the physical quantity $|\psi|^2$ represents the density of superconducting carriers, i.e., the Cooper pairs, and the vector potential $\mathbf{A}$ which is related with the local magnetic field by $\mathbf{h} = \nabla \times \mathbf{A}$. The Ginzburg–Landau equations in their time-dependent form are expressed by [36]

$$\left(\frac{\partial}{\partial t} + i\Phi\right)\psi = -(-i\nabla - \mathbf{A})^2\psi + (1-T)\psi(1-|\psi|^2),$$

$$\beta\left(\frac{\partial \mathbf{A}}{\partial t} + \nabla\Phi\right) = \mathbf{J}_s - \kappa^2\nabla \times \mathbf{h}, \tag{1}$$

where $\mathbf{J}_s = (1-T)\Re[\psi^*(-i\nabla - \mathbf{A})\psi]$ is the supercurrent density, and Φ is the scalar potential; these two equations are commonly referred to as time dependent Ginzburg–Landau equations (TDGL for short). Thus, the time evolution of a superconducting system and, consequently, the evolution of the vortices even in non-stationary states, could be followed. However, for our purposes, we will use the TDGL equations just as a relaxation method to achieve the stationary state. This is only a matter of convenience, since we could solve the GL equations by other means. For example, we could solve then by finite elements methods (see for instance Ref. [37].

Here, the distances are measured in units of the coherence length at zero temperature $\xi(0)$; the magnetic field is in units of the zero temperature upper critical field $H_{c2}(0)$; the temperature T is in units of the critical temperature T_c; the time is in units of the characteristic time $t_0 = \pi\hbar/8k_BT_c$; κ is the Ginzburg–Landau parameter; β is the relaxation time of $\mathbf{A}$, related to the conductivity. Rigorously speaking, the Ginzburg–Landau theory is applicable only for temperatures close to T_c. However, as we are interested in a general feature of a threshold line between macro-to-bulk superconducting behaviors, we have adopted a linear dependence with respect to the temperature for the phenomenological parameters in the Ginzburg–Landau theory, i.e., $H_{c2}(T) = H_{c2}(0)(1-T)$.[1] It is interesting to emphasize that the Ginzburg-Landau theory was proven to give good qualitative results in mesoscopic superconductors even at low temperature, despite the microscopic derivation of the Ginzburg-Landau equations being valid only for T very close to T_c [38,39]. For better quantitative comparisons at low temperatures, one should employ Boguliobov-deGenes [42–47], Eilenberger [48–52], or recently developed Extended GL model [53].

In this work we solved the TDGL equations for very long cylinders of square cross section and with several lateral sizes, expressed by $L/\xi(0)$, as described in references [26,31]. Those equations were discretized following the link variables method as developed by Gropp and coworkers [40]. It is interesting to emphasize that the TDGL equations, even in their discretized form, are gauge invariant under the transformations $\psi' = \psi e^{i\chi}$, $\mathbf{A}' = \mathbf{A} + \nabla\chi$, $\Phi' = \Phi - \partial\chi/\partial t$, where ψ is the order parameter, $\mathbf{A}$ is the vector potential, Φ is the scalar potential and χ is a scalar function. In this study we chose the zero-scalar potential gauge, that is, $\Phi' = 0$, at all times and positions.

[1] We have chosen the simplest model for the temperature dependence of the physical quantities. Other better choices which are valid for T well below the critical temperature do not invalidate the present investigation, since our main aim is to show that there is a length scale for which we have a meso-to-bulk crossover, no matter what is temperature dependence of $H_{c2}(T)$.

The simulations were carried out for a type II superconductor with $\kappa = 5$, and we focused the analyzes on the Meissner state, i.e., the region of small intensities of magnetic fields which were applied along the cylinder axis. The field was incremented in steps of $\Delta H = 10^{-3}$. Although the TDGL equations can provide all the metastable states of a fixed field, as stressed previously, in the present work we studied only the stationary states. We used the value of $\beta = 1$. This choice has no influence on the final configuration of the stationary state since it affects only the time steps to achieve the steady state [41].

3. Crossover Criteria

In order to facilitate the discussion of our results, in this work we have used the following terminology. First, by *mesoscopic* we mean a superconductor of dimensions such that the vortex lattice is mostly influenced by the geometry of the sample. In addition, in the mixed state, the magnetization is not a smooth function of the applied field; it has a series of jumps which indicate the nucleation of one or more vortices. Second, according to references [26,31], as the size of the sample is increased, there is a length scale above which deep inside the superconductor, the vortex lattice is not perturbed by the surface effects, although they are still present. In this regime, which we denote by *macroscopic*, the vortices are arranged nearly as a triangular lattice, except near the surface where there are some distortions. Also, in the mixed state, the height of the jumps in the magnetization curves are very small so that it approaches to a continuous line. Finally, by *bulk* superconductors we mean those with an infinite size such that the vortex configuration is a perfect triangular lattice through the whole sample. In other words, an ideal superconductor for which all surface effects are suppressed.

Recently, by solving the TDGL equations for many dimensions of a square and many temperatures, the authors of reference [26] developed a work where they built a diagram of the size of square superconducting samples versus the temperature, $L_c(T)$, as shown in the inset of Fig. 1. This diagram delimits two distinct behaviors of type II superconductors, i.e., they have shown the existence of a threshold line between mesoscopic and macroscopic superconducting behaviors. This curve is quite different of the penetration depth of the material, $\lambda(T)$, which is commonly used as the definition for the typical size of mesoscopic samples. Thus, the curve $L_c(T)$ represents the *meso-to-macro crossover*, that is, a length which

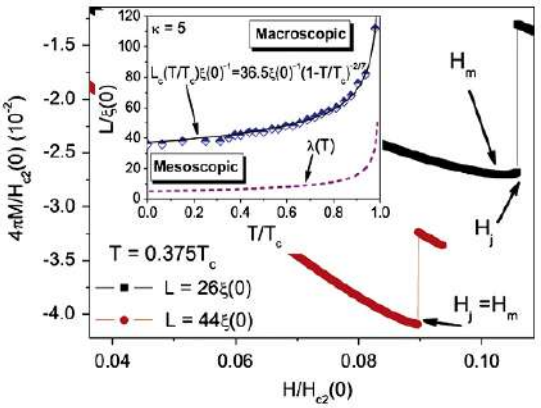

Fig. 1. Magnetization versus applied magnetic field curve for superconducting squares of sizes $L = 26\xi(0)$ and $44\xi(0)$ at $T = 0.375T_c$. As $L/\xi(0)$ increases, H_j and H_m become close one each other and when they are coincident the corresponding size is chosen as the threshold point between meso-to-macro behaviors for such temperature. The inset shows the $L_c(T)/\xi(0)$ diagram in comparison with $\lambda(T)$.

nearly separates the mesoscopic and macroscopic regimes described above. We must stress that this is *not a phase transition*. Instead, it is a smooth change from one regime to another.

The criterion used in ([26,31]) to obtain the meso-to-macro crossover was based on the surface barrier for the first penetration of vortices inside the superconductor. In Fig. 1, we show the magnetization curve $M(H)$ as a function of the applied field H for a superconducting square of sizes $L = 26\xi(0)$ and $L = 44\xi(0)$, and temperature $T = 0.375T_c$. In this figure we indicate the minimum of the magnetization as H_m, and by H_j the field which corresponds to the first nucleation of vortices. We can easily observe that, as $L/\xi(0)$ increases, H_m and H_j become very close to one each other. When we achieve a determined length $L/\xi(0)$ for which these two values of the applied field are equal, within a certain precision, we approach the meso-to-macro crossover. In [26] we explain in more details the physical basis of the criterion. We then repeat the procedure for several temperatures and obtain an $L_c(T)/\xi(0)$ diagram.

In the present work, we will focus on the *macro-to-bulk crossover*. The criterion which we will rely on is the initial slope of the magnetization curve in the Meissner state. In the next section we will describe this criterion in more details. We will see that as $L/\xi(0)$ increases, in the Meissner state, the curve $M(H)$ moves toward the expected bulk line $4\pi M(H) = -H$. Rigorously speaking, we would only achieve the bulk regime for $L = \infty$. Since we are only interested in a crossover, we will relax this criterion and use a slope which is slightly larger than -1, say, -0.999. Of course there is an arbitrariness in this criterion. The best choice of the inclination only could be tested experimentaly, in which the surface effects should be minimally reduced.

4. Results and discussion

We simulated several samples with different lateral sizes for four values of temperature, $T/T_c = 0.0$;0.3125; 0.6500 and 0.8750, where T_c is the critical temperature. As an illustration of the criterion used, in Fig. 2 we show the $M(H)$ curves, normalized by the upper critical field at zero temperature, $H_{c2}(0)$, at $T/T_c = 0.0$ and 0.8750, for several values of $L/\xi(0)$. We can notice that, as the lateral size of the sample increases, the Meissner line moves toward the bulk curve, i.e., $4\pi M = -H$. However, even for $L = 2000\xi(0)$ the curves are not entirely coincident with the bulk one, although are very closed to.

Running the simulations for the entire range of applied field H, until the destruction of superconductivity, becomes unfeasible as L increases. However, since we are interested only in the slope, denoted by $\alpha(L/\xi(0))$, of the $M(H)$ curves for low values of H, only a few values of applied field were sufficient. Therefore, we could run our simulations for sizes until $L = 2000\xi(0)$. In this way we plotted $\alpha(L/\xi(0))$ for the four studied temperatures as shown in the main panel of Fig. 3. Such curves were fitted by the exponential expression, $\alpha(L/\xi(0)) = \alpha_0[(L/\xi(0))^{-n}e^{-L/L_0}] - 1$, where α_0, n and L_0 are adjustable parameters which were maintained free in such process, and the value -1 is the angular coefficient for bulk samples normalized by 4π.

To choose the best parameters to fit the data of Fig. 3, we analyzed the fit quality for several amount of points. To count the number of points, we fixed the last one, i.e., $L/\xi(0) = 2000$, and started from it. Fig. 4 shows the curves of the fit quality for $T/T_c = 0.3125$ and 0.8750 as a function of the number of points used in each fitting process. The adjustable parameters were obtained from the best quality fit point of Fig. 3 and were used to extrapolate the data until we reach the bulk region. Those fitted curves are connecting the data of Fig. 3 and their extrapolation part are shown in the inset of the same figure.

We considered as the criterion for the beginning of the bulk behavior, the point of the fitted curve which reached 0.1% of the value of α predicted for bulk samples, i.e., in our case, -1, as shown in the inset of Fig. 3. By this analyses a diagram of the size of the sample as a function of the temperature, $L_c(T)/\xi(0)$, was built. Such diagram gives us a reference of the threshold between the macroscopic and the bulk behaviors, as shown in Fig. 5. It is worth noticing that by a macroscopic behavior we mean the fact that the Abrikosov vortex lattice is formed in the sample, in contrast with that occurs in the mesoscopic regime [26,31], although the presence of surface superconductivity is still present, as illustrated in the lower inset of Fig. 5. On the other hand, for the macroscopic behavior, we can neglect the surface contribution, as illustrated by the upper inset of Fig. 5. In other words, the vortex configuration in the bulk regime is not influenced by surface for values of L larger than critical length $L_c(T)$.

In references [26,31] we have demonstrated that the meso-to-macro threshold line can be fitted as $L_c(T) = L_c(0)(1 - T/T_c)^{\nu}$, having $L_c(0)$ and ν as fitting parameters. Since we have a few values of $L_c(T)$ we did not attempt to adjust the curve of Fig. 5, although it is very

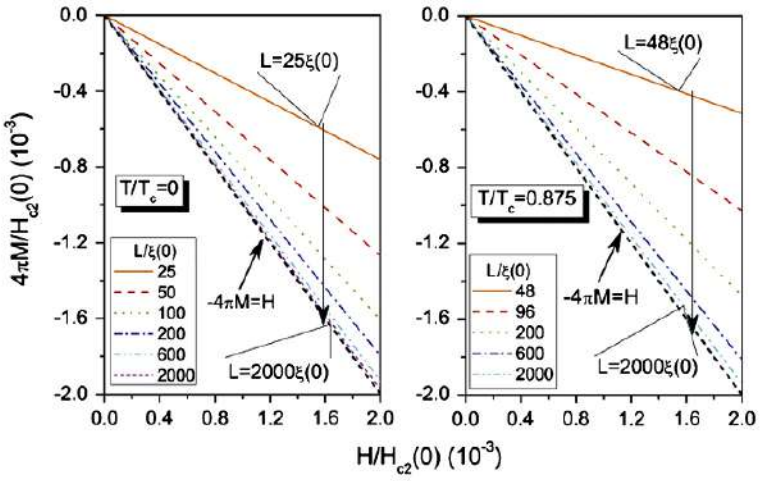

Fig. 2. Magnetization as a function of the applied magnetic field for several values of the samples size for $T/T_c = 0.0$ and 0.8750. We can note that as $L/\xi(0)$ increases, the curves approximate the Meissner line which is predicted for bulk samples.

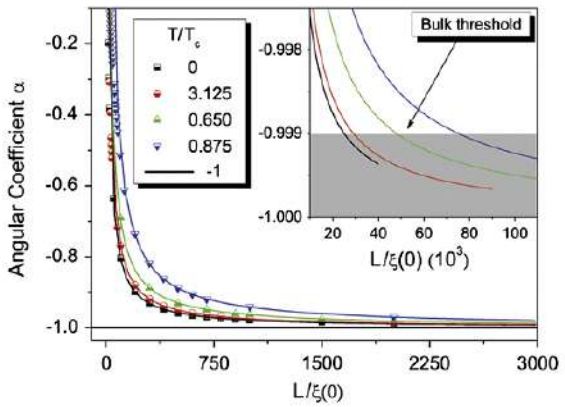

Fig. 3. Angular coefficient of the $M(H)$ curves as a function of the size of the sample for $T/T_c = 0.0$; 0.3125; 0.6500 and *0.8750*. The horizontal line is the angular coefficient of bulk samples. The lines which connect the data were obtained by an exponential expression used to fit each curve.

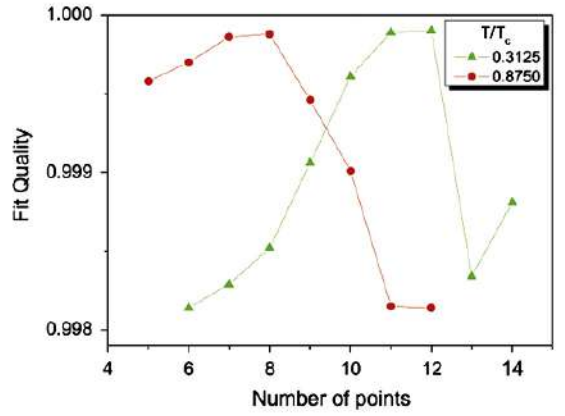

Fig. 4. Fit quality as a function of the number of points considered in the fitting process for $T/T_c = 0.3125$ and *0.8750*. The number of points were counted from the last point of each curve of Fig. 2 which was maintained fixed. The adjustable parameters were chosen from the best quality point.

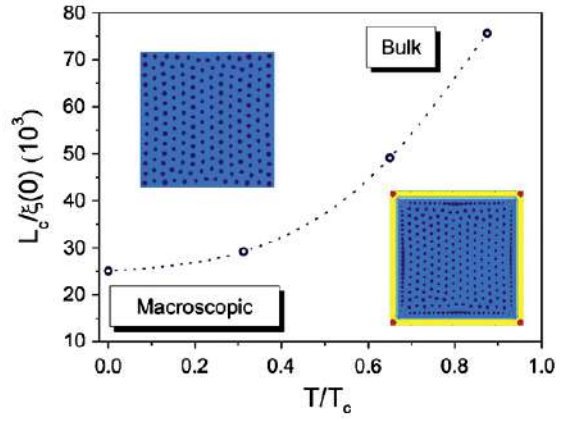

Fig. 5. Sample size versus temperature diagram. The data were obtained from the point of the fitted curve which rich 0.1% of the value of $\varkappa(L/\xi(0))$ predicted for a bulk sample. The upper and lower inset are only representative of the macroscopic and bulk behaviors respectively.

similar to Fig. 7 of ([26]) where we had many more critical points. The difference in both curves is their amplitude, that is, the value of the critical length at zero temperature is very significant. In fact, from Fig. 4 we obtain $L_c(0) = 25{,}105\xi(0)$ for the macro-to-bulk crossover, whereas for the meso-to-macro crossover we have $L_c(0) = 36.5\xi(0)$ (see inset of Fig. 1).

5. Conclusion

We studied the behavior of the characteristic curves of the Meissner state for homogeneous superconducting samples with square geometry. From this investigation we observed that as the lateral size of the samples is increased, the $M(H)$ curves move toward the characteristic Meissner line of bulk materials, i.e., $4\pi M = -H$. Thus, by the study of the angular coefficient of such curves we built a diagram which gives us a reference of the threshold between macroscopic and bulk behaviors. We quote the threshold sizes of $L/\xi(0) = 25{,}105$ and $L/\xi(0) = 75{,}595$ for $T/T_c = 0.0$ and $T/T_c = 0.875$ respectively, as examples.

Acknowledgements

We thank the Brazilian Agencies FAPESP, CAPES and CNPq for financial support.

References

[1] V.A. Schweigert, F.M. Peeters, P. Singha Deo, Phys. Rev. Lett. 81 (1998) 2783.
[2] A.S. Melnikov, I.M. Nefedov, D.A. Ryzhov, I.A. Shereshevskii, V.M. Vinokur, P.P. Vysheslavtsev, Phys. Rev. B 65 (2002) 140503(R).
[3] T. Mertelj, V.V. Kabanov, Phys. Rev. B 67 (2003) 134527.
[4] B.J. Baelus, F.M. Peeters, Phys. Rev. B 65 (2002) 104515.
[5] A.K. Geim, I.V. Grigorieva, S.V. Dubonos, J.G.S. Lok, J.C. Maan, A.E. Filippov, F.M. Peeters, Nature 390 (1997) 259.
[6] L.F. Chibotaru, A. Ceulemans, V. Bruyndoncx, V.V. Moshchalkov, Nature 408 (2000) 833.
[7] E. Sardella, P.N. Lisboa-Filho, C.C. de Souza Silva, L.R.E. Cabral, W.A. Ortiz, Phys. Rev. B 80 (2009) 012506.
[8] E. Sardella, A.L. Malvezzi, P.N. Lisboa-Filho, W.A. Ortiz, Phys. Rev. B 74 (2006) 014512.
[9] I.V. Grigorieva, W. Escoffier, V.R. Misko, B.J. Baelus, F.M. Peeters, L.Y. Vinnikov, S.V. Dubonos, Phys. Rev. Lett. 99 (2007) 147003.
[10] V.V. Moshchalkov, L. Gielen, C. Strunk, R. Jonckheere, X. Qiu, C. Van Haesendonck, Y. Bruynseraede, Nature 373 (1995) 319.
[11] E. Sardella, E.H. Brandt, Supercond. Sci. Technol. 23 (2010) 025015.
[12] M.C.V. Pascolati, E. Sardella, P.N. Lisboa-Filho, Physica C 470 (2010) 206.
[13] S.V. Yampolskii, F.M. Peeters, Phys. Rev. B 62 (2000) 9663.
[14] H.J. Zhao, V.R. Misko, F.M. Peeters, S. Dubonos, V. Oboznov, I.V. Grigorieva, EPL 83 (2008) 17008.
[15] Ben Xu, M.V. Milošević, Shi-Hsin Lin, F.M. Peeters, B. Jankó, Phys. Rev. Lett. 107 (2011) 057002.
[16] T. Cren, L. Serrier-Garcia, F. Debontridder, D. Roditchev, Phys. Rev. Lett. 107 (2011) 097202.
[17] A. Kanda, B.J. Baelus, F.M. Peeters, K. Kadowaki, Y. Ootuka, Phys. Rev. Lett. 93 (2004) 257002.
[18] D.S. Golubovic, M.V. Milošević, F.M. Peeters, V.V. Moshchalkov, Phys. Rev. B 71 (2005) 180502.
[19] B.J. Baelus, A. Kanda, F.M. Peeters, Y. Ootuka, K. Kadowaki, Phys. Rev. B 71 (2005) 140502.
[20] M.V. Milošević, A. Kanda, S. Hatsumi, F.M. Peeters, Y. Ootuka, Phys. Rev. Lett. 103 (2009) 217003.
[21] A.K. Geim, S.V. Dubonos, I.V. Grigorieva, K.S. Novoselov, F.M. Peeters, V.A. Schweigert, Nature 407 (2000) 55.
[22] A.I. Buzdin, J.P. Brison, Phys. Lett. A 196 (1994) 267.
[23] J.J. Palacios, Phys. Rev. Lett. 84 (2000) 1796.
[24] B.J. Baelus, F.M. Peeters, V.A. Schweigert, Phys. Rev. B 63 (2001) 144517.
[25] L.R.E. Cabral, B.J. Baelus, F.M. Peeters, Phys. Rev. B 70 (2004) 144523.
[26] R. Zadorosny, E. Sardella, A.L. Malvezzi, P.N. Lisboa Filho, W.A. Ortiz, Phys. Rev. B 85 (2012) 214511.
[27] V.R. Misko, B. Xu, F.M. Peeters, Phys. Rev. B 76 (2007) 024516.
[28] E. Sardella, P.N. Lisboa-Filho, A.L. Malvezzi, Phys. Rev. B 77 (2008) 104508.
[29] V.R. Misko, B. Xu, F.M. Peeters, Physica C 468 (2008) 726.
[30] H.J. Zhao, V.R. Misko, F.M. Peeters, V. Oboznov, S.V. Dubonos, I.V. Grigorieva, Phys. Rev. B 78 (2008) 104517.
[31] R. Zadorosny, E. Sardella, A.L. Malvezzi, P.N. Lisboa Filho, W.A. Ortiz, Physica C 479 (2012) 154.
[32] G.R. Berdiyorov, A.D. Hernández-Nieves, M.V. Milošević, F.M. Peeters, D. Domínguez, Phys. Rev. B 85 (2012) 092502.

[33] André Müller, Milorad V. Milošević, Sara E.C. Dale, Miles A. Engbarth, Simon J. Bending, Phys. Rev. Lett. 109 (2012) 197003.
[34] M.R. Connolly, M.V. Milošević, S.J. Bending, J.R. Clem, T. Tamegai, EPL 85 (2009) 17008.
[35] V.L. Ginzburg, L. Landau, Zh. Eksp. Teor. Fiz. 20 (1950) 1064.
[36] A. Schmid, Phys. Kondens. Mater. 5 (1966) 302.
[37] Q. Du, M.D. Gunzburger, J.S. Peterson, Phys. Rev. B 46 (1992) 9027.
[38] R. Geurts, M.V. Milošević, F.M. Peeters, Phys. Rev. B 81 (2010) 214514.
[39] M.V. Milošević, R. Geurts, Physica C 470 (2010) 791.
[40] W.D. Gropp, H.G. Kaper, G.K. Leaf, D.M. Levine, M. Palumbo, V.M. Vinokur, J. Comput. Phys. 123 (1996) 254.
[41] G.C. Buscaglia, C. Bolech, A. López, in: Connectivity and Superconductivity, J. Berger and J. Rubinstein (Eds.), Springer, Berlin, 2000.

4.3. Amostras mesoscópicas na presença de gradientes térmicos

Em nossas revisões bibliográficas, não havíamos encontrado nenhum relato na literatura sobre processos de dissipação térmica em supercondutores mesoscópicos. Assim, estudos sobre tal assunto foram incluídos no escopo de projeto de doutorado de um aluno, Elwis C. S. Duarte. Para trabalhar com as equações TDGL, tivemos que explicitar a temperatura na primeira equação. Com isso, estudamos alguns aspectos de um supercondutor sob um gradiente térmico o qual será mostrado na sequência. Um outro trabalho está sendo escrito sobre esse assunto, contudo, o foco será uma forma alternativa de simular amostras que apresentam parâmetros supercondutores que variam com a posição, tal como o estudo feito por Gladilin et al.[4]. Nele, a dinâmica de vórtices de uma amostra do tipo I em forma de cunha foi estudada. Como a profundidade de penetração varia com a espessura da amostra, esse sistema pode, continuamente, passar de um supercondutor do tipo I para um do tipo II. Nosso método usando gradiente térmico é muito mais simples de simular e apresenta resultados semelhantes.

[4] V.N. Gladilin et al., New J. Phys., 17 (2015) 063032

27th International Conference on Low Temperature Physics (LT27) IOP Publishing
Journal of Physics: Conference Series **568** (2014) 022011 doi:10.1088/1742-6596/568/2/022011

Influence of thermal gradient in vortex states of mesoscopic superconductors

E C S Duarte[1], A Presotto[1], D Okimoto[1], E Sardella[2,3], R Zadorosny[1]

[1] Departamento de Física e Química, Univ Estadual Paulista - Unesp, Ilha Solteira, SP, Brazil, CEP 15385-000

[2] UNESP-Universidade Estadual Paulista, Faculdade de Ciências, Departamento de Física, CEP 17033-360, Bauru-SP, Brazil

[3] UNESP-Universidade Estadual Paulista, IPMet-Instituto de Pesquisas Meteorológicas, CEP 17048-699, Bauru-SP, Brazil

E-mail: elwis.gapira@gmail.com

Abstract.

In general, the studies of finite size effects in mesoscopic superconductors have been carried out in such a way that the temperature parameter is constant in the entire system. However, we could have situations where a real sample is near a heater source, as an example. In such situations, gradients of temperature are present. On the other hand, mesoscopic superconductors are interesting systems due to the fact that they present confinement effects which influence all the vortex dynamics. Thus, in this work we studied the influence of thermal gradients on the vortex dynamics in mesoscopic superconductors. For this purposes, we used the time dependent Ginzburg-Landau equations. The thermal gradients produce an asymmetric distribution of the currents around the system which, in turn, yield interesting vortex configurations and difficult the formation of giant vortices.

1. Introduction

The time dependent Ginzburg-Landau (TDGL) theory has been successfully used in the last decades to describe several aspects of mesoscopic superconducting systems. Such systems present small size of the order of penetration depth $\lambda(T)$ and/or the coherence length $\xi(T)$, where T is the temperature. By using the TDGL formalism, several works have demonstrated that the confinement effects induce the formation of multi-vortex (MV) and giant vortex (GV) states [1]-[4]. This depend of the temperature and the system geometry [5]-[11]. Also, the presence of surface defects and De Gennes boundary conditions modify the vortex dynamics of mesoscopic systems [12], in such way that differs from the dynamics presented by the macroscopic ones [13]-[14]. In this work, we study the behavior of the vortex dynamics in mesoscopic systems in the presence of linear thermal gradients. Then, we analyze their magnetic properties, the vortex configurations, and the possible formation of a GV state.

2. Theoretical formalism

The formalism which we used was firstly proposed by Schimid[15], and it is a generalization of the Ginzburg-Landau (GL) equations, where a temporal evolution of the order parameter ψ

27th International Conference on Low Temperature Physics (LT27) IOP Publishing
Journal of Physics: Conference Series **568** (2014) 022011 doi:10.1088/1742-6596/568/2/022011

and the potential vector $\mathbf{A}$ was inserted; $|\psi|^2$ is the density of superelectrons and the induction magnet field is given by $\mathbf{B} = \nabla \times \mathbf{A}$. In dimensionless units, the TDGL equations are given by

$$\frac{\partial \psi}{\partial t} + \imath\varphi\psi = (-i\boldsymbol{\nabla} - \mathbf{A})^2\psi + \psi(1 - T(x) - |\psi|^2) \,, \tag{1}$$

$$\beta\frac{\partial \mathbf{A}}{\partial t} + \boldsymbol{\nabla}\varphi = \mathbf{J_S} - \kappa^2\boldsymbol{\nabla} \times \boldsymbol{\nabla} \times \mathbf{A} \,, \tag{2}$$

where de superconductivity current density is given by

$$\mathbf{J_S} = \mathrm{Re}(\psi^*(-\imath\nabla - \mathbf{A})\psi) \,. \tag{3}$$

For the thermal gradient we assumed a linear dependence of T along the x axis which is given by

$$T(x) = T_l + \frac{T_r - T_l}{a}x \,, \tag{4}$$

where T_r and T_l are the temperatures at the right-hand (hottest) and left-hand (coldest) side of the superconducting square. All equations have been normalized. The distances are in units of the coherence length $\xi(0)$; the magnetic field in units of the bulk upper critical field $H_{c2}(0)$ and the temperature in units of the critical temperature T_c; $\kappa = \lambda(T)/\xi(T)$ is the GL parameter. The TDGL equations are gauge invariant under the transformations: $\psi' = \psi e^{i\chi}$, $\mathbf{A}' = \mathbf{A} + \nabla\chi$, $\varphi' = \varphi - \frac{\partial\chi}{\partial t}$. We have worked in the Coulomb gauge where $\varphi' = 0$ for all times and positions. We numerically solved such equations by using the link variable method [16]. This method is preferably used because it preserves the gauge invariance of the equations once they are discretized. The TDGL equations will be used only as a relaxation method to obtain the steady state, that is, we are solely interested in the equilibrium vortex configurations.

3. Results and Discussion

We carried out the numerical simulations considering square systems with lateral size of $12\xi(0)$ and GL parameter $\kappa = 5$, which is equivalent to a Pb-In alloy[17]. We also used the following simulation parameters: $\beta = 1$; the size of the mesh was taken as $\Delta x = \Delta y = 0.125\xi(0)$ and the steps of the external magnetic field $\Delta H = 10^{-3}$. All the dynamics were analyzed under a thermal gradient which changes the value of ψ along the x axis of the system. In this work, we investigated the dynamics of two systems under two different thermal gradients, i.e, one in which the temperature varies from $0.7T_c$ to $0.9T_c$, label by S_1 and another one from $0.8T_c$ to $0.85T_c$, labeled by S_2. We also compared the results with a system at a homogeneous temperature (HT for brief) distribution by taking $T = 0.85T_c$. In Fig. 1 we present the magnetization curve as a function of the applied magnetic field of the systems under investigation. The behavior of such curves are similar to those ones exhibited by the HT systems, i.e., each discontinuity is due to one or more vortex penetration. Note that, the field corresponding to the first penetration for the S_1 system is lower than for the S_2 one. This is due to the fact that S_1 has its right-hand side hotter than S_2 which, on its turn, has a similar behavior presented by the HT system. The field sufficient for the destruction of superconductivity is higher for S_1 than for S_2 because temperature in the colder region is lower for the former system. In Fig. 2 we illustrate the profile of the modulus the current density, J/J_0, where J_0 is the despairing current, along the x axis and for three different distances w from the bottom side of the system (see inset of Fig. 1). A comparison between S_1 and S_2 is showed in Fig. 2. It is worth noticing the asymmetric distribution of J in comparison with the inset of this same figure for the HT system. However, S_2 presents a less asymmetric profile when it is compared with S_1. Also, it can be observed that J presents a higher value in the colder region and a degradation of superconductivity in the hottest one. We notice that with both perturbations S_1 and S_2 the vortices nucleate inside

27th International Conference on Low Temperature Physics (LT27) IOP Publishing
Journal of Physics: Conference Series **568** (2014) 022011 doi:10.1088/1742-6596/568/2/022011

the superconductor one by one. As expected, the penetration always occurs at the right-hand side of the system.

We also studied the influence of non-homogeneous distribution of temperature on the giant vortex state which has been found for the HT systems [18]. In Fig. 3 we show two vortex state for S_1, S_2 and HT. In the panel 3(a) it is shown the intensity of $|\psi|$ superimposed by the streamlines $\mathbf{J}$. In such figure is clearly seen two separate vortices which is confirmed by the phase of ψ in panel 3(b). The other hand, the equivalent panels 3(c) and (d) for S_2, and 3(e) and (f) for the HT system, we clearly see the formation of giant vortex state. As a consequence, we can say that a rather non-homogeneous temperature like S_2 is not sufficient to avoid the nucleation of such state.

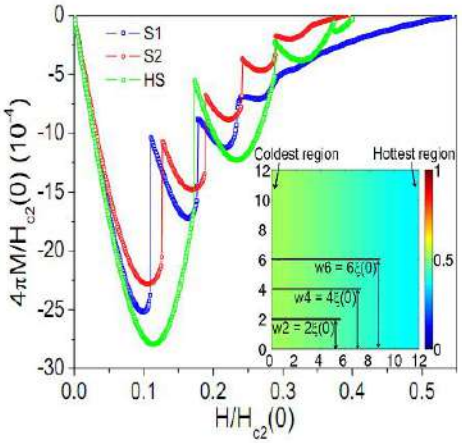

Figure 1. The magnetization curve as a function of the external applied field for the S_1, S_3 and HT systems. The inset shows the intensity of the order parameter in the initial state (without applied magnet field) under a thermal gradient.

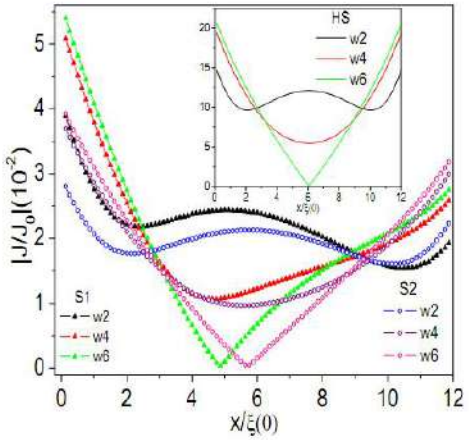

Figure 2. Profile of the modulus of the current along the x axis for three different levels of the square shown in the inset of Fig. 1 for S_1 and S_2. In the inset of the present figure it is shown the symmetric profile of the current for the HT system.

Fig. 4 illustrate the scenario associated with the third penetration. S_1 and S_2 present the same penetration dynamics with three nucleated vortices in the stationary state. However, the HT system presents four vortex state just after the third penetration (see panels 4(e) and (f)). This indicates that the thermal gradient breaks the fourfold symmetry of the multi-vortex state in those systems. On the other hand, it is interesting to note that giant vortex is created in S_1, which means that a greater variation of the temperature induces a non-conventional vortex interaction.

4. Conclusion

In this work we studied two systems with different thermal gradients by using the time dependent Ginzburg-Landau equations. It was shown that a variation of the temperature induces an asymmetric distribution of $\mathbf{J}$ along the system which is responsible for non-conventional behavior of the vortex dynamics. Depending on the conditions, such the range of variation of T and the number of penetrated vortices, giant vortex states can be avoided. Another interesting behavior is the break of the fourfold symmetric of the third penetration presented by the systems with thermal gradients in comparison with a system in a uniform temperature.

27th International Conference on Low Temperature Physics (LT27) IOP Publishing
Journal of Physics: Conference Series **568** (2014) 022011 doi:10.1088/1742-6596/568/2/022011

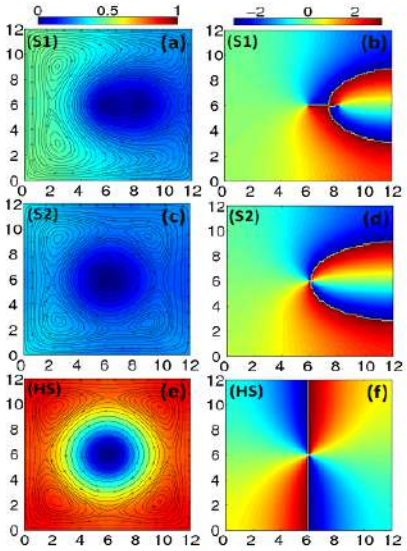

Figure 3. Left: intensity of the order parameter; right: phase of the order parameter; S_1 (a,b); S_2 (c,d); HT (e,f).

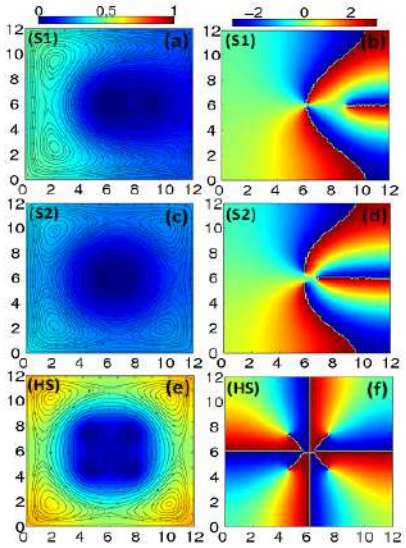

Figure 4. The same as for Fig. 3; S_1 (a,b); S_2 (c,d); HT (e,f).

5. Acknowledgments

We thank the Brazilian Agencies Fundunesp/PROPe grant 2115/002/14-PROPe/CDC and the São Paulo Research Foundation (FAPESP), grants 2013/17719-8 and 2012/04388-0 for financial support.

6. References

[1] Machida M, Kaburaki, H 1993 *Phys.Rev.Lett* **71** 3206–3209
[2] Bolech A C, Buscaglia G C, Lopez A, 1995 *Phys.Rev.B* **52** 15719–15722
[3] Deo P S, Schweigert V A, Peeters F M, Geim A K 1997 *Phys.Rev.Lett* **79** 4653–4657
[4] Schweigert V A, Peeters F M 1998 *Phys.Rev.B* **57** 13817
[5] Schweigert V A, Peeters F M 1999 *Phys.Rev.B* **60** 3084–3087
[6] Cren T, Garcia L S, Debontridder F, Roditchev D 2011 *Phys.Rev.Lett* **107** 097202
[7] Baelus B J, Kanda A, Peeters F M, Ootuka Y, Kadowaki K 2005 *Phys.Rev.B* **71** 140502
[8] Sardella E, Lisboa-Filho P N, Malvezzi A L 2008 *Phys.Rev.B* **77** 104508
[9] Presotto A, Sardella E, Zadorosny R 2013 *Physica C* **492** 75–79
[10] Palacios J J 1998 *Phys.Rev.B* **58** R5948-R5951
[11] Zadorosny R, Sardella E, Malvezzi A L, Lisboa-Filho P N, Ortiz W A 2012 *Phys.Rev.B* **85** 214511
[12] Barba-Ortega J, Gonzlez J D, Sardella E 2014 *J.Low.Temp.Phys* **174** 96–103
[13] Barba-Ortega J, Sardella E, Aguiar J A, Brant E H 2012 *Physica C* **479** 49–52
[14] Connolly M R, Milosevic M V, Bending S J, Clem J R, Tamegai T 2009 *Euro.Phys.Lett* **85** 17008
[15] Schimid A 1966 *Phys.Kondens.Materie* **5** 302–317
[16] Gropp W D, Kaper H G, Leaf G K, Levine D M, Palumbo M, Vinokur V M 1996 *J.Comput.Phys* **123** 254–266
[17] Poole Jr C P, Farach H A, Creswick R J, Prozorov Ruslan 2007 *Superconductivity* 2.ed (Amsterdam: Elsevier) p 670
[18] Sardella E, Malvezzi A L, Lisboa-Filho P N, Ortiz W A 2006 *Phys.Rev.B* **74** 014512

4.4. Aniquilação de vórtice e antivórtice de Abrikosov

Vórtices (Vs) e antivórtices (AVs) magnéticos (aqui chamados de Abrikosov) podem ser criados de forma a conviverem no supercondutor sob as mesmas condições aplicando um campo magnético externo cíclico. Esse espécimes se atraem e, dependendo de parâmetros como temperatura e tamanho da amostra, o V e o AV podem se aniquilar na região supercondutora entre o buraco e a borda externa. Além disso, o movimento dos V e AV é dissipativo, aumentando localmente a temperatura da amostra. Dessa forma, estudamos os parâmetros para a aniquilação ocorrer no mar supercondutor e os processos dissipativos envolvidos nesse evento. A forma de incluir dissipação de energia e difusão térmica nas equações TDGL serão mostrados na próxima seção.

IOP Publishing Journal of Physics: Condensed Matter
J. Phys.: Condens. Matter 29 (2017) 405605 (9pp) https://doi.org/10.1088/1361-648X/aa81e6

Dynamics and heat diffusion of Abrikosov's vortex-antivortex pairs during an annihilation process

E C S Duarte[1], E Sardella[2], W A Ortiz[3] and R Zadorosny[1]

[1] Departamento de Física e Química, Universidade Estadual Paulista (UNESP), Faculdade de Engenharia de Ilha Solteira, Caixa Postal 31, 15385-000 Ilha Solteira-SP, Brazil
[2] Departamento de Física, Universidade Estadual Paulista (UNESP), Faculdade de Ciências, Caixa Postal 473, 17033-360, Bauru-SP, Brazil
[3] Departamento de Física, Universidade Federal de São Carlos—UFSCar, 13565-905, São Carlos-SP, Brazil

E-mail: rafazad@gmail.com

Received 2 March 2017, revised 18 July 2017
Accepted for publication 25 July 2017
Published 4 September 2017

Abstract

The manipulation and control of vortex states in superconducting systems are of great interest in view of possible applications, for which mesoscopic materials are good candidates. In this work, we studied the annihilation dynamics and the dissipative aspects of an Abrikosov's vortex-antivortex pair in a mesoscopic superconducting system with a concentric hole. The generalized time-dependent Ginzburg–Landau equations were numerically solved. The main result is the appearance of a phase slip-like line due to the elongation of the vortex and antivortex cores. Under specific circumstances, thermal dissipation might be associated with a sizeable relaxation of the order parameter, so that the energy released in the annihilation of a vortex-antivortex pair might become detectable in measurements of the magnetization as a function of time.

Keywords: vortex dynamics, TDGL, annihilation, heat diffusion, energy dissipation

(Some figures may appear in colour only in the online journal)

1. Introduction

The study of vortex matter is an issue of greatest interest, since the comprehension and manipulation of the vortex motion are very important for possible applications as in the case of control of spins by vortices [1–3]. However, unusual behaviors appear when the vortices are subjected to an environment where the confinement effects emerge, as is the case of mesoscopic systems. As an example, we cite the formation of multivortex states, where one has coexistence of single and giant vortices[4]. In mesoscopic systems, this state tends to follow the geometry of the sample [4–12]. Also, due to interactions between vortices and the shielding currents, the formation of a giant vortex is conceivable under certain circumstances. In this case, the cores of individual vortices collapse into a single entity with vorticity greater than one [13–17].

On the other hand, under specific conditions, it is possible that a vortex-antivortex pair (V–AV) becomes stable. Such stability has a close correspondence with the symmetry of the system, e.g. it is possible to stabilize a state with vorticity 3 in a square system by 4 vortices located near the vertices and an antivortex in the center of the square [18]. The V–AV dynamics was also studied in systems with holes [19–21], magnetic dots [22–25] and arrays of small current loops [26].

The V and AV can be spontaneously formed after a quench caused by, e.g. a hot spot [27, 28]. In this scenario, as the heat is diffused and depending on the velocity of such diffusion, the vortices are arranged in a cluster or in a metastable ring-like configuration [27]. In a ring superconductor, just after a quench, there is no interaction of the Vs and the

[4] A giant vortex is a multiquanta vortex with a single core.

AVs with the defects and annihilations occur. After such a period of time, some Vs and AVs leave the sample or are trapped in the ring's hole, which generates a magnetic flux inside the hole [28].

In [29, 30], the nucleation and penetration of vortices were studied in very thin films and wires under applied currents and magnetic fields. In such cases, the vortices penetrate the samples forming a chain in the thin films and helicoidal lines in the wires [29]. It was also shown that the normal state penetrates the superconductor like macroscopic droplets which in the presence of defects evolve to single vortices [30].

Samples with a V–AV state were also studied by Berdiyorov and coworkers [31]. They analyzed the V–AV dynamics in a thin stripe with electric contacts where a current was injected. In this system a phase slip line is formed and the annihilation of V and AV depends on the intensity of the applied current. This annihilation process produces an oscillating voltage over the contacts in a terahertz frequency [31]. In this sense, it is interesting to mention the work of Gulevich and Kusmartsev [32] who proposed a device based on a long annular Josephson junction where the creation, annihilation and trapping of flux and antiflux take place. The authors claim that their device is very sensitive and could become a detector of microwave radiation and magnetic fields.

In [20], Sardella and coworkers, analyzed the annihilation of a V–AV pair in a square mesoscopic system with a concentric square hole. As a result, it was shown that, when the vortex is entering the system, its average velocity is of the order of 10^3 m s^{-1} and, during the annihilation motion, due to the mutual attraction between the V and the AV, its average velocity reaches values of the order of 10^5 m s^{-1}. Recently, Zadorosny *et al* [21] studied similar systems and have shown that the V–AV pair acquires an elongated shape which creates a channel between the border of the system and the hole. In the analysis of the V–AV pair motion it was also shown that such specimens acquire an acceleration in the early and final stages of the annihilation process, with a nearly constant velocity motion between these stages.

In practice, mesoscopic superconducting materials have been applied in devices like amplifiers [33], imaging of single magnetic flux quantum (single vortex) [34], single electron [35] and single photon [36–39] detectors, and the knowledge of the V–AV dynamics in such materials is of great importance to improve specific characteristics to those applications.

In this work we studied the annihilation process between a vortex and an antivortex in mesoscopic superconducting square systems with a concentric square hole. The study is focused on a systematic analysis of the parameters for which the annihilation process occurs in the superconducting region. Attention is also given to the total energy released in such a collision. Our results indicate that the energy generated in such process can be associated to frequencies in the infrared spectrum and also that smaller systems present the higher energies. We speculate that such system could be the heart of a future device for detection of electromagnetic waves in the appropriate frequency range.

This work is organized as follows. In section 2 we briefly delineate the theoretical formalism used to simulate the mesoscopic systems. In section 3 we present the results obtained from the simulations and, subsequently, discuss them. In section 4, we present our conclusions.

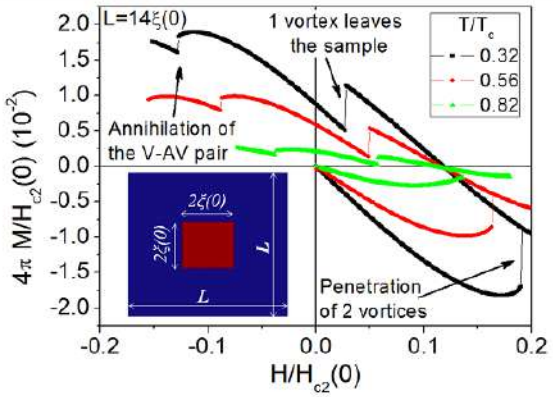

Figure 1. Magnetization as a function of the applied magnetic field for the $L = 14\xi(0)$ system. In such sample, two vortices are nucleated in the first penetration. In the decreasing field branch, one vortex is untrapped and leaves the sample and in the branch of negative fields the annihilation of the V–AV pair takes place. The inset shows an illustration of the simulated system.

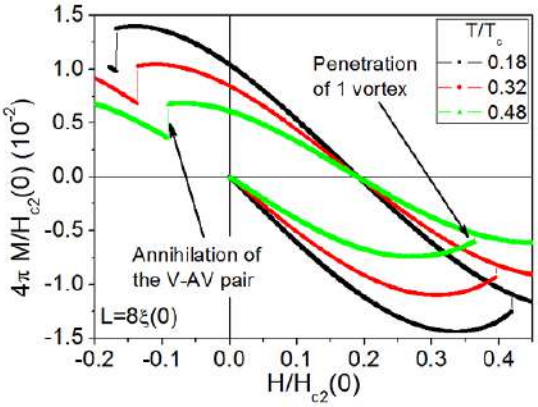

Figure 2. Magnetization as a function of the applied magnetic field for the $L = 8\xi(0)$ system. In such sample, only one vortex is nucleated in the first penetration and the annihilation of the V–AV pair takes place in the branch of negative fields.

2. Theoretical formalism

The time-dependent approach for the Ginzburg–Landau equations, proposed by Schmid [40], provides a temporal evolution of the order parameter ψ and the vector potential $\mathbf{A}$ for a superconducting material submitted to an external applied magnetic field and/or a transport current. Such approach is appropriate to describe most phenomena which occur in the resistive state. For our purposes, it will be important to use the equations for the energy dissipated due to both the induced electrical field and the relaxation of ψ during the vortex motion. It is worth to mention that this theoretical framework has a satisfactory agreement with experiments at temperatures

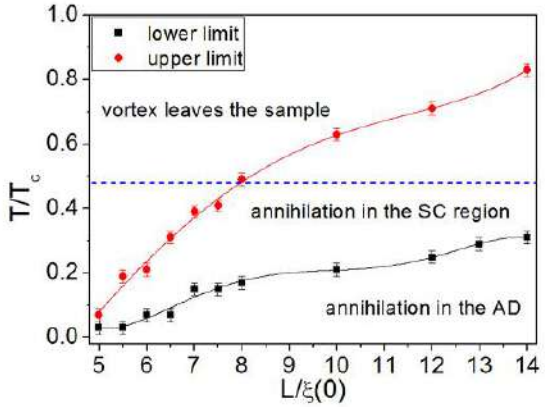

Figure 3. The $T(L)$ diagram indicating the domains for which the annihilation of a V–AV pair occurs in the superconducting region. The lines which links the points are only a guide for the eyes. The dashed line indicates the temperature, i.e. $T = 0.48T_c$, for which we analyzed the dynamics of the simulated systems.

larger than $T = 0.5T_c$ [40, 41] however, qualitatively explains the dynamics at lower temperatures. Those equations have also been applied in studies with induced voltage [42], magnetoresistance [43, 44] and the application of alternating external magnetic fields [45]. The equations proposed by Schmid were extended for gap superconductors by Kramer and Watts-Tobin [46]. Thus, the generalized time-dependent Ginzburg–Landau (GTDGL) equations take the form:

$$\frac{u}{\sqrt{1+\gamma^2|\psi|^2}}\left(\frac{\partial}{\partial t}+\frac{\gamma^2}{2}\frac{\partial|\psi|^2}{\partial t}+\mathrm{i}\varphi\right)\psi = -(-\mathrm{i}\nabla-\mathbf{A})^2\psi+\psi(1-T-|\psi|^2), \tag{1}$$

$$\left(\frac{\partial\mathbf{A}}{\partial t}+\nabla\varphi\right) = \mathbf{J}_s-\kappa^2\nabla\times\nabla\times\mathbf{A}, \tag{2}$$

where the superconducting current density is given by:

$$\mathbf{J}_s = \mathrm{Re}\left[\bar{\psi}(-\mathrm{i}\nabla-\mathbf{A})\psi\right]. \tag{3}$$

Here, the distances are in units of the coherence length at zero temperature $\xi(0)$, the magnetic field is in units of the bulk upper critical field $H_{c2}(0)$, the temperature is in units of T_c, time is in units of $t_{GL}(0) = \pi\hbar/8k_bT_cu$, the Ginzburg–Landau time, $\mathbf{A}$ is in units of $H_{c2}(0)\xi(0)$, φ is the scalar potential and is in units of $\hbar/2et_{GL}(0)$, $\kappa = \lambda(0)/\xi(0)$ is the Ginzburg–Landau parameter, where $\lambda(0)$ is the London penetration length at zero temperature, and the order parameter is in units of α_0T_c/β, where α_0 and β are the phenomenological Ginzburg–Landau parameters [20]. The parameter u is related to the relaxation of ψ [47] and is very important in studies with dissipative mechanisms; u is extracted from a microscopic derivation of the Ginzburg–Landau equations using the Gor'kov approach [48, 49]. Frequently, $u = 5.79$ is adopted, as determined by first principle in [46]. In such formulation the inelastic phonon-electron scattering time, t_e, is taken into account and $\gamma = 2t_e\psi_0/\hbar$. The GTDGL equations were

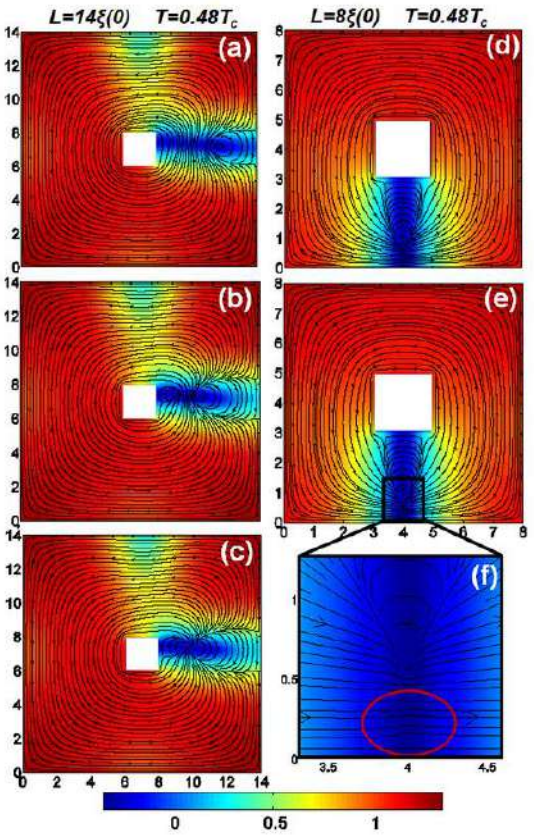

Figure 4. Intensity of $|\psi|$ during the annihilation process at $T = 0.48T_c$. The black lines indicate the superconducting currents flowing around the system. From panel (a) to (c), it shows the dynamics for $L = 14\xi(0)$: in (a) an AV penetrates the system with a V trapped in the hole; (b) the vortex leaves the hole and in (c) it is shown the overlap of the currents during the annihilation. From panel (d) to (f), it is shown the dynamics for $L = 8\xi(0)$. It is worth to note that in this case the dynamics occurred near the upper threshold line shown in figure 3. In (d) the V moves toward the border of the system; in (e) an AV starts to penetrate the system and (f) is a zoom showing the distortion of the currents due to the nucleation of an AV. It is also shown that the currents circumvents the vortex and/or the antivortex in such a way it forms a cone-like profile.

numerically solved by using the link-variable method [50, 51] which ensures the gauge invariance under the transformations $\psi' = \psi e^{i\chi}$, $\mathbf{A}' = \mathbf{A}+\nabla\chi$, $\varphi' = \varphi-\partial\chi/\partial t$, when they are discretized in a numerical grid [52]. Therefore, for all times and positions we have chosen $\varphi' = 0$, since neither charges nor external currents are considered in this work. The equation for the dissipated power energy was obtained by using the Helmholtz free energy theorem for a superconductor in an external magnetic field [40, 45]. Such equation, in dimensionless form, is given by:

$$W_{total} = 2\left(\frac{\partial\mathbf{A}}{\partial t}\right)^2+\frac{2u}{\sqrt{1+\gamma^2|\psi|^2}}\left[\left(\left|\frac{\partial\psi}{\partial t}\right|\right)^2+\frac{\gamma^2}{4}\left(\frac{\partial|\psi|^2}{\partial t}\right)^2\right]. \tag{4}$$

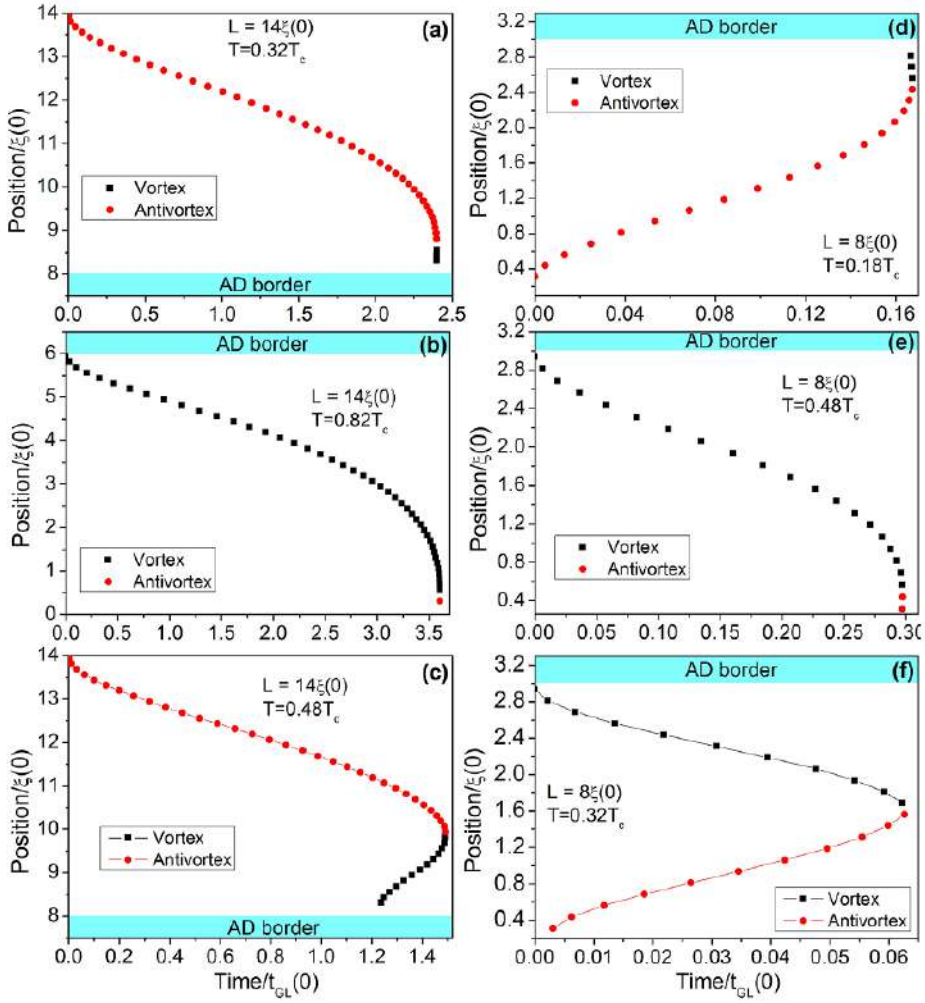

Figure 5. Position as a function of time in temperatures near the lower and upper threshold line of figure 3. (a) $T = 0.32T_c$, (b) $T = 0.82T_c$ for $L = 14\xi(0)$ system and (d) $T = 0.18T_c$, (e) $T = 0.48T_c$, for $L = 8\xi(0)$. (c) $0.48T_c$ and (f) $0.32T_c$ show the motion of the pair for an intermediate temperature for the systems $L = 14\xi(0)$ and $L = 8\xi(0)$, respectively.

The first term is the dissipation due to the induced electrical field, W_A, and the second one is due to the dissipation related to the relaxation of the order parameter, W_ψ. The dissipated power energy is given in units of $H_{c2}^2(0)/[8\pi\kappa^2 t_{GL}(0)]$. As W_{total} diffuses through the system, we couple the thermal diffusion equation to the GTDGL ones. By using the approach of [42], the dimensionless form of the thermal equation can be written as:

$$C'_{eff}\frac{\partial T}{\partial t} = K_{eff}\,\nabla^2 T + \frac{1}{2}W_{total} - \eta(T - T_0). \qquad (5)$$

Here, η is the heat transfer coefficient of the substrate, $C'_{eff} = \pi^4/48u$ is the effective heat capacity, and $K_{eff} = \pi^4/48u^2$ is the effective thermal conductivity.

In the first part of this work, as we do not take into account dissipative effects, we set $u = 1$ and $\gamma = 0$ in equation 1. Such procedure is still well accepted in the literature [43] due to the good qualitative description of experimental data [53–55] and facilitated computations [20]. In the second part of the study, where the thermal dissipation and diffusion need to be properly taken into account, $u = 5.79$ and $\gamma = 10$ were used.

3. Results and discussion

We divide the discussion into two distinct scenarios. First, we consider the temperature constant throughout the system. And second, we take into account the heat diffusion produced by the V–AV collision.

3.1. Constant temperature

The simulations of the annihilation dynamics were carried out by adopting $u = 1$ and $\kappa = 5$. The value for κ is equivalent to those of some low critical temperature superconductors, such as the metallic alloy Pb–In [56]. The systems were simulated

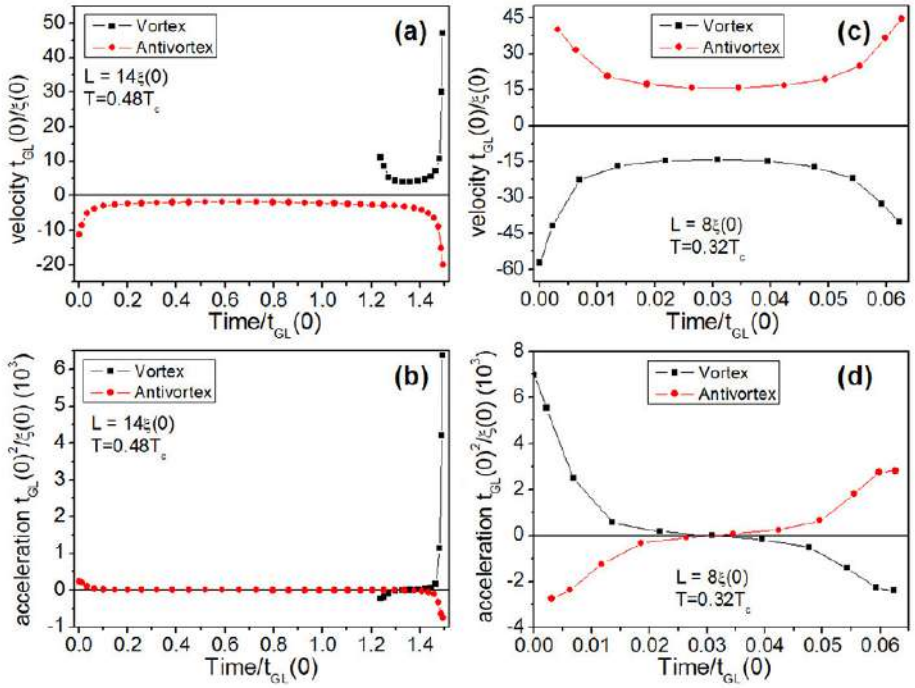

Figure 6. Velocities and accelerations of the vortex and antivortex motion for the $L = 14\xi(0)$ and $L = 8\xi(0)$ systems.

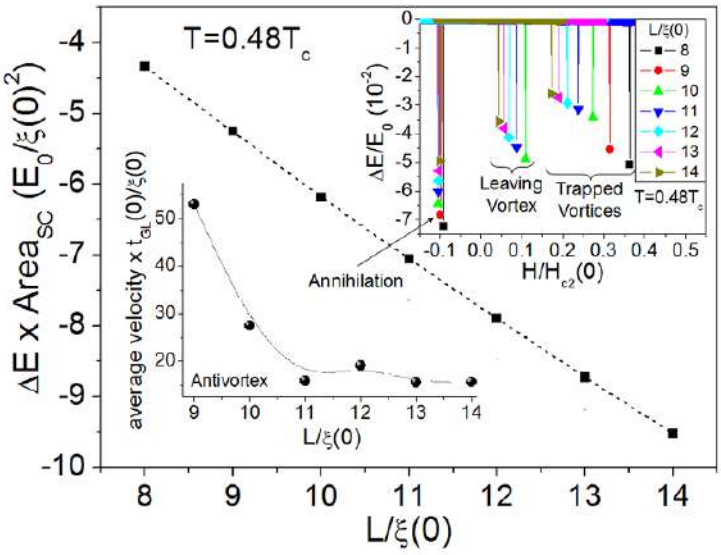

Figure 7. The main curve shows the variation of the normalized superconducting energy × the normalized superconducting area as a function of the lateral size of the system. The ΔE was calculated as the difference between the superconducting energy immediately before and just after the annihilation. The energy minimized in the annihilation process decreases as the size of the sample is increased. The upper inset shows ΔE as a function of the applied magnetic field for several systems at $T = 0.48T_c$. In the range $0.15 < H/H_{c2} < 0.4$ the vortices are trapped in the hole; for $0 < H/H_{c2} < 0.14$ one of the vortices is untrapped and leaves the sample. The dips around $H = -0.1H_{c2}$ occurs as the minimization of the energy after the annihilation. The lower inset shows the average velocity as a function of the lateral size of the systems. A quasi-phase slip line is formed in smaller systems as a consequence of the size effect. In such degraded region, the V–AV pair moves faster than in larger systems where the degradation does not take all the superconducting track.

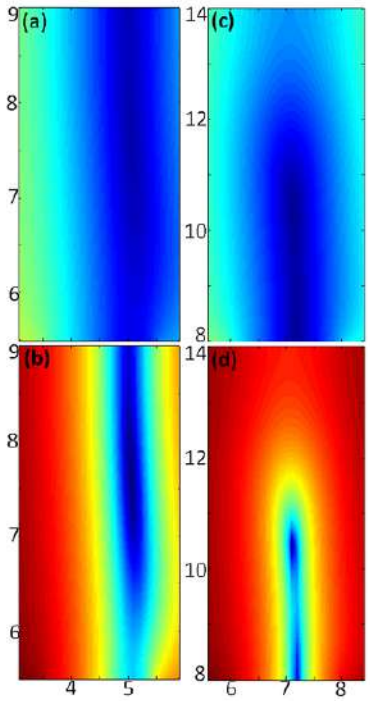

Figure 8. Upper panels: intensity of the order parameter, $|\psi|$; lower panels: for a better visualizing of the degraded superconducting region, we show $\log|\psi|$. In (a) and (b) we show the snapshots for the $L = 9\xi(0)$ system. From these panels, it can be clearly seen that no preserved superconducting region remains, once the values of v_{avg} are very large. On the other hand, for the $L = 14\xi(0)$ system is visible in both images (panels (c) and (d)) that there is still a superconducting region which is not entirely degraded. All snapshots were taken at the instant just before the annihilation of the V–AV pair.

with a concentric square hole of side $l = 2\xi(0)$, as shown in the inset of figure 1. For each system, the external magnetic field was varied in steps of $\Delta H = 10^{-3}H_{c2}(0)$ and the temperature in steps of $\Delta T = 0.2T_c$.

Figure 1 shows the magnetization versus applied magnetic field, $M(H)$ curves for the system with $L = 14\xi(0)$ at different temperatures. In this case, two vortices nucleate into the sample being trapped by the hole. As H is decreased, one vortex leaves the system and, when the field is inverted, an AV penetrates the sample while a vortex remains trapped in the hole. Thus, a V–AV pair is formed and each specimen moves toward each other until their mutual annihilation. The same process occurs in smaller systems as can be seen in figure 2 for a system with $L = 8\xi(0)$. The main difference is that in the first penetration only one vortex is nucleated and trapped by the hole. It is interesting to note that the annihilation process was detected even in systems with an effective superconducting region smaller than the size of a vortex core, i.e. smaller than $2\xi(0)$. Our simulations show that, in this case, both V and AV elongate to accommodate themselves into the superconducting material, so that the cores run against each other in a straight track, resembling a phase slip line, even though the order parameter is not exactly zero along this line. This aspect will be further discussed ahead in this paper.

In order to determine the parameters, such as the range of temperatures and the lateral sizes of the system, for which the annihilation process takes place in the superconducting region, a $T(L)$ diagram was built and the result is shown in figure 3. As described in this figure, below the line characterized by square symbols, namely, the lower limit, when H is inverted, the V remains trapped in the hole. Then, an AV penetrates the system and moves toward the center of the sample. The penetrated AV and the trapped flux interact attractively, what causes an acceleration of the AV, which falls in the hole and cancels the flux which was already inside. On the other hand, above the upper limit (circles), when H is inverted, the V is untrapped and leaves the sample before the nucleation of an AV. In between such lines, the annihilation of the V–AV pair occurs in the superconducting region.

The horizontal line in figure 3 indicates the isothermal where annihilation dynamics were analyzed. In figure 4 we exhibit some images of the intensity of $|\psi|$ which summarize the annihilation process for systems with two distinct sizes, i.e. $L = 14\xi(0)$—figures 4(a)–(c)—and $L = 8\xi(0)$—(d) to (f)—at $T = 0.48T_c$.

One can notice that in both systems a quasi phase slip line is formed[5]. Such region appears due to the attraction between the vortex and the antivortex which causes an elongation of their cores [21]. After the annihilation, such line disappears. In small systems, the hole and the border of the sample are so close that the distortion of the vortex and the antivortex, which occurs during their encounter, is sufficient to create such a quasi phase slip line. Figure 4 shows the intensity plot of $|\psi|$ and the black lines indicate the shielding currents. We can also notice that for both systems a visible structure is formed by the currents, which is originated in the drag motion of the V–AV pair. In figure 4(f), one of the borders of that system is zoomed up. We can see the distortion of the shielding current caused by the nucleation of an AV. To study the dynamics of the V–AV motion, in figure 5 we plotted the time evolution of the position of those specimens. The evolution of the $L = 14\xi(0)$ system is depicted in panels figures 5(a)–(c) for three distinct temperatures: in panel (a) it is basically shown the motion of the AV which annihilates the vortex near the hole in the vicinity of the lower limit $T = 0.32T_c$ of the phase diagram of figure 3; in panel (b) we show the vortex motion near the upper limit line $T = 0.82T_c$ where the annihilation occurs near the border; and finally in panel (c) the motion of an intermediate temperature is shown. The same evolution is illustrated in panels 5(d)–(f) for the $L = 8\xi(0)$ system at $T = 0.18T_c$, $0.48T_c$, and $0.32T_c$, respectively.

By calculating the derivatives of the curves from figure 5 (panels (c) and (f)) we obtained the velocity and the acceleration of the V–AV pair (see figure 6). It becomes evident that the motion of the pair is accelerated. The amplitude of the average velocity of the AV, as an example, decays and reaches a nearly constant value as the size of the system is increased,

[5] A phase slip line is a line along which the order parameter vanishes. This is clearly not the case in the present scenario. However, we can see that the order parameter is very small in a quite elongated region. It is in this sense that we use the denomination *quasi phase slip line*.

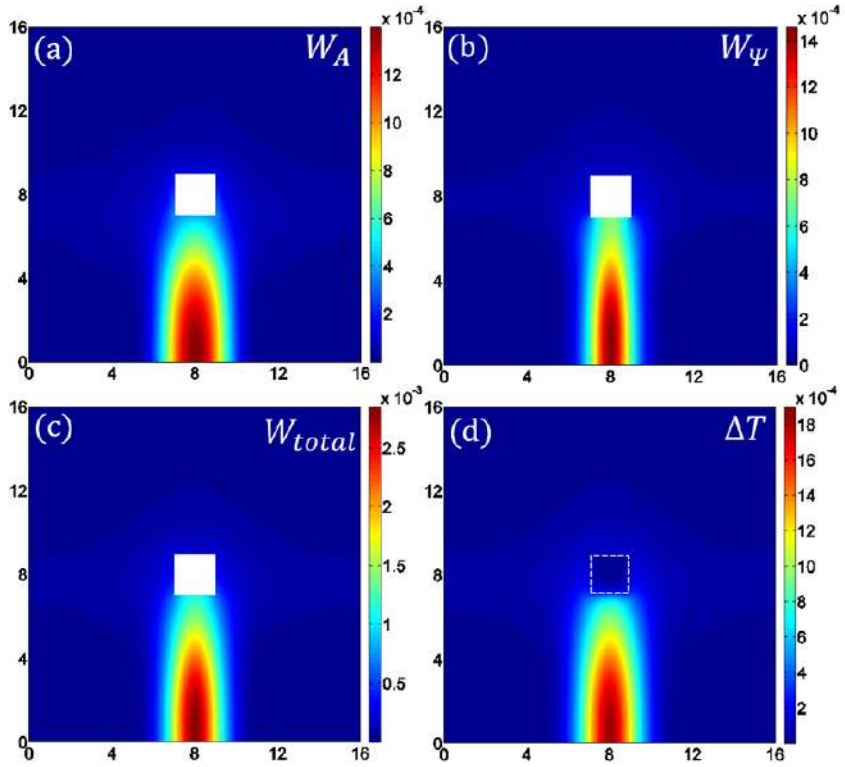

Figure 9. Intensity of the different contributions of dissipated power energy, (a) $W_{\mathbf{A}}$, (b) W_ψ and (c) W_{total}, taken immediately before the annihilation at $T = 0.8T_c$; panel (d) shows the variation of the temperature, ΔT, around the annihilation region. The dissipation and the heat diffusion are concentrated at the regions where the annihilation occurs and is narrower for W_ψ since it originates from the relaxation of ψ.

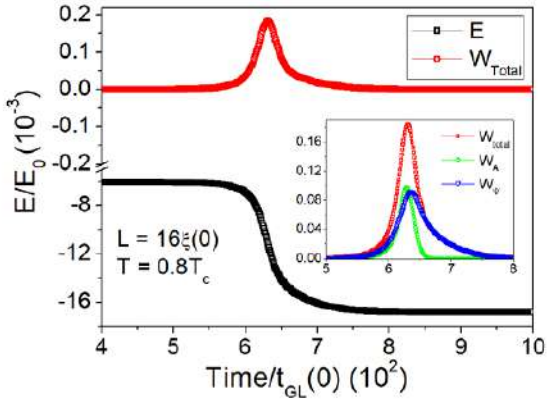

Figure 10. Superconducting (E) and dissipated energy (W_{total}) densities as a function of time in the vicinity of the annihilation for the $L = 16\xi(0)$ sample at $T = 0.8T_c$. The inset shows that the tail of W_{total} is related to the relaxation of ψ after the annihilation, as evidenced by the curves of $W_{\mathbf{A}}$ and W_ψ.

as shown in the lower inset of figure 7. Further ahead this result will be discussed in more detail.

Both the V and the AV acquire a high velocity immediately before the annihilation, and after the collision the energy of the system is reduced. The upper inset of figure 7 shows the variation of the superconducting energy, ΔE, as a function of H/H_{c2} at $T = 0.48T_c$ (dashed line of figure 3). ΔE was evaluated as the difference between the energy immediately before and just after the annihilation. The dips in the range (i) $0.15 < H/H_{c2} < 0.4$ are due to the trapping of a vortex (or two vortices for $L \geqslant 10\xi(0)$) in the hole; (ii) for $0 < H/H_{c2} < 0.14$ in systems with two penetrated vortices, one vortex leaves the sample and a spike is detected; and (iii) the dips around $H = -0.1H_{c2}$ are related to the annihilation of the V–AV pair. The main curve of figure 7 shows the values of the energy dips multiplied by the superconducting area, A_{SC}, as a function of $L/\xi(0)$. Here, $A_{\text{SC}} = L^2 - 2^2$, where 2^2 is the area of the hole in reduced units and $E_0 = \Phi_0^2/32\pi^3\xi(0)\kappa^2$. As we can see, the energy decreases monotonically with $L/\xi(0)$, since the average velocity, v_{avg}, for smaller systems is larger (see lower inset of the same figure).

Another signature of the size effect is the decreasing of v_{avg} as $L/\xi(0)$ is increased (see the lower inset of figure 7). In small samples, the hole is closer to the edge. In this case, the elongation of the vortex and the antivortex cores takes all the region where they are moving and in such degraded region, the pair moves faster. Panels (a) and (b) of figure 8 show the intensity of $|\psi|$ and $\log|\psi|$ with $L = 9\xi(0)$ where one can see that the superconducting state is degraded to some degree all around the sample. On the other hand, the degraded region for larger systems does not take all the extension between the border and the hole. Then, the motion of the V–AV pair

is influenced by the intact superconducting region and v_{avg} decreases as $L/\xi(0)$ increases. For $L \geqslant 11\xi(0)$, v_{avg} becomes nearly independent of the size of the system. In panels 8(c) and (d), the intensity of $|\psi|$ and $\log|\psi|$ for $L = 14\xi(0)$ system present a less degraded region which is responsible for lower v_{avg}. In real units, for the Pb–In compound, v_{avg} is of the order of 10^6 m s^{-1} and such a high velocity is due to the attraction between the V and the AV.

In the next section, we will analyze the kinematic aspects of the annihilation of an Abrikosov's V–AV pair.

3.2. Heat diffusion

The data discussed so far were obtained without taking into account dissipation and heat diffusion processes. When, however, heat transfer is considered, the values of the energy of figure 7 are still valid. In this part of the present study, we simulated similar systems as those ones described previously. We used equations (4) and (5) to estimate the dissipated energy, W_{total}, and the variation of the temperature, $\Delta T/T_c$, during the motion and the annihilation of a V–AV pair. The analysis was carried out for the $L = 16\xi(0)$ sample at $T = 0.8T_c$, $\gamma = 10$ and $u = 5.79$. In figure 9 the intensities of W_A, W_ψ, W_{total} and $\Delta T/T_c$ are shown in panels (a)–(d), respectively. The snapshots were taken immediately before the annihilation. As W_A is related to dissipation of normal currents, it takes a wider region in the sample than W_ψ. On the other hand, since W_ψ is due to the relaxation of ψ, a narrower region is dominated by this dissipation mechanism. Recently, Halbertal and coworkers have shown to be possible imaging thermal dissipation in nanoscopic systems by using nanoSQUIDs [57]. Then, our theoretical approach should be experimentally confirmed since ΔT is of the order of $10^{-3}T_c$ (see panel (d)), which is in the sensitivity range of such devices.

It is worth noting in figure 9 that the dissipation and the increase of the temperature are concentrated in the annihilation's region. Additionally, during the annihilation process, there is no subsequent penetration of V–AV pairs.

Figure 10 presents W_{total} and the superconducting energy, E, as a function of time during the annihilation; $W_{total}(t)$ has a tail which is due to the different time scale of W_A and W_ψ and is associated to the relaxation of ψ, as evidenced in the inset of this figure. One can also note that both dissipation mechanisms W_A and W_ψ have the same intensity. As a consequence, both contributions must be taken into account for a better description of the dissipative processes.

Since the magnetization is a measurable quantity, in figure 11, the $M(t)$ curve is shown for the $L = 16\xi(0)$ system and $T = 0.8T_c$. The positive signal of M is due to both the negative applied magnetic field and the vortex trapped in the hole. The insets show the snapshots of $\log|\psi|$ focusing in the region where the V–AV pair is formed. In panel (a) ($t = 5t_{GL}(0)$), it is shown the state where the V is still trapped in the hole; panel (b) ($t = 6.06t_{GL}(0)$) corresponds to the instant when the V leaves the hole; and in panel (c) ($t = 6.21t_{GL}(0)$), the AV penetrates the sample. At $t = 6.23t_{GL}(0)$ (panel (d)) corresponds to the instant of the V–AV collision, i.e. the very moment when the cores of V and AV are superimposed. Just after the annihilation,

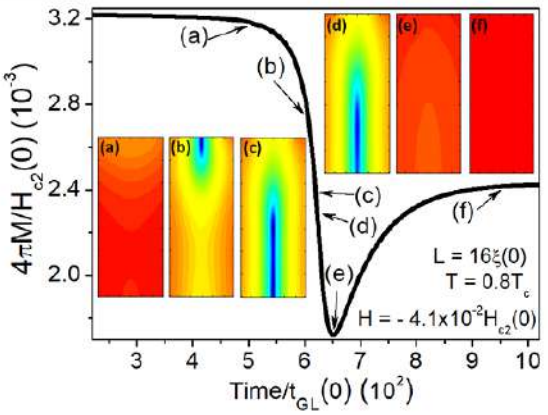

Figure 11. Magnetization as a function of time during the V–AV annihilation process. The snapshots of $\log|\psi|$ show the dynamics of the V–AV pair motion before and after the collision. (a) ($t = 5t_{GL}(0)$) the vortex is trapped in the hole; (b) ($t = 6.06t_{GL}(0)$) the vortex leaves the hole; (c) ($t = 6.2t_{GL}(0)$) the antivortex penetrates the sample; (d) ($t = 6.23t_{GL}(0)$) the V–AV collision; (e) ($t = 6.51t_{GL}(0)$) degradation due to the local heating and (f) ($t = 9.5t_{GL}(0)$) the near recovered superconducting region.

the temperature reaches its maximum value (as shown in figure 9(d)). The local increasing of the temperature generates further degradation of the superconducting state of the surroundings (see the peak of W_{total} in figure 10), as can be seen in panel figure 11(e) at the instant $t = 6.51t_{GL}(0)$. After the annihilation, the system begins to recover the local superconducting state at $t = 9.5t_{GL}(0)$ (see panel (f)). Since M is a response function, its characteristic time is different from that one of the W_{total} and the inflexion of the first one (where the annihilation occurs) does not match with the peak of the last one. After the annihilation, the remained response is due to the surface of the sample. The time during which $M(t)$ changes appreciably is $\delta t \approx 800t_{GL}(0)$, which is of the order of nanoseconds, since $t_{GL} \approx 10^{-13}$ seconds for the Pb–In alloy [56]. Thus, to detect the annihilation of an Abrikosov's V–AV pair using magnetometry would require a device with resolution in the timescale of nanoseconds.

4. Conclusions

In this work we studied the annihilation dynamics of Abrikosov's V–AV pairs in a mesoscopic superconductor with a central hole. In the collision process, the cores of the V and the AV elongates and a phase slip-like (PSlike) appears. In very small samples, $L < 10\xi(0)$, the PSlike degrades superconductivity on the entire region where the pair is moving increasing their average velocity. For systems with $L > 10\xi(0)$, non degraded superconducting regions remain in the moving area implying a lower average velocity. The formation of a V–AV pair and its consequent annihilation in the superconducting region depends on both the size of the system and the temperature. Then, we built an $L(T)$ diagram which can be used as a guide for the predicted occurrence of the annihilation process. The variation of the superconducting energy just before and immediately after the annihilation, multiplied by the superconducting area, increases as the size of the

samples decrease, in accordance with the average velocity of the antivortex, which is lower for larger samples. We coupled the thermal diffusion and the dissipated energies equations to the GTDGL ones. Although, the dissipative term related to the relaxation of the order parameter has been neglected in many works, here we have evidenced that it is a significant contribution to the dissipative processes. We also verified that the time of the V–AV collision is of the order of nanoseconds. Thus, conceivably, the annihilation of Abrikosov's V–AV pairs can be detected by measuring the magnetization response of the sample as a function of time, which would require fast and sensitive detection scheme. Another interesting aspect is that the local increase of the temperature in the annihilation is of the order of $10^{-3}T_c$, which can be measured by a SQUID thermal sensor as described by Halbertal *et al* [57].

Acknowledgments

We thank the Brazilian Agencies CNPq and the São Paulo Research Foundation (FAPESP), grants 2007/08072-0, 2012/04388-0 and 2016/12390-6, for financial support.

References

[1] Berciu M, Rappoport T G and Jankó B 2005 *Nature* **435** 71
[2] Brisbois J *et al* 2016 *Sci. Rep.* **6** 27159
[3] Lopes R F, Carmo D, Colauto F, Ortiz W A, Andrade A M H, Johansen T H, Baggio-Saitovitch E and Pureur P 2017 *J. Appl. Phys.* **121** 013905
[4] Buzdin A I and Brison J P 1994 *Phys. Lett.* A **196** 267
[5] Milošević M V, Kanda A, Hatsumi S, Peeters F M and Ootuka Y 2009 *Phys. Rev. Lett.* **103** 217003
[6] Sardella E and Brandt E H 2010 *Supercond. Sci. Technol.* **23** 025015
[7] Schweigert V A, Peeters F M and Singha Deo P 1998 *Phys. Rev. Lett.* **81** 2783
[8] Melnikov A S, Nefedov I M, Ryzhov D A, Shereshevskii I A, Vinokur V M and Vysheslavtsev P P 2002 *Phys. Rev.* B **65** 140503
[9] Geim A K, Grigorieva I V, Dubonos S V, Lok J G S, Maan J C, Filippov A E and Peeters F M 1997 *Nature* **390** 259
[10] Palacios J J 2000 *Phys. Rev. Lett.* **84** 1796
[11] Misko V R, Xu B and Peeters F M 2007 *Phys. Rev. B.* **76** 024516
[12] Zhao H J, Misko V R, Peeters F M, Oboznov V, Dubonos S V and Grigorieva I V 2008 *Phys. Rev.* B **78** 104517
[13] Golubovic D S, Milošević M V, Peeters F M and Moshchalkov V V 2005 *Phys. Rev.* B **71** 180502
[14] Baelus B J, Peeters F M and Schweigert V A 2001 *Phys. Rev.* B **63** 144517
[15] Sardella E, Lisboa-Filho P N and Malvezzi A L 2008 *Phys. Rev.* B **77** 104508
[16] Kanda A, Baelus B J, Peeters F M, Kadowaki K and Ootuka Y 2004 *Phys. Rev. Lett.* **93** 257002
[17] Mertelj T and Kabanov V V 2003 *Phys. Rev.* B **67** 134527
[18] Chibotaru L F, Ceulemans A, Bruyndoncx V and Moshchalkov V V 2000 *Nature* **408** 833
[19] Geurts R, Milošević M V and Peeters F M 2009 *Phys. Rev.* B **79** 174508
[20] Sardella E, Lisboa-Filho P N, Silva C C S, Cabral L R E and Ortiz W A 2009 *Phys. Rev.* B **80** 012506
[21] Zadorosny R, Duarte E C S, Sardella E and Ortiz W A 2014 *Physica* C **503** 94
[22] Milošević M V, Peeters F M and Jankó B 2011 *Supercond. Sci. Technol.* **24** 024001
[23] Gomes A, Gonzalez E M, Gilbert D A, Milošević M V, Kai Liu and Vicent J L 2013 *Supercond. Sci. Technol.* **26** 085018
[24] Kramer R B G, Silhanek A V, Gillijns W and Mochshalkov V V 2011 *Phys. Rev.* X **1** 021004
[25] Kapra A V, Misko V R, Vodolazov D Y and Peeters F M 2011 *Supercond. Sci. Technol.* **24** 024014
[26] Gladilin V N, Tempere J, Devreese J T and Moshchalkov V V 2012 *New J. Phys.* **14** 103021
[27] Shapiro I, Pechenik E and Shapiro B Ya 2001 *Phys. Rev.* B **63** 184520
[28] Ghinovker M, Shapiro B Ya and Shapiro I 2001 *Europhys. Lett.* **53** 240
[29] Aranson I, Gitterman M and Shapiro B Ya 1995 *Phys. Rev.* B **51** 3092
[30] Aranson I, Shapiro B Ya and Vinokur V 1996 *Phys. Rev. Lett.* **76** 142
[31] Berdiyorov G R, Milošević M V and Peeters F M 2009 *Phys. Rev.* B **79** 184506
[32] Gulevich D R and Kusmartsev F V 2007 *New J. Phys.* **9** 59
[33] Eom B H, Day P K, LeDuc H G and Zmuidzinas J 2012 *Nat. Phys.* **8** 623
[34] Vasyukov D *et al* 2013 *Nat. Nanotechnol.* **8** 639
[35] Rosticher M, Maneval F R, Dorenbos S N, Zijlstra T, Klapwijk T M, Zwiller V, Lupascu A and Nogues G 2010 *Appl. Phys. Lett.* **97** 183106
[36] Gol'tsman G N, Okunev O, Chulkova G, Lipatov A, Semenov A, Smirnov K, Voronov B, Dzardanov A, Williams C and Sobolewski R 2001 *Appl. Phys. Lett.* **79** 705
[37] Kerman A J, Dauler E A, Yang J K W, Rosfjord K M, Anant V, Berggren K K, Gol'tsman G N and Boronov B M 2007 *Appl. Phys. Lett.* **90** 101110
[38] Salim A J, Eftekharian A and Majedi A H 2014 *J. Appl. Phys.* **115** 054514
[39] Berdiyorov G R, Milošević M V and Peeters F M 2012 *Appl. Phys. Lett.* **100** 262603
[40] Schmid A 1966 *Phys. Kondens. Mater.* **5** 302
[41] Petković I, Lollo A, Glazman L I and Harris J G E 2016 *Nat. Commun.* **7** 13551
[42] Vodolazov D Y, Peeters F M, Morelle M and Moshchalkov V V 2005 *Phys. Rev.* B **71** 184502
[43] Berdiyorov G R, Chao X C, Peeters F M, Wang H B, Moshchalkov V V and Zhu B Y 2012 *Phys. Rev.* B **86** 224504
[44] Berdiyorov G R, Milošević M V, Latimer M L, Xiao Z L, Kwok W K and Peeters F M 2012 *Phys. Rev. Lett.* **109** 057004
[45] Hernandez A D and Dominguez D 2008 *Phys. Rev.* B **77** 224505
[46] Kramer L and Watts-Tobin R J 1978 *Phys. Rev. Lett.* **40** 1041
[47] Kramer L and Baratoff A 1977 *Phys. Rev. Lett.* **38** 518
[48] Gor'kov L P and Èliasberg G M 1968 *Sov. Phys.—JETP* **27** 328
[49] Gor'kov L P and Kopnin N B 1975 *Sov. Phys.—Usp.* **18** 496
[50] Gropp W D, Kaper H G, Leaf G K, Levine D M, Palumbo M and Vinokur V M 1996 *J. Comput. Phys.* **123** 254
[51] Milošević M V and Geurts E 2010 *Physica* C **470** 791
[52] Kogut J 1979 *Rev. Mod. Phys.* **51** 659
[53] Baranov V V, Balanov A G and Kabanov V V 2011 *Phys. Rev.* B **84** 094527
[54] Ivlev B I, Kopnin N B and Maslova L A 1980 *Sov. Phys. JETP* **51** 986 (http://www.jetp.ac.ru/cgi-bin/dn/e_051_05_0986.pdf)
[55] Ivlev B I, Kopnin N B and Larkin L A 1985 *Sov. Phys. JETP* **61** 337 (http://www.jetp.ac.ru/cgi-bin/dn/e_061_02_0337.pdf)
[56] Poole C P Jr, Farach H A, Creswick R J and Prozorov R 2007 *Superconductivity* 2nd edn (Amsterdam: Elsevier)
[57] Halbertal D *et al* 2016 *Nature* **539** 470

4.5. Vórtices cinemáticos

Na presença de correntes de transporte e, mesmo a campo magnético externo nulo, surge um estado resistivo que está associado à formação de pares de vórtice e antivórtice cinemáticos. Esses entes não apresentam um núcleo contendo um quantum de fluxo magnético e sua velocidade é tão alta que o mesmo se alonga formando algo parecido com uma phase-slip line. Nesse ínterim, há três orientandos trabalhando nessa linha e um artigo foi recentemente aceito para publicação com participação do Prof. José José Barba Ortega, da Colômbia. Outros artigos estão sendo escritos.

Para estudar tais fenômenos na presença de correntes de transporte aplicadas, usamos a primeira equação TDGL na sua forma generalizada (GTDGL)[5]. Essa mudança é necessária, pois quando uma corrente elétrica é aplicada no sistema supercondutor, ocorre o aparecimento dos pares de vórtices e anti-vórtices cinemáticos (V-AV). Nos pontos onde esses vórtices aparecem, o ψ é depreciado e possui valor nulo. A equação GTDGL possui um termo que está relacionado com a restauração do parâmetro de ordem nos locais degradados. Este termo tem relação com o tempo de colisão inelástica dos elétrons τ_E e é definido por $\gamma = 2\tau_E\psi_0/\hbar$. Assim, a GTDGL é dada por:

$$\frac{u}{\sqrt{1+\gamma^2|\psi|^2}}\left(\frac{\partial}{\partial t} + i\varphi + \frac{\gamma^2}{2}\frac{\partial|\psi|^2}{\partial t}\right)\psi = -(-i\boldsymbol{\nabla} - \boldsymbol{A})^2\psi + (1-T)\psi(g(r) - |\psi|^2), \qquad (4.64)$$

onde $g(r)$ é uma função relacionada à degradação de ψ (região de defeito), sendo que nas regiões supercondutoras $g(r) = 1$. Para $g(r) = 0$, é como se, naquele local, houvesse um supercondutor cuja T_c é menor e, por isso, um material mais degradado. As normalizações estão indicadas na eq. (4.3).

A equação (4.64) está acoplada com a equação do potencial escalar:

$$\nabla^2\varphi = \boldsymbol{\nabla}.\boldsymbol{J_s}, \qquad (4.65)$$

onde $\boldsymbol{J_s}$ é a densidade de corrente supercondutora, dada por (4.6).

As equações (4.64) e (4.65), já estão escritas na forma normalizada, onde o comprimento é expresso em termos de $\xi(0)$, a temperatura T em unidades de T_c, o tempo em unidades do tempo característico de Ginzburg-Landau $t_{GL} = \pi\hbar/k_BT_cu$, o campo magnético em unidades de $H_{c2}(0)$, o potencial eletrostático em unidades de $\varphi_0 = \hbar/2e\tau_{GL}$, o potencial vetor em termos de $H_{c2}(0)\xi(0)$ e o parâmetro de ordem em unidades de $\psi = (|\alpha|/\beta)^{1/2}$. O termo $u = 5{,}79$ é determinado a partir de considerações de primeiros princípios[3].

A equação (4.65) para o potencial elétrico é obtida usando a equação da continuidade:

[5] L. Kramer e R. J. Watts-Tobin, Phys. Rev. Lett. 40, 1041 (1978)
R. J. Watts-Tobin, Y. Kr¨ahenb¨uhl, e L. Kramer, J. Low Temp. Phys. 42, 459 (1981).

$$\frac{\partial \rho}{\partial t} + \boldsymbol{\nabla} . \boldsymbol{J} = 0 \,, \qquad (4.66)$$

onde $\boldsymbol{J} = \boldsymbol{J_s} + \boldsymbol{J_n}$, sendo $\boldsymbol{J_s}$ a densidade de corrente supercondutora, dada por (4.6) e $\boldsymbol{J_n} = -\boldsymbol{\nabla}\varphi$, é a densidade de corrente normal. Assumindo que não há acúmulo de carga, i.e., $\frac{\partial \rho}{\partial t} = 0$, obtemos que $\boldsymbol{\nabla} . \boldsymbol{J} = 0$, assim, temos a solução da expressão (4.65).

Às equações GTDGL, podemos associar as equações de dissipação de energia e difusão térmica, expressas na sequência, respectivamente. Detalhes do cálculo dessas expressões e seu acoplamento com a GTDGL está descrito na tese recém defendida de Elwis C. S. Duarte[6].

$$W = 2\left(\frac{\partial \boldsymbol{A}}{\partial t} + \nabla\varphi\right)^2 + \frac{2u}{\sqrt{1+\gamma^2|\psi|^2}}\left[\left|\frac{\partial \psi}{\partial t} + i\varphi\psi\right|^2 + \frac{\gamma^2}{4}\left(\frac{\partial |\psi|^2}{\partial t}\right)^2\right], \qquad (4.67)$$

$$C_{eff}\frac{\partial T}{\partial t} = K_{eff}\nabla^2 T + \frac{1}{2}W - \eta(T - T_0). \qquad (4.68)$$

Nas equações (4.67) e (4.68) temos que $C_{eff} = \frac{\pi^4}{48u}$ e $K_{eff} = \frac{\pi^4}{48u^2}$ são a capacidade e condutividade térmica efetiva do material, respectivamente. T é a temperatura local, T_0 a temperatura de banho térmico e η representa o coeficiente de transferência de calor para o substrato. As outras variáveis já foram definidas anteriormente.

Até a equação (4.66), temos ferramentas para estudar supercondutores mesoscópicos onde correntes de transporte são injetadas nos mesmos. O artigo apresentado na sequência mostra um estudo de como o parâmetro de deGennes afeta o surgimento de um estado resistivo na amostra. Tal parâmetro está associado às condições de contorno impostas à amostra as quais podem estar em contato ou com um metal, ou vácuo ou supercondutor mais robusto (de maior T_c).

Outros artigos sobre tal assunto estão sendo preparados e problemas correlatos estão sendo implementados no Grupo de Supercondutividade e Materiais Avançados, GSMA.

[6] Elwis Carlos Sartorelli Duarte, "Processos dissipativos e térmicos em supercondutores mesoscópicos: mecanismos de dissipação, difusão térmica e dinâmica de vórtices estudados suando o formalismo de Ginzburg-Landau". Tese de Doutorado, Ilha Solteira (2018).

Doctopic: Condensed matter ARTICLE IN PRESS PLA:24826

Physics Letters A ••• (••••) •••–•••

Contents lists available at ScienceDirect

Physics Letters A

www.elsevier.com/locate/pla

Influence of the deGennes extrapolation parameter on the resistive state of a superconducting strip

J. Barba-Ortega [a,*], Edson Sardella [b], R. Zadorosny [c]

[a] Grupo de Física Mesoscópica, Departamento de Física, Universidad Nacional de Colombia, Bogotá, Colombia
[b] Departamento de Física, Universidade Estadual Paulista (UNESP), Faculdade de Ciências, Caixa Postal 473, 17033-360, Bauru-SP, Brazil
[c] Departamento de Física e Química, Universidade Estadual Paulista (UNESP), Faculdade de Engenharia de Ilha Solteira, Caixa Postal 31, 15385-000 Ilha Solteira-SP, Brazil

ARTICLE INFO

Article history:
Received 30 August 2017
Received in revised form 10 November 2017
Accepted 12 November 2017
Available online xxxx
Communicated by L. Ghivelder

Keywords:
Ginzburg–Landau
deGennes parameter
Mesoscopics

ABSTRACT

We studied the resistive state of a mesoscopic superconducting strip (bridge) at zero external applied magnetic field under a transport electric current, J_a, subjected to different types of boundary conditions. The current is applied through a metallic contact (electrode) and the boundary conditions are simulated via the deGennes extrapolation length b. It will be shown that the characteristic current–voltage curve follows a scaling law for different values of b. We also show that the value of J_a at which the first vortex–antivortex (V–Av) pair penetrates the sample, as well as their average velocities and dynamics, strongly depend on the b values. Our investigation was carried out by solving the two-dimensional generalized time dependent Ginzburg–Landau (GTDGL) equation.

1. Introduction

One mechanism for the resistive state of current carrying superconductors is the formation of hot spots, where the local temperature T exceeds the transition temperature, T_c, and the superconducting order parameter is completely suppressed. It is believed that the hot spot mechanism dominates at low temperatures [1]. Another mechanism for the resistive state could be explained by the so called kinematic vortices (propagating waves of the order parameter).[1] These vortices have been discovered in theoretical works [2–4] and experimentally observed by using techniques such as laser imaging [5], multiprobe voltage measurements [6], and radio-frequency synchronization [7,8]. They move with velocity $\upsilon_{kv} \simeq 10^5$ m/s, which is much larger than the maximal measured speed of Shubnikov–Abrikosov vortices $\upsilon_{av} \simeq 10^3$ m/s [5]. Because of their very high velocity, kinematic vortices do not retain their circular structure [2,3]. Berdiyorov et al. studied the dynamics of the superconducting condensate and the effect of pinning on the time response of bridges under an external applied *dc* current. They show that, depending on the applied current, the resistive state is characterized by either the flux-flow, the phase-slip or the hot-spot states and observed qualitative changes in the dynamics of the superconducting condensate [4], [9]. In reference [10] it was shown that the V–Av pairs can also be magnetically activated by applying an external magnetic field to a square mesoscopic superconductor with a concentric square hole. Very recently, this system was studied in more details by taking into account heat diffusion effects in the annihilation of the V–Av pairs [11]. It was shown that the local increase of temperature should be experimentally measured by using nanoSQUIDs [12]. Fink et al. studied the effect of deGennes boundary parameter, b, on T_c for various sample geometries. They found that b can be used to describe a reduction or an enhancement of T_c in small superconductors [13].

In recent works, the effect of the deGennes extrapolation length b on the superconducting state of two and three dimensional specimens were studied. The structural and magnetic properties of the vortex state are significantly modified as the size of the sample is comparable to the coherence length ξ and/or the London penetration depth λ [14–16].

In this contribution, we study the resistive response of the superconducting condensate of bridges under an external applied current at zero applied magnetic field (see Fig. 1). Both sides of the bridge are attached to two electrodes symmetrically positioned (indicated by the blue color). The superconductor is covered by a very thin layer of a different material, which was adjusted by

* Corresponding author.
E-mail address: jjbarbao@unal.edu.co (J. Barba-Ortega).

[1] It is already well accepted that the kinematic vortices are constituted of a V–Av pair which moves at a much larger velocity than a normal Abrikosov vortex. The order parameter nearly vanishes along the line where the kinematic vortices move, although it has two minima which carry the singularities of its phase.

https://doi.org/10.1016/j.physleta.2017.11.010
0375-9601/

Please cite this article in press as: J. Barba-Ortega et al., Influence of the deGennes extrapolation parameter on the resistive state of a superconducting strip, Phys. Lett. A (2018), https://doi.org/10.1016/j.physleta.2017.11.010

Doctopic: Condensed matter ARTICLE IN PRESS PLA:24826

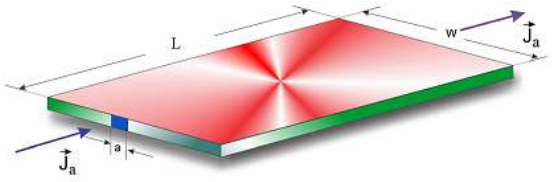

Fig. 1. (Color online) Schematic view of the studied system: a bridge of length L and width W; the width of the electrodes is a, through which a uniform dc current density J_a is injected.

changing the values of b (indicated by green color). A systematic study was carried out by considering different interfaces such as superconductor–vacuum (SC–V), superconductor–normal metal (SC–M), superconductor–superconductor at a higher T_c (SC–SC). We found that the value of the critical current density J_{c1}, at which the first kinematic vortex enters the sample, strongly depends on the boundary conditions.

This paper is outlined as follows. In Section 2 we describe the theoretical formalism used to study a mesoscopic bridge in the presence of an applied current at zero magnetic field. Then, in Section 3 we present the results that come out from the numerical solution of the GTDGL equation for the three types of boundary conditions specified previously. In Section 4 we present our conclusions.

2. Theoretical formalism

In the present investigation we consider a very thin bridge of thickness $d \ll \xi$, and intermediate width ($\xi \ll W \ll \lambda$). Within this approximation we can neglect the magnetic field produced by the transport current itself. Therefore, this can be treated as a two dimensional problem [2]. The general form of the GTDGL equation in dimensionless units is given by [17–19]:

$$\frac{u}{\sqrt{1+\Gamma^2|\psi|^2}}\left[\frac{\partial}{\partial t}+i\varphi+\frac{\Gamma^2}{2}\frac{\partial|\psi|^2}{\partial t}\right]\psi = (\nabla - i\mathbf{A})^2\psi + (1-|\psi|^2)\psi\,, \tag{1}$$

which is coupled to the equation for the electrostatic potential $\Delta\varphi = \mathrm{div}\left\{\mathrm{Im}[\bar{\psi}(\nabla - i\mathbf{A})\psi]\right\}$.

Here, distances are scaled by the coherence length ξ, time is in units of the Ginzburg–Landau time $t_{GL} = \pi\hbar/8k_BT_cu$, the electrostatic potential φ is given in units of $\varphi_0 = \hbar/2et_{GL}$, the vector potential $\mathbf{A}$ is scaled by $H_{c2}\xi$, where H_{c2} is the bulk upper critical field. From first principles, we obtain the parameters $u = 5.79$ and $\Gamma = t_E\psi_0/\hbar$ (which is material dependent, t_E being the inelastic scattering time) [17]. Neumann boundary conditions are taken at all sample boundaries, except at the electrodes where we used $\psi = 0$ and $\nabla\varphi\,|_n = -J_a$, where J_a is the external applied current density in units of $J_0 = c\sigma\hbar/2et_{GL}$; σ is normal electrical conductivity. As we have mentioned above, in Eq. (1) the screening of the magnetic field is neglected, since we restrict ourselves to thin superconducting samples (see references [2], [4] and [16]). The phase diagram of mesoscopic superconductors is strongly influenced by the boundary conditions for the order parameter. In general, they are given by the deGennes boundary conditions:

$$\mathbf{n}\cdot(i\nabla + \mathbf{A})\psi = -\frac{i}{b}\psi\,, \tag{2}$$

where $\mathbf{n}$ is the unit vector normal outward the superconductor–medium interface, and b is the deGennes surface extrapolation length. We must emphasize that the superconductor is covered by a very thin layer of another material; b depends on the properties of the interface. It is maximum for an ideal surface with the mirror reflection of quasi-particles and minimum for the rough surface with the diffusive reflection [20–23]. We unify all the boundary conditions upon introducing the parameter

$$\gamma = \begin{cases} 1 - \frac{\delta}{b}\,, & \text{if } b \neq 0, \\ 0\,, & \text{if } b = 0, \end{cases} \tag{3}$$

where δ is the resolution of the meshgrid used to solve Eq. 1 numerically. For convenience, this notation allows us to obtain a more comprehensive analysis of the results. Thus (i) and $\gamma = 0$ simulates an interface at the normal state, i.e., the Dirichlet boundary condition ($b = 0$, where $\psi = 0$); (ii) $0 < \gamma < 1$ simulates a SC–M interface ($b > \delta$); (iii) $\gamma = 1$ simulates a SC–V interface ($b \to \infty$); (iv) a SC–SC interface is described by $\gamma > 1$ ($b < 0$).

The first branch of the γ parameter of Eq. (3) arises from the discretization of the deGennes boundary condition of Eq. (2) (for more details, see reference [14]); γ relates the value of ψ at the boundary with its value in an adjacent point inside the superconductor. The second branch is just a definition. Thus, we unify all the boundary conditions under consideration, $b < 0$, $b = 0$, $b > 0$ and $b \to \infty$, in a single parameter.

Then, except at the electrodes, we employ the deGennes boundary conditions with $b \neq 0$ for the order parameter. In order to solve Eq. (1) numerically, we used the link-variable method as sketched in references [24–26]. In the numerical approximations, the Γ parameter is the relevant one to solve Eq. (1) (see reference [14]). If $\Gamma = 0$ (gapless superconductor), then there will be no kinematic vortex. In this case, the system goes straight to the normal state above a certain critical value of the dc current.

3. Results and discussion

3.1. The I–V characteristic curve

We consider a bridge of width $W = 8\xi$ and length $L = 12\xi$ in absence of an external magnetic field and in the presence of a dc current density J_a uniformly applied through the electrodes of width $a = 2\xi$; we used $\Gamma = 10$. The rage $10 \leq \Gamma \leq 20$ is suitable for most metals like Nb [9,17,18]. We considered a uniform meshgrid with a resolution of 10 points per ξ, that is, $\delta = 0.1\xi$.

In order to analyze the response of the superconductor to an external dc current, we calculated the I–V characteristic curves of the bridge, which are shown in Fig. 2 for six values of the γ parameter. As we can see from this figure, the values of J_{c1} for which a resistive state takes place are 1.08, 1.22, 1.36, 1.74, 2.12, 2.60 for $\gamma = 0, 0.8, 0.9, 1, 1.05, 1.1$ respectively. The small resistance for $J_a < J_{c1}$ is due solely to the electrodes. Note that for $\gamma < 1$ ($\gamma > 1$) J_{c1} decreases (increases) compared to the SC–V interface critical current density. The striking result is the extent for which the resistive phase persists before the system goes to the normal state for a small increase of γ. In addition, we can observe that a small decrease in the value of γ substantially diminishes the value of the critical current density. This is an important result, since in the fabrication process of superconducting samples, it is inevitable the contamination of the material at the borders, which produces a value of $\gamma < 1$.

For $J_a > J_{c1}$, the system goes into a resistive state with a finite jump in the output voltage, signaled by a discontinuity in the resistance $\partial V/\partial J_a$ as a function of the applied current J_a. The results are shown in Fig. 3 for the boundary conditions $\gamma = 0.8, 1, 1.05$. This resistive state is characterized by the fast-moving vortices as reported in several works [27,28]. The dynamics of the V–Av pairs will be discussed in more details in subsection 3.3.

3.2. The first critical current density

Now we will determine the relationship between J_{c1} and γ. For this end, we registered the values of the first critical current density for several boundary conditions and in Fig. 4 it is plotted J_{c1}

Please cite this article in press as: J. Barba-Ortega et al., Influence of the deGennes extrapolation parameter on the resistive state of a superconducting strip, Phys. Lett. A (2018), https://doi.org/10.1016/j.physleta.2017.11.010

Doctopic: Condensed matter ARTICLE IN PRESS PLA:24826

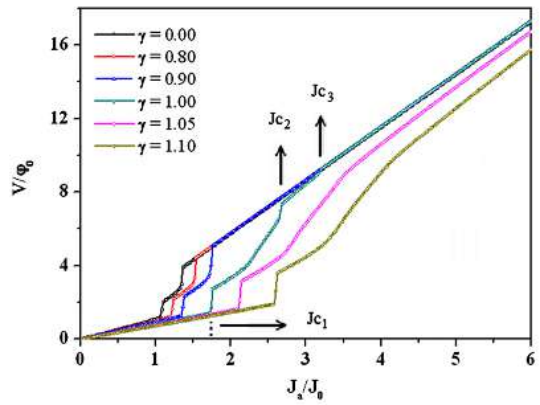

Fig. 2. Time-averaged voltage V as a function of the applied current-density J_a for several values of γ. The arrows indicate the critical current densities only for the *SC–V* interface ($\gamma = 1$).

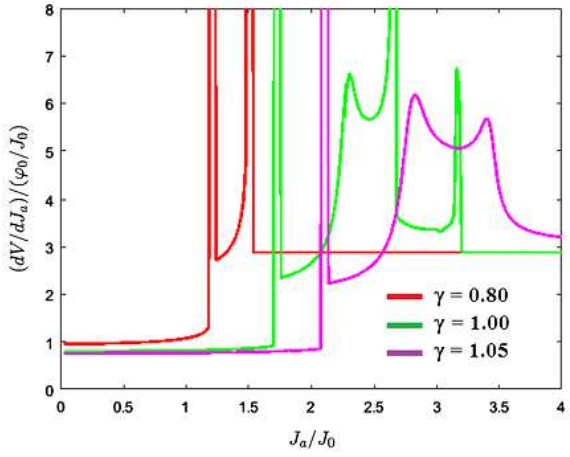

Fig. 3. (Color online) Curve of the resistivity $\partial V/\partial J_a$ as a function of the applied current J_a for the indicated boundary conditions.

as a function of γ. As we can see, J_{c1} increases exponentially with γ, according to the expression $J_{c1} \simeq 1.080 + 0.0002\exp(\gamma/0.123)$ (blue line in Fig. 4). The rapid growth of J_{c1} means that the smaller the metallic boundary is, i.e., the more enhanced the surface superconductivity is, the more diamagnetic the material will be. From an experimental point of view, this is an important result, since the appearance of a resistive state occurs for larger J_{c1} as γ increases. Thus, the shielding of the first penetration of the kinematic vortices could be strongly enhanced by surrounding the bridge by a thin layer of another superconducting material of higher T_c.

3.3. The V–Av nucleation dynamics

Now, we will turn our discussion to the dynamics of the nucleation of the *V–Av* pairs. But first, let us make some considerations of results previously found. In the pioneering work of Andronov et al. [2], it is was found that, if $a = W$, the current distribution is uniform in the longitudinal direction. In this case, the order parameter is uniform along the channel ($x = L/2$ line).[2] Thus, no instability is produced in the resistive phase and the system goes

[2] It should be noted that in this work we use the term *channel* to denominate the line through which the kinematic vortices will move. In reference [2], it was used to denominate the superconducting strip itself.

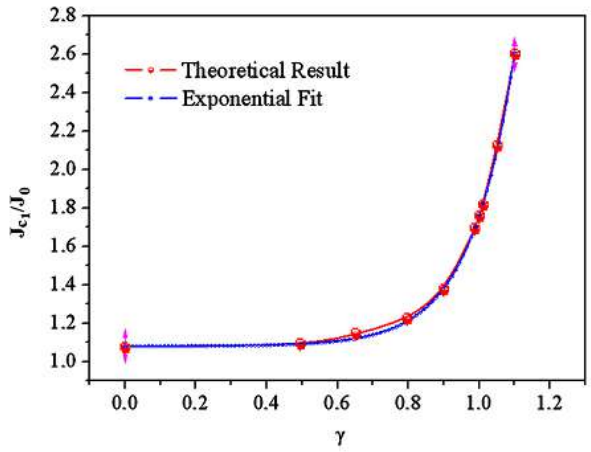

Fig. 4. (Color online) J_{c1} as a function of γ; theoretical results (red line) and exponential fit (blue line).

straight to the normal state at $J_a = J_{c1}$. However, if an inhomogeneity is introduced (say, a defect) along the channel, both the potential and the order parameter become unstable for $J_a > J_{c1}$. In this scenario, the kinematic vortices constituted by a *V–Av* pair start nucleating in the sample. In reference [3] it was argued that the inhomogeneity across the transversal direction is sufficient to originate the kinematic vortices, but not necessary. If we consider an uniform channel, but take an electrode smaller then the width of the bridge, a locally injected current density will produce an electronic instability in the superconducting condensate along the transversal channel.

The authors of reference [3] have argued that, for $J_a > J_{c1}$ the kinematic vortices first sprout at the center of the channel and propagate towards the edges and finally disappear. When J_a achieves a determined value, there is an inversion in the formation of the *V–Av* pairs, they nucleate at the edges and move towards the center where they annihilate one each other. This inversion on the nucleation fairly coincides with the maximum of the resistance in the interval $J_{c1} < J_a < J_{c2}$ (see Fig. 3). The nucleation and annihilation of the *V–Av* pairs persist until $J_a = J_{c2}$. From Fig. 3, we can see that for $\gamma = 1$ we have obtained exactly the same result as the equivalent one found in reference [3]. In the interval $J_{c2} < J_a < J_{c3}$ the system is in a partially normal state where the superconductivity is nearly destroyed in the whole bridge, except at the corners.

In the context of references [2] and [3], we have two factors responsible for the vortex dynamics in the resistive state, either a defect is present along the channel or the electrode size is smaller then the width of the bridge, $a < W$. Here, we have an additional factor which is the deGennes extrapolation length. We have observed that whether the local inversion on the formation of the *V–Av* pairs occurs or not also depends on the values of γ.

In Fig. 5 it is plotted the average velocity, V_m, of a vortex during the annihilation with an antivortex. The upper panel is for the *SC–M* interfaces simulated with $\gamma = 0.6, 0.8, 0.9$, and in the lower panel it is shown the V_m curves for the *SC–SC* interfaces simulated with $\gamma = 1.05, 1.1$. In this last case, we can see that, as γ increases, the intensity of the peak of V_m decreases and is shifted towards larger values of J_a. For $0 < \gamma < 1$, V_m decreases monotonically as J_a increases. Such samples present only one type of *V–Av* dynamics, i.e., all the pairs are formed at the center perpendicular to the current direction and annihilate at the border of the sample (see Fig. 6). This behavior is a coherent physical result, since for metal interfaces, the degradation of the superconductivity on the edge of the bridge precipitates the nucleation of the normal

Please cite this article in press as: J. Barba-Ortega et al., Influence of the deGennes extrapolation parameter on the resistive state of a superconducting strip, Phys. Lett. A (2018), https://doi.org/10.1016/j.physleta.2017.11.010

Doctopic: Condensed matter ARTICLE IN PRESS PLA:24826

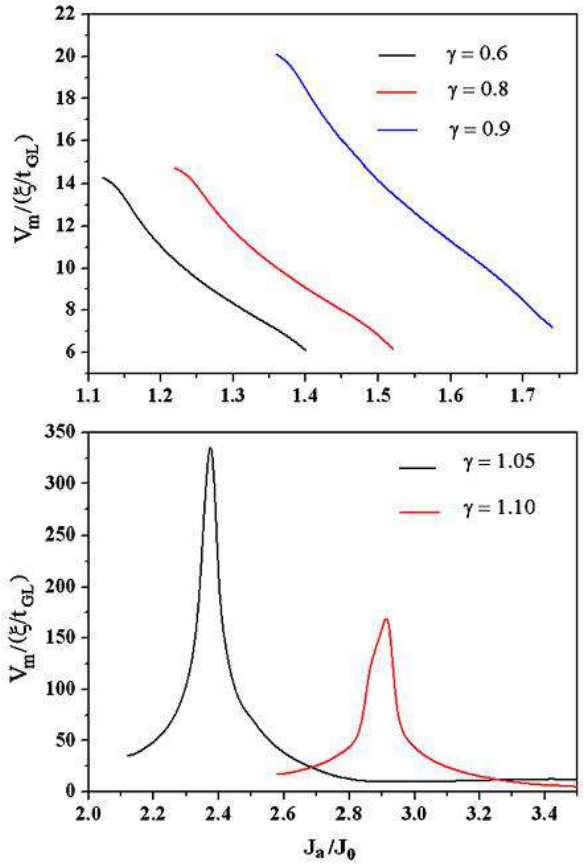

Fig. 5. (Color online) Average velocity of the *V–Av* pairs, V_m, for a *SC–M* interfaces simulated with $0 < \gamma < 1$ (upper panel) and for the *SC–SC* at higher critical temperature interfaces simulated with $\gamma > 1$ (lower panel).

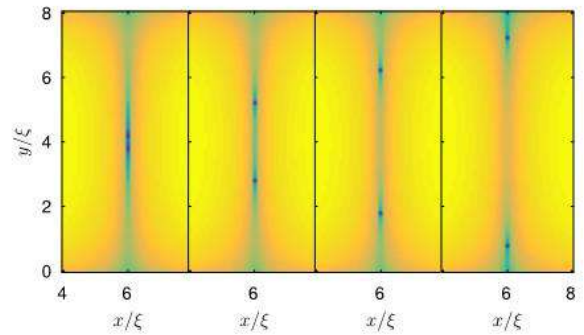

Fig. 6. (Color online) Snapshots of the logarithm of the order parameter, $\ln|\psi|$, (yellow/blue corresponds to largest/zero $|\psi|$) for $\gamma = 0.8$ and $J_a = 1.38\,J_0$. In this case the *V–Av* pairs always nucleate at the center of the sample and are ejected through the edges.

state and there is no time for an inflection in the *I–V* characteristic curve between the two transitions, as can be seen from Fig. 3.

For $\gamma > 1$, the dynamics is similar to the *SC–V* case. First, the *V–Av* pairs are nucleated at the center of the sample and then move along the channel until they are ejected at the borders of the bridge, as illustrated in Fig. 7. After the maximum of the average velocity (see lower panel of Fig. 5) the kinematic vortices are formed at the edge of the bridge and annihilate one each other at the center, as can be seen from Fig. 8.

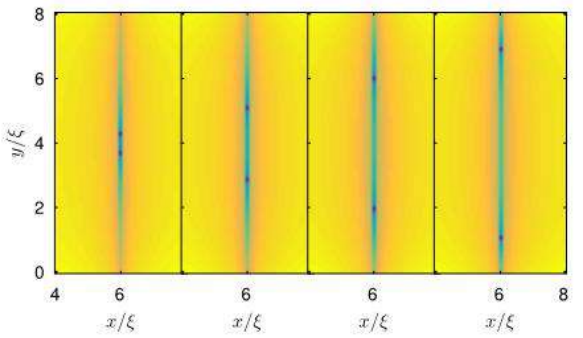

Fig. 7. (Color online) The same as Fig. 6 for $\gamma = 1.05$ and $J_a = 2.22\,J_0$. In this case, for $J_{c1} \leq J_a \leq 2.80\,J_0$, the *V–Av* pairs always nucleate at the center of the sample and are ejected at the edges.

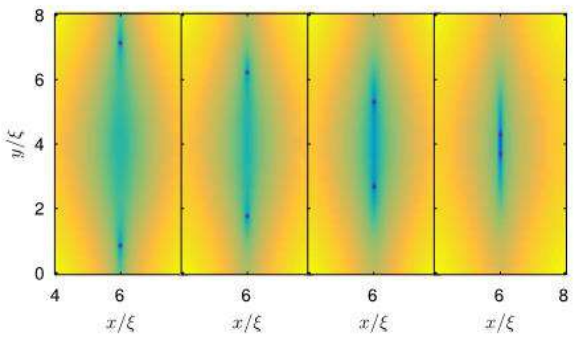

Fig. 8. (Color online) The same as Fig. 7 for $\gamma = 1.05$ and $J_a = 3.12\,J_0$. In this situation, for $J_a > 2.80\,J_0$, there is an inversion in the formation the *V–Av* pairs. They always nucleate at the border of the sample and are annihilated at the center.

As a final remark, we note that the order of magnitude of the average velocity of the *V–Av* pairs are much lower for the *SC–SC* interface than for the *SC–V* counterpart. This can be explained as follows. For $\gamma > 1$, superconductivity is considerably enhanced throughout the bridge. Thus, the medium becomes more viscous for the *V–Av* pairs. This is an important result for controlling the speed of these objects, so that we can avoid heating generation.

4. Conclusions

By solving the GTDGL equation, we studied the resistive state of superconducting bridges under an applied *dc* electrical current for different boundary conditions. We found that the critical current for the transition to the resistive state, J_{c1}, shows a strong dependence with the type of boundary conditions. We have found that, a superconductor–superconductor at a higher T_c boundary avoids the appearance of resistive state, increasing J_{c1}. We also found an analytical dependence of J_{c1} with the γ parameter, and have shown that the dynamics of the *V–Av* along the central channel of the bridge strongly depends on this parameter. Thus, our results are of experimental importance since the kinematic vortex dynamics can be controlled by depositing other materials at the boundaries of mesoscopic superconducting devices.

Acknowledgements

We thank the Brazilian Agencies CNPq and the São Paulo Research Foundation (FAPESP), grants 2012/04388-0 and 2016/12390-6, for financial support.

Please cite this article in press as: J. Barba-Ortega et al., Influence of the deGennes extrapolation parameter on the resistive state of a superconducting strip, Phys. Lett. A (2018), https://doi.org/10.1016/j.physleta.2017.11.010

Doctopic: Condensed matter ARTICLE IN PRESS PLA:24826

References

[1] W.J. Skocpol, M.R. Beasley, M. Tinkham, J. Appl. Phys. 45 (1974) 4054.
[2] A. Andronov, I. Gordion, V. Kurin, I. Nefedov, I. Shereshevsky, Physica C 213 (1993) 193.
[3] G. Berdiyorov, M.V. Milošević, F.M. Peeters, Phys. Rev. B 79 (2009) 184506.
[4] G. Berdiyorov, K. Harrabi, F. Oktasendra, K. Gasmi, A.I. Mansour, J.P. Maneval, F.M. Peeters, Phys. Rev. B 90 (2014) 054506.
[5] A.G. Sivakov, A.M. Glukhov, A.N. Omelyanchouk, Y. Koval, P. Muller, A.V. Ustinov, Phys. Rev. Lett. 91 (2003) 267001.
[6] G.J. Dolan, L.D. Jackel, Phys. Rev. Lett. 39 (1977) 1628.
[7] R.B. Laibowitz, A.N. Broers, J.T.C. Yeh, J.M. Viggiano, Appl. Phys. Lett. 35 (1979) 891.
[8] W.J. Skocpol, M.R. Beasley, M. Tinkham, J. Low Temp. Phys. 16 (1974) 145.
[9] G. Berdiyorov, K. Harrabi, J.P. Maneval, F.M. Peeters, Supercond. Sci. Technol. 28 (2015) 025004.
[10] E. Sardella, P.N. Lisboa-Filho, C.C.S. Silva, L.R.E. Cabral, W.A. Ortiz, Phys. Rev. B 80 (2009) 012506.
[11] E.C.S. Duarte, E. Sardella, W.A. Ortiz, R. Zadorosny, J. Phys. Condens. Matter 29 (2017) 405605.
[12] D. Halbertal, J. Cuppens, M. Ben Shalom, L. Embon, N. Shadmi, Y. Anahory, H.R. Naren, J. Sarkar, A. Uri, Y. Ronen, Y. Myasoedov, L.S. Levitov, E. Joselevich, A.K. Geim, E. Zeldov, Nature 539 (2016) 470.
[13] H. Fink, S. Haley, C.V. Giuraniucz, V.F. Kozhevnikovz, J.O. Indekeu, Mol. Phys. 103 (21) (2005) 2969.
[14] J. Barba-Ortega, E. Sardella, J.A. Aguiar, Supercond. Sci. Technol. 24 (2011) 015001.
[15] J. Barba-Ortega, E. Sardella, J.A. Aguiar, Phys. Lett. A 379 (2015) 732.
[16] M. Tinkham, J. Low Temp. Phys. 35 (1979) 147.
[17] L. Kramer, R.J. Watts-Tobin, Phys. Rev. Lett. 40 (1978) 1041.
[18] J. Watts-Tobin, Y. Krähenbühl, L. Kramer, J. Low Temp. Phys. 42 (1981) 459.
[19] D.Y. Vodolazov, F.M. Peeters, M. Morelle, V.V. Moshchalkov, Phys. Rev. B 71 (2005) 184502.
[20] P.G. de Gennes, Superconductivity of Metals and Alloys, Addison-Wesley, New York, 1994.
[21] P.G. de Gennes, J. Matricon, Rev. Mod. Phys. 36 (1964) 45.
[22] E.A. Andrushin, V.L. Ginzburg, A.P. Silin, Usp. Fiz. Nauk 163 (1997) 105.
[23] R.O. Zaitsev, Zh. Eksp. Teor. Fiz. 48 (1965) 1759.
[24] W.D. Gropp, H.G. Kaper, G.K. Leaf, D.M. Levine, M. Palumbo, V.M. Vinokur, J. Comput. Phys. 123 (1996) 254.
[25] G. Buscaglia, C. Bolech, C. Lopez, in: J. Berger, J. Rubinstein (Eds.), Connectivity and Superconductivity, Springer, Heidelberg, 2000.
[26] M.V. Milošević, R. Geurts, Physica C 470 (2010) 791.
[27] A.V. Silhanek, M.V. Milošević, R.B.G. Kramer, G.R. Berdiyorov, J. Van de Vondel, R.F. Luccas, T. Puig, F.M. Peeters, V.V. Moshchalkov, Phys. Rev. Lett. 104 (2010) 017001.
[28] L.N. Bulaevskii, M.J. Graf, V.G. Kogan, Phys. Rev. B 85 (2012) 014505.

Please cite this article in press as: J. Barba-Ortega et al., Influence of the deGennes extrapolation parameter on the resistive state of a superconducting strip, Phys. Lett. A (2018), https://doi.org/10.1016/j.physleta.2017.11.010

Conclusão

Nesse trabalho objetivamos demonstrar de uma forma sequencial a evolução dos nossos estudos e a contribuição que demos para o entendimento da dinâmica de vórtices em supercondutores mesoscópicos. Atualmente temos encontrado certas dificuldades em publicar trabalhos puramente teóricos. Sendo assim, estudos experimentais foram iniciados para a fabricação de nanofios de supercondutores cerâmicos tal como o YBCO. Nossa expectativa é conseguir simular esses materiais e contrastar os resultados teóricos com aqueles experimentais. Há, também, um outro trabalho em início de desenvolvimento no qual estudaremos a dinâmica de vórtices em interfaces de supercondutores tipo I e tipo II. Esse estudo também terá um análogo experimental o qual está em desenvolvimento no Grupo de Supercondutividade e Magnetismo, GSM, da UFSCar.

Em anexo, é exposto o trabalho publicado sobre a fabricação de nanofios de supercondutor cerâmico.

Ceramics International 42 (2016) 16230–16234

Contents lists available at ScienceDirect

Ceramics International

journal homepage: www.elsevier.com/locate/ceramint

YBCO ceramic nanofibers obtained by the new technique of solution blow spinning

M. Rotta, L. Zadorosny, C.L. Carvalho, J.A. Malmonge, L.F. Malmonge, R. Zadorosny *

Departamento de Física e Química, Univ Estadual Paulista-UNESP, Caixa Postal 31, Ilha Solteira, SP, 15385-000 Brazil

ARTICLE INFO

Article history:
Received 30 June 2016
Received in revised form
19 July 2016
Accepted 22 July 2016
Available online 27 July 2016

Keywords:
A. Sol-gel processes
B. Nanocomposites
Solution blow spinning

ABSTRACT

This study proposes a novel solution blow spinning technique (SBS) for fabricating YBCO ceramic nanofibers. The precursor solutions were obtained from Y, Ba, and Cu metallic acetates (Ac) and poly(vinyl pyrrolidone) (PVP, Mw=360,000). Ac: PVP concentrations of 1:1 and 5:1 were tested, resulting in ceramic nanofibers with average diameters of 359 and 375 nm, respectively. X-ray diffraction confirmed the formation of a pure phase of $YBa_2Cu_3O_{7-x}$. This is the first study to use SBS for fabricating YBCO nanofibers, and this technique shows promise for obtaining high-quality ceramic materials.

1. Introduction

Novel techniques are urgently required for fabricating materials owing to developments in nanotechnology and miniaturized devices [1,2]. Currently, electrospinning (ES) is used for fabricating one-dimensional nanostructured materials such as wires [3], tubes [4], and fibers [5] by applying high voltage between a tip and a collector to disperse a polymeric solution and create nanofibers [6–14] . Recently, a simple technique called solution blow spinning (SBS) has attracted attention for producing one-dimensional polymeric and ceramic samples [15,16]. SBS can produce tens of times more nanofibers than ES with improved cost/benefit ratio [17,18]. It does not require high voltages or a conducting collector. Furthermore, it can be used in a variety of polymeric solutions, regardless of their dielectric constant and heat sensitivity, such as some proteins [17].

Oxide ceramics of the Y-Ba-Cu-O (YBCO) system are an interesting class of materials that has not yet been studied in the framework of SBS [6,19–21]. YBCO, owing to their superconducting properties, have been applied in nanoscale molecular circuits [22], high-frequency electronics [23,24], power transmission [25], transformers [26], generators [27], and motors [28].

This study produced high-quality YBCO nanofibers by SBS. Samples were successfully obtained with an average diameter of 368 nm, and X-ray diffraction (XRD) analysis confirmed the formation of a pure phase. To the knowledge of the authors, this is the first study to produce such a ceramic system by SBS.

The outline of this paper is as follows. First, we provide an overview of the materials and method used to obtain the precursor solution and, consequently, the nanofibers. Then, we describe the processes applied for the thermal treatment and characterization of the samples. The remainder of the paper presents and discusses the obtained results.

2. Experimental procedures

2.1. Materials

Sol-gel precursor solutions were produced by using the following reagents: poly(vinyl pyrrolidone) (PVP, Mw=360,000), yttrium acetate hydrate [$Y(CH_3CO_2)_3xH_2O$] (99.9%) from Sigma, and barium acetate [$Ba(CH_3CO_2)_2$] (99%) and copper acetate monohydrate [$Cu(CH_3CO_2)_2\ H_2O$] (99%), both from Sigma Aldrich. Before the reagents were weighted, they were dried overnight at 100 °C.

2.2. Sol-gel process

Initially, PVP was dissolved in a solution of 65% methanol, 21% acetic acid, and 14% propionic acid at a concentration of 5 wt%. Then, acetates were added to obtain the correct stoichiometric composition of Y:Ba:Cu=1:2:3. The final solution, called the "precursor solution," was stirred at room temperature for 24 h in a hermetic vessel to obtain a stable and homogeneous solution for spinning. As expected, by keeping a fixed PVP concentration, e.g., 5 wt%, the morphologies and fiber diameters of the produced samples showed similar values [18], as discussed in Section 3. However, to confirm the formation of the composite and YBCO

* Corresponding author.

http://dx.doi.org/10.1016/j.ceramint.2016.07.152
0272-8842/

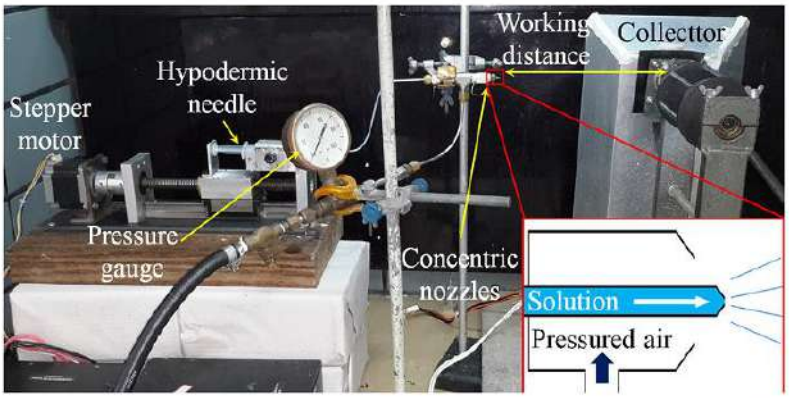

Fig. 1. SBS experimental apparatus. The stepper motor pushes the hypodermic needle loaded with the precursor solution. Then, the pressured air in the outer nozzle drags the solution in the inner nozzle. As the solution travels along the work distance, the solvents evaporate and nanofibers are formed. In the rotating collector, a thin blanket with nanofibers is obtained. For more details, see Ref. [17,18].

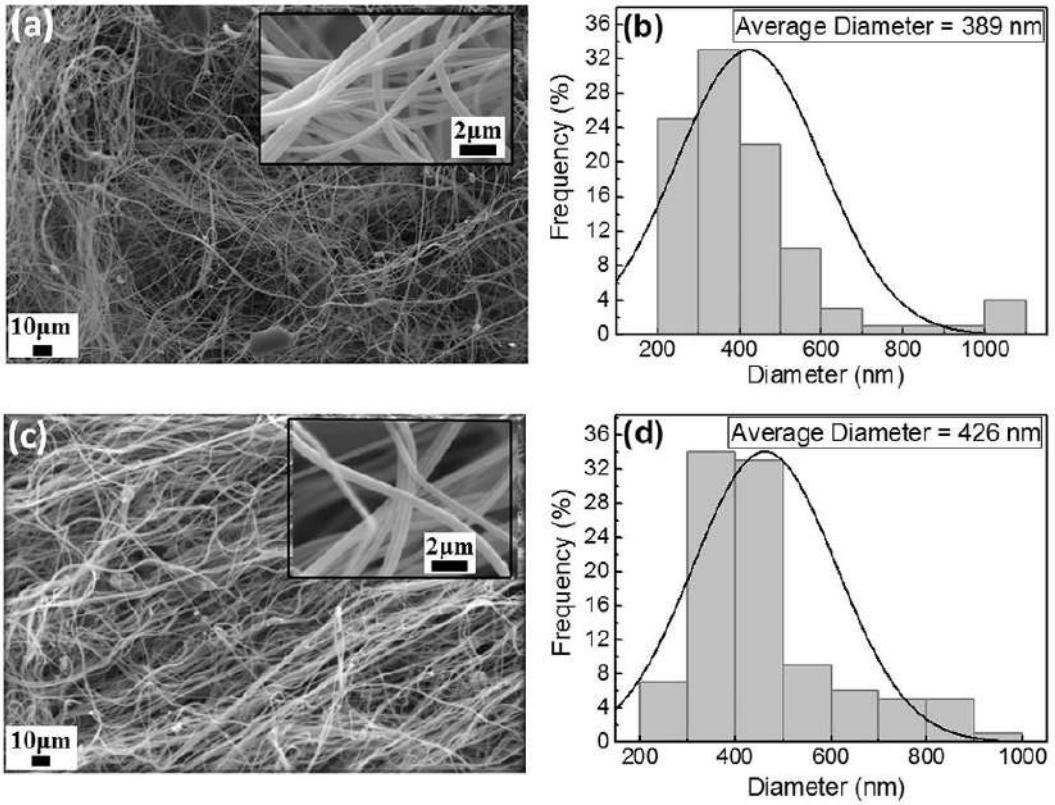

Fig. 2. (a) SEM micrographs of the as produced S51 sample and (b) the size distribution of the S51 nanofibers. (c) SEM micrographs of the as produced S11 sample and (d) the size distribution of the S11 nanofibers.

nanofibers (after the polymer burns out), we tested Ac: PVP precursor concentrations of 1:1 and 5:1. A detailed study of different acetate:poly(vinyl alcohol) (Ac:PVA) weight ratios has been conducted previously [19].

2.3. Solution blow spinning

The SBS technique uses two concentric nozzles: the inner one injects the polymeric solution at a controlled rate, and the outer one flows high-pressure gas for dragging the fibers to a rotating cylindrical collector. The angular speed and distance from the injection point to the collector (working distance) are set as 40 rpm and 40 cm, respectively. Fig. 1 shows the SBS experimental apparatus.

The precursor solution was loaded in a 3-mL hypodermic needle, which in turn was injected in a needle with 0.5-mm internal diameter. To produce Ac: PVP samples with 1:1 and 5:1 concentration, injection rates of 50 and 60 μL/min with air pressures of 133 and 66 kPa, respectively, were used. A halogen lamp was used to increase the local temperature and to evaporate the solvents as the solution was dragged. The nanofibers in the green state (before heat-treatment) were collected in a coated cylinder

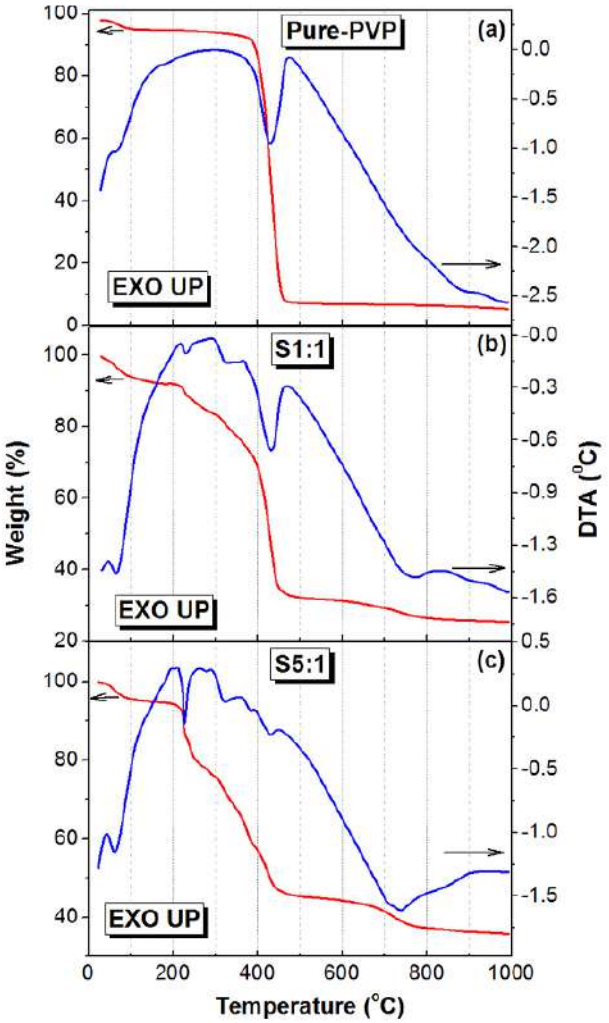

Fig. 3. (Color online) Simultaneous TGA/DTA thermal analysis of the as produced samples. (a) Reference (commercial PVP), (b) S11, and (c) S51 samples. The endothermic peak of the reference sample at 430 °C indicates PVP degradation. In panels (b) and (c), the peaks at ~800 °C indicate the beginning of the crystallization of the YBCO phase.

covered by a steel screen.

2.4. Heat treatment

The nanofiber composite in the green state was dried overnight at 100 °C and then heat-treated in two steps. In the first step, the samples were calcined at T=450 °C for 3 h in an oven to eliminate organic material. Both heating and cooling were performed at 1 °C/min. In the second step, the samples were sintered in a tube furnace at 820 °C for 14 h and then at 925 °C for 1 h, following which they were treated at 725 °C for 3 h and 450 °C for 12 h. Both steps were performed under oxygen flow. The heating rates from room temperature to 820 °C and from 820 °C to 925 °C were 3 °C/min and 1 °C/min, respectively. The cooling rate from 925 to 750 °C was 1 °C/min, and that from 750 °C to room temperature (remaining 12 h at 450 °C) was 3 °C/min. The samples obtained with Ac: PVP concentrations of 1:1 and 5:1 are called S11 and S51, respectively.

2.5. Characterization

Scanning electron microscopy (SEM) analysis was performed using an EVO LS15 Zeiss operated at 20 kV. Green state samples were coated with a thin layer of gold before SEM observations. IMAGE J software was used to measure the diameters of 100 nanofibers. Thermogravimetric measurements were performed using a TA Instruments model Q600 at temperatures between 25 and 1000 °C at a heating rate of 10 °C/min. Analyses were performed in nitrogen atmosphere with flow rate of 100 mL/min. XRD was performed using a Shimadzu XDR-6000 diffractometer with CuK_{α} radiation (wavelength: 1.5418 Å). The displacement ranged from $2\theta=5°$ to 60° at a scan rate of 0.02°/min.

3. Results and discussion

Fibers with a continuous structure are obtained when the polymer concentration is sufficient to thoroughly entangle the long polymeric chains with the molecules of the solvent [18]. In addition, a polymeric solution with low surface tension needs to be obtained to facilitate the evaporation of the solvent and then dry the solution before it has been collected [18]. Therefore, the morphology of the nanofibers is strongly influenced by the PVP concentration in the precursor solution. On the other hand, depending on the polymer concentration in the solution, the injection rate and pressure of compressed air need to be adjusted. Then, a stable cone formed by the solution at the tip can be established and, consequently, continuous fibers structures are produced. If suitable parameters are not set, undesired drops or discontinuities in the jet or even a film could be produced [18].

The diameter of the fibers is also influenced by the polymer concentration in the solution, i.e., lower polymer concentration produces fibers with smaller diameters. The evaporation rate of the solvent also depends on the polymer concentration, and consequently, beads and interconnections may be produced between the produced fibers [16–18].

After setting suitable parameters, polymeric nanofibers such as those shown in Fig. 2 were produced. For as produced S51, the fibers were oriented randomly and presented several beads, as shown in the micrograph in Fig. 2(a). The average diameter of these fibers was 389 nm, and around 25% of them had diameters smaller than 300 nm, as shown in Fig. 2(b).

For as produced S11, the production of beads decreased, as shown in the micrograph in Fig. 2(c). The average diameter of these fibers was 426 nm, as shown in Fig. 2(d); this value was close to that of S51. However, only 7% of the nanofibers showed diameters smaller than 300 nm. This behavior was expected because we used the same polymer concentration in both solutions, which resulted in fibers with similar diameters [17,18].

The commercial PVP sample shows weight loss of 6% at ~100 °C owing to the evaporation of water, as indicated by the TGA curve in Fig. 3(a). The second event with an endothermic peak in the DTA curve at 420 °C is attributed to PVP decomposition. From 25 to 280 °C, samples S11 and S51 lost 15.5% and 22.4% of their initial mass, respectively, as shown in Fig. 3(b) and (c). This behavior is attributed to dehydration and the elimination of other volatile substances [4]. These figures also show successive endothermic peaks from 280 to 500 °C for both samples. These events correspond to polymer combustion and decomposition of the organic groups of the acetates used in the precursor solutions [4,6,21]. In the same temperature range, the S11 sample lost more mass (53%) than the S51 one (33%), which is related the larger amount of PVP in its composition. Therefore, the peaks associated with acetate degradation are masked in the thermogram of sample S11. The exothermic peak above 780 °C (DTA curve) indicates the

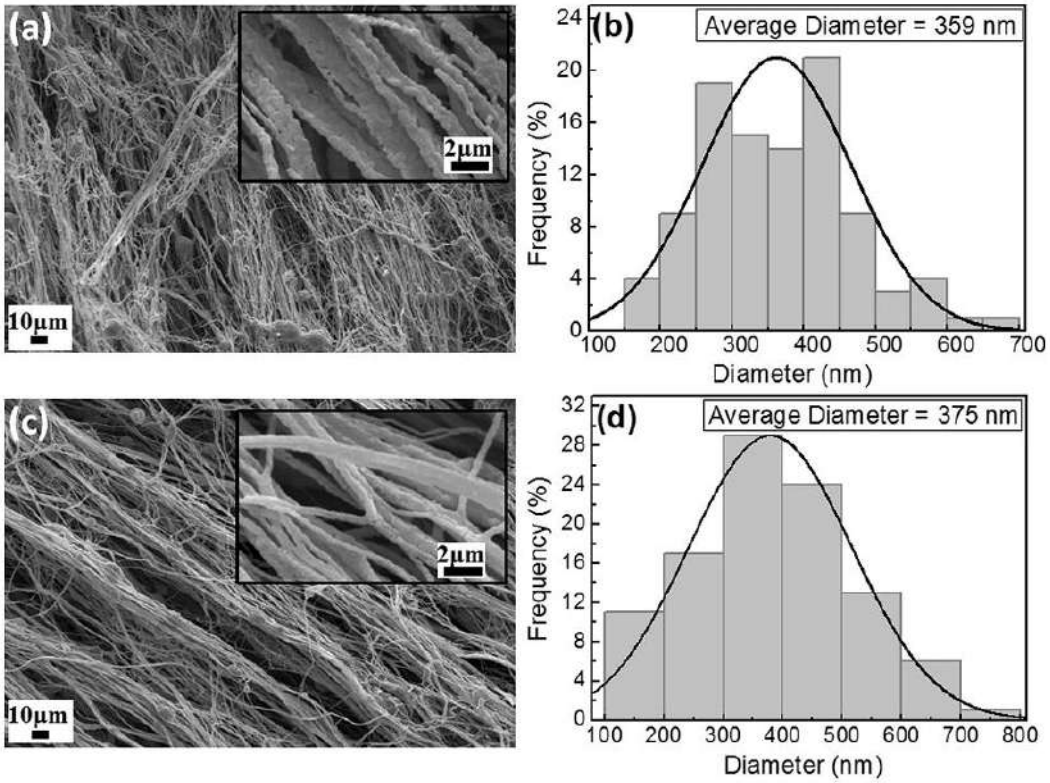

Fig. 4. SEM micrographs and diameter distribution of the samples after all heat-treatments and oxygenation. (a) Micrograph of the S51 sample and (b) the diameter distribution of its nanofibers. (c) Micrograph of the S11 sample and (d) the diameter distribution of its nanofibers.

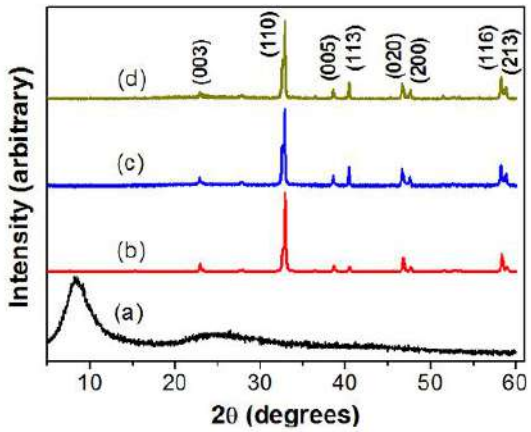

Fig. 5. (Color online) XRD diffractograms of the samples. (a) A sample in the green state (S51), (b) reference YBCO pattern (JCPDS-78-2273), and (c) S51 and (d) S11 YBCO nanofibers after sintering.

beginning of YBCO crystallization [6,21]. The total mass lost from room temperature up to 925 °C was 94.2%, 74%, and 64% in the commercial PVP, S11, and S51 samples, respectively. These results were used to choose the heat-treatment temperatures applied to obtain the YBCO phase.

Fig. 4 shows SEM images of the S51 and S11 samples and the distributions of their diameters after all heat treatments and oxygenation. The S51 and S11 samples showed a fibrous structure with nanoscale dimensions and average diameters of 359 and 375 nm, respectively. In the S11 sample, 32% of nanofibers were smaller than 300 nm; in the S51 sample, this value decreases to 27%.

The ceramic nanofibers are not smooth like those obtained by the composites shown in Fig. 2. Instead, they seem to be made of grains that are joined to each other, as seen in the inset of Fig. 4(a). Along with the samples in the green state, the ceramic nanofibers showed very similar diameters.

It should be noted that in our experiment, the green nanofibers were produced using flow rates of 50 and 60 μL/min for the S11 and S51 samples, respectively. These values are around four times greater than those used in the ES experiments [21].

XRD patterns of the green nanofiber and heat-treated samples S51 and S11 are shown in Fig. 5. The green sample shows an amorphous pattern with a broad peak at $2\theta = 8°$ that is attributed to PVP [4,29]. The XRD patterns of samples S51 and S11 showed peaks that are characteristic of YBCO ceramic (JCPDS-78-2273, curve (d)). We did not observe the formation of secondary phases, indicating that the heat-treatment applied was adequate. The Miller index in Fig. 5 is related to the patterns shown in Fig. 5(b), (c), and (d).

4. Conclusions

Nanofibers of pure $YBa_2Cu_3O_7$ were successfully obtained, for the first time, by using the novel SBS technique. Polymeric solutions with Ac:PVP concentrations of 5:1 and 1:1 were prepared. After heat-treatment, YBCO ceramic nanofibers with average diameters of 359 and 375 nm were produced from the 5:1 and 1:1 samples, respectively. We showed that the SBS technique can produce YBCO ceramic nanofibers with a production rate close to

four times greater that of ES.

Acknowledgements

We acknowledge the Instituto Federal de Mato Grosso do Sul-IFMS and the National Council for the Improvement of Higher Education-CAPES for the doctoral scholarship granted to Maycon Rotta.

Appendix A. Supplementary material

Supplementary data associated with this article can be found in the online version at http://dx.doi.org/10.1016/j.ceramint.2016.07.152.

References

[1] C.A. Gautier, J.C. Loulergue, J. Etchepare, S. Hunsche, H. Kurz, T.P. Doughtery, S. Adachi, K.A. Nelson, Y.R. Shen, T. Ruf, J.M. Zhang, R. Lauck, M. Cardona, T. Hattori, Y. Homma, A. Mitsuishi, M. Tacke, A. Torabi, T.E. Stevens, M. Born, K. Huang, Directed assembly of one-dimensional nanostructures into functional networks, Science 291 (2001) 630–634.

[2] G.Y. Tseng, J.C. Ellenbogen, Toward nanocomputers, Science 294 (2001) 1293–1295.

[3] E.A. Duarte, P.A. Quintero, M.W. Meisel, J.C. Nino, Electrospinning synthesis of superconducting BSCCO nanowires, Phys. C Supercond. Appl. 495 (2013) 109–113.

[4] Z. Shen, Y. Wang, W. Chen, L. Fei, K. Li, H.L.W. Chan, L. Bing, Electrospinning preparation and high-temperature superconductivity of YBa2Cu3O7-x nanotubes, J. Mater. Sci. 48 (2013) 3985–3990.

[5] J. Yuh, L. Perez, W.M. Sigmund, J.C. Nino, Electrospinning of complex oxide nanofibers, Phys. E Low-Dimens. Syst. Nanostruct. 37 (2007) 254–259.

[6] J. Yuh, L. Perez, W.M. Sigmund, J.C. Nino, Sol-gel based synthesis of complex oxide nanofibers, J. Sol-Gel Sci. Technol. 42 (2007) 323–329.

[7] A. Rogina, Electrospinning process: Versatile preparation method for biodegradable and natural polymers and biocomposite systems applied in tissue engineering and drug delivery, Appl. Surf. Sci. 296 (2014) 221–230.

[8] C. Mu, Y. Song, X. Wang, P. Wu, Kesterite Cu2ZnSnS4 compounds via electrospinning: a facile route to mesoporous fibers and dense films, J. Alloy. Compd. 645 (2015) 429–435.

[9] G.C. Leindecker, A.K. Alves, C.P. Bergmann, Synthesis of niobium oxide fi bers by electrospinning and characterization of their morphology and optical properties, Ceram. Int. (2014) 1–6.

[10] N. Bhardwaj, S.C. Kundu, Electrospinning: a fascinating fi ber fabrication technique, Biotechnol. Adv. 28 (2010) 325–347.

[11] R. Nayak, R. Padhye, I.L. Kyratzis, Y.B. Truong, L. Arnold, Recent advances in nanofibre fabrication techniques, Text. Res. J. 82 (2) (2011) 129–147.

[12] Z. Huang, Y. Zhang, M. Kotaki, S. Ramakrishna, A review on polymer nanofibers by electrospinning and their applications in nanocomposites, Composites Science and Technology; 63, 2003, pp. 2223–2253.

[13] J. Gao, W. Li, H. Shi, M. Hu, R.K.Y. Li, Preparation, morphology, and mechanical properties of carbon nanotube anchored polymer nanofiber composite, Compos. Sci. Technol. 92 (2014) 95–102.

[14] W. Teo, S. Ramakrishna, Electrospun nanofibers as a platform for multifunctional, hierarchically organized nanocomposite, Compos. Sci. Technol. 69 (2009) 1804–1817.

[15] R. Maria, R. Rodrigues, J. Elvis, Production of submicrometric fi bers of mullite by solution blow spinning (SBS), Mater. Lett. 149 (2015) 47–49.

[16] B. Cheng, X. Tao, L. Shi, G. Yan, X. Zhuang, Fabrication of ZrO2 ceramic fi ber mats by solution blowing process, Ceram. Int. 40 (2014) 15013–15018.

[17] E.S. Medeiros, G.M. Glenn, A.P. Klamczynski, W.J. Orts, L.H.C. Mattoso, Solution blow spinning : a new method to produce micro- and nanofibers from polymer solutions, J. Appl. Polym. Sci. 113 (4) (2009) 2322–2330.

[18] S. Afonso, J.E. Oliveira, E.A. Moraes, R.G.F. Costa, L.H.C. Mattoso, W.J. Orts, E. S. Medeiros, W. Luis, C. Ufscar, R.W. Luis, Nano and submicrometric fibers of poly (D, L -Lactide) pbtained by solution blow spinning : process and solution variables, J. Appl. Polym. Sci. 122 (5) (2011) 3396–3405.

[19] X.M. Cui, W.S. Lyoo, W.K. Son, D.H. Park, J.H. Choy, T.S. Lee, W.H. Park, Fabrication of YBa2Cu3O7−δ superconducting nanofibres by electrospinning, Supercond. Sci. Technol., 19, 2006, pp. 1264–1268.

[20] E. Zussman, YBCO nanofibers synthesized by electrospinning a solution of poly (acrylic acid) and metal nitrates, J. Mater. Sci. (2008) 1664–1668.

[21] E.A. Duarte, N.G. Rudawski, P.A. Quintero, M.W. Meisel, J.C. Nino, Electrospinning of superconducting YBCO nanowires, Supercond. Sci. Technol. 28 (1) (2014) 015006–015012.

[22] R.F. Service, N. York, S. Rf, P. Types, C.S. Mostrando, Nanocomputing. Assembling nanocircuits from the bottom up, Science 293 (2016) 1–2.

[23] S. Anders, M.G. Blamire, F. Buchholz, D. Crété, R. Cristiano, P. Febvre, L. Fritzsch, A. Herr, E. Il, J. Kohlmann, J. Kunert, H. Meyer, J. Niemeyer, T. Ortlepp, H. Rogalla, T. Schurig, M. Siegel, R. Stolz, E. Tarte, H.J.M. Brake, H. Toepfer, J. Villegier, A.M. Zagoskin, A.B. Zorin, European roadmap on superconductive electronics – status and perspectives q, Phys. C Supercond. Appl. 470 (2010) 2079–2126.

[24] P. Febvre, G. Burnell, T. Claeson, D. Cre, G.J. Gerritsma, H. Hilgenkamp, R. Humphreys, Z. Ivanov, W. Jutzi, M.I. Khabipov, J. Mannhart, J. Niemeyer, A. Ravex, H. Rogalla, M. Russo, J. Satchell, M. Siegel, H. To, F.H. Uhlmann, E. Wikborg, D. Winkler, A.B. Zorin, SCENET Roadmap for Superconductor Digital Electronics, (2006) 1–41.

[25] T. Izumi, Y. Shiohara, R & D of coated conductors for applications in Japan, Phys. C. Supercond. Appl. 470 (2010) 967–970.

[26] H. Zueger, 630 kVA high temperature superconducting transformer, Cryogenics 38 (1998) 1169–1172.

[27] P.N. Barnes, M.D. Sumption, G.L. Rhoads, Review of high power density superconducting generators : Present state and prospects for incorporating YBCO windings, Cryogenics, 45, 2005, pp. 670–686.

[28] P. Manuel, Prospects for application of high temperature superconductors to electric power networks, Phys. C: Supercond. 376 (2002) 1591–1597.

[29] D. Khan, B. Ahmed, S.K. Raghuvanshi, M.A. Wahab, Structural, morphological and optical properties of silver doped polyvinylpyrrolidone composites, Indian J. Pure Appl. Phys. 52 (2014) 192–197.